COMPUTATIONAL STUDIES OF TRANSITION METAL NANOCLUSTERS ON METAL-SUPPORTED GRAPHENE MOIRÉ

A Thesis
Presented to
The Academic Faculty

by

Die Teng

In Partial Fulfillment
of the Requirements for the Degree
Doctor of Philosophy in the
School of Chemical & Biomolecular Engineering

Georgia Institute of Technology
May 2014

COMPUTATIONAL STUDIES OF TRANSITION METAL NANOCLUSTERS ON METAL-SUPPORTED GRAPHENE MOIRÉ

Approved by:

Dr. David S. Sholl, Advisor
School of Chemical & Biomolecular Engineering
Georgia Institute of Technology

Dr. Mark P. Styczynski
School of Chemical & Biomolecular Engineering
Georgia Institute of Technology

Dr. Dennis W. Hess
School of Chemical & Biomolecular Engineering
Georgia Institute of Technology

Dr. Andrew Zangwill
School of Physics
Georgia Institute of Technology

Dr. Carsten Sievers
School of Chemical & Biomolecular Engineering
Georgia Institute of Technology

Dr. Ye Xu
Cain Department of Chemical Engineering
Louisiana State University

Date Approved: March 24, 2014

To my parents

ACKNOWLEDGEMENTS

There are a number of excellent people I would like to acknowledge and give credits to. First of all, I would like to present my sincere gratitude to my academic advisor and mentor, Dr. David S. Sholl, for his constant guidance and support over the course of my Ph.D. studies. His enthusiasm for research and rigorous scholarship are infectious. His continuous encouragement helped me to be creative and innovative at research. I always admire his wisdom, solid knowledge, and personality that will continue inspiring me in my future career endeavors. I would like to thank Dr. Dennis W. Hess, Dr. Carsten Sievers, Dr. Mark P. Styczynski, Dr. Andrew Zangwill, and Dr. Ye Xu for serving in my thesis committee and providing insightful comments and suggestions.

I would like to thank my research collaborators, Dr. Lymarie Semidey-Flecha, Dr. Bradley F. Habenicht, and Dr. Ye Xu for their excellent guidance, advice and discussions. I want to especially thank Lasse B. Vilhelmsen from Aarhus University in Denmark for providing enormous instructions and help on the subject of genetic algorithm. I am thankful to Dr. Tao Liang and Dr. Susan B. Sinnott for their hospitable hosting during my visit in University of Florida and introducing me to the fascinating world of COMB potential.

I am grateful to the former and present group members, and I would not have accomplished so much without their generous help. Special thanks are dedicated to Dr. Taku Watanabe, Dr. Thomas A. Manz, Dr. Ki Chul Kim, Dr. Shiqiang Hao, Dr. Veronika Walkosz, and Dr. Xuerong Shi. Thank you for the stimulating discussions and valuable

suggestions, and I greatly appreciate your assistance, patience and encouragement when I was in the bottleneck of my research. I also want to thank Dr. Hanjun Fang, Dr. Ji Zang, Dr. Mohamad Kassaee, Dr. Sung Gu Kang, Dr. Emmanuel Haldoupis, Dr. Rongshun Zhu, Dr. Iyad Hijazi, Liwei Li, Nita Chandrasekhar, Timothy van Heest, Amberish Kulkarni, Daniel Wei, Kelly Nicholson, Jason Gee, and other group members for their help and support during my pursuit of Ph.D. in Georgia Tech.

Finally, I would like to express my deepest gratitude to my parents in China for their love, understanding, and support. My successful completion of Ph.D. degree would not have been possible without them. My special thanks belong to my boyfriend, Dr. Xiaojing Ye, for his love and support.

This work is supported as part of the Center for Atomic Level Catalyst Design, an Energy Frontier Research Center funded by the U.S. Department of Energy (DOE), Office of Science, and Office of Basic Energy Sciences under Award Number DE-SC0001058.

Die (Dieh) Teng

Atlanta, GA

March 10, 2014

TABLE OF CONTENTS

Page

LIST OF TABLES

Page

LIST OF FIGURES

Page

SUMMARY

The graphene moiré superstructure formed on Ru(0001) (g/Ru(0001)) has shown the potential as a template to self-assemble super-lattices of metal nanoparticles as model catalysts. To explore the possibility of rational catalyst design on g/Ru(0001), it is desirable to know the minimum-energy adsorption sites, adsorption energies, and diffusion properties of small metal species on this surface. Toward this end, detailed density functional theory (DFT) calculations have been performed to investigate the adsorption and diffusion of Rh and Au adatoms on g/Ru(0001). The results show that the adsorption of both Rh_1 and Au_1 is most stable in the fcc region on the graphene moiré. The global diffusion barrier is estimated to be 0.53 eV for Rh_1 and 0.71 eV for Au_1, corresponding to a hopping rate between adjacent moiré cells of ~10^3 s^{-1} and ~1 s^{-1} at 298 K, respectively. The consequences of different hopping rates for cluster nucleation have been explored by performing Monte Carlo-based statistical analysis, which suggests that diffusing species other than adatoms need to be taken into account to develop an accurate description of cluster nucleation and growth on this surface.

DFT calculations have also been carried out to investigate the adsorption and diffusion of 18 4d (Y-Ag) and 5d (La-Au) transition metal adatoms on g/Ru(0001), using small surface models representing different regions of the g/Ru(0001) surface. For each adatom, adsorption is the strongest in the fcc region and the weakest in the mound region of the moiré. Diffusion within the fcc region is facile for most adatoms, but an additional barrier is imposed by the corrugation of the graphene moiré for traversing between neighboring fcc regions. Overall, the earlier 4d and 5d metal adatoms have stronger

adsorption energies and higher diffusion barriers on g/Ru(0001) than the later ones. These results provide a better understanding of the conditions necessary to achieve dense super-lattices of monodisperse metal clusters on g/Ru(0001).

Given the necessity to study larger diffusing species than adatoms, DFT calculations have been performed to study the adsorption and diffusion of Rh and Au dimers and trimers on g/Ru(0001). The fcc region of g/Ru(0001) was predicted to be where dimers and trimers are most strongly adsorbed and where the nucleation of metal nanoclusters occurs. The diffusion mechanisms and energy barriers for the dimers and trimers on g/Ru(0001) were calculated, and the results was compared with monomer diffusion. It was shown that the mobility of Rh clusters decreases with the increase of cluster size, while for Au, dimers diffuse faster than monomers and trimers on the moiré surface. These calculations give us insights into the nucleation and growth mechanism of metal clusters on graphene moiré.

Gold nanoparticles have been extensively studied for their high catalytic activity both theoretically and experimentally. We used a genetic algorithm combined with DFT calculations to predict the lowest energy structure of a Au_8 cluster on g/Ru(0001). The most stable Au_8 structure and its adsorption energy in the fcc and the ridge region of g/Ru(0001) were reported. Our result gives a double-layer Au wall structure for Au_8 in the fcc region, where the Au_8 cluster is most strongly adsorbed. Our prediction is consistent with the Au island structure experimentally observed on g/Ru(0001), which supports the hypothesis that Au clusters aggregates through Oswald ripening with Au dimer being the major diffusing species.

Finally, we examined the morphology of Cu clusters on g/Cu(111) by investigating the adsorption of a Cu_{19} cluster in the fcc region of g/Cu(111) using MD simulations with COMB3 potential. We determined the low energy Cu_{19} structures and their adsorption energies at 0 K on g/Cu(111). Our results show that at low temperature, a Cu_{19} cluster prefers to form a 3D compact structure on g/Cu(111). We also studied the mobility of Cu clusters on g/Cu(111) by performing NVT-MD simulations at elevated temperatures. The analysis shows that the small corrugation of g/Cu(111) imposes weak interaction on the supported Cu clusters, which suggests that g/Cu(111) may not be a suitable substrate for the formation and growth of isolated Cu clusters.

CHAPTER 1

INTRODUCTION

1.1 Background and Motivation

Subnanometer- and nanometer-size clusters are materials that are distinctly different from the corresponding bulk phases and can possess unique electronic, catalytic, magnetic, and optical properties [1, 2]. Recent studies have demonstrated that metal nano-clusters differing by just a few atoms can exhibit distinctly different catalytic properties [3-6]. Size is therefore potentially another dimension in which to tune catalyst properties, besides composition and structure. To exploit these properties, it is desirable to fabricate dense arrays of uniformly sized, monodisperse clusters. Methods to prepare clusters include ligand-stabilized metal clusters [7], inverse micelles [2], and soft-landing of mass-selected clusters [8]. Although these methods can produce cluster with highly uniform sizes or shapes, it remains a challenge to fabricate dense arrays of monodisperse, uniformly sized, and spatially accessible clusters on well-defined substrates, which would make desirable platforms on which to perform model catalysis studies at low to moderate temperatures [9]. A viable approach involves the use of patterned surfaces as templates [10] for the self-assembly of atoms into clusters. The formation of metal clusters has been reported, for example, on epitaxial films of Al_2O_3 [11, 12], FeO [13], BN [14], and graphene formed on support materials [15, 16]; and on vicinal or reconstructed surfaces of Si(111) [17] and Au(111) [18, 19]. The pioneering work by N'Diaye *et al.* [20] has demonstrated that graphene moiré formed on Ir(111) (denoted as g/Ir(111)) can function as such a template for the nucleation and growth of metal clusters. Densely populated

super-lattices of metal clusters with narrow size distribution were reported for Ir [20], Pt, and W, and for Re and Au at low temperature [21]. Among potential applications, such super-lattices of clusters can make interesting model catalysts [22, 23].

Epitaxial growth on transition metals is one of the main methods for preparing graphene [24]. Graphene has been synthesized on Co(0001) [25], Ni(111) [26], Cu(111) [27, 28], Ru(0001) [29-32], Rh(111) [33], Ir(111) [16, 34-36], Pd(111) [37, 38], and Pt(111) [39-41]. A moiré super-structure has been observed in graphene on Ru(0001), Rh(111), Pd(111), Ir(111), and Cu(111) because of a mismatch between the graphene and metal lattices, which results in alternating regions of C atoms being either favorably or unfavorably aligned with the underlying metal atoms to undergo sp^3 rehybridization [42, 43]. It can be envisaged that by varying the substrate metal, the graphene-substrate coupling [44, 45], and the deposited metal [22], a series of monodisperse, structurally uniform nano-clusters with different compositions and sizes can be achieved, leading to exciting potential applications.

Like on Ir(111), continuous, single-crystalline, a defect-free graphene moiré that can grow to micron sizes and over step edges without interruption has been obtained on Ru(0001) [29, 32, 46-48]. Graphene moiré on Ru(0001) (denoted as g/Ru(0001); Figure 1.1) is stable in air up to ca. 500 K [49, 50], making it a suitable support material for model catalysts with the advantage of being free of multiple reactive elements as are typically present on oxides. Efforts to use g/Ru(0001) to self-assemble metal clusters have so far involved a handful of different metals. At room temperature, Pt [51, 52] and Ru [22, 53] form numerous dispersed clusters with a narrow distribution of sizes and heights; Rh forms dispersed but less numerous clusters [32]; whereas Pd, Co [32], Au [9,

32, 54], and Fe [55] atoms coalesce into a few large aggregates. Lower temperature (140-180 K for Pt [52]; 230-250 K for Ru [22]) results in the occupation of all moiré cells (i.e., maximum number density) on g/Ru(0001). These examples on g/Ru(0001) and those demonstrated on g/Ir(111) [36] suggest that thermally activated surface transport processes strongly control the nucleation and growth behavior of metal clusters on the graphene moiré. These kinetic aspects, however, have not been completely explored.

The periodicity for the graphene moiré superstructure on Ru(0001) has been approximated to be (12×12)-graphene-on-(11×11)-Ru(0001) [31, 43, 47, 56]. Density functional theory (DFT) calculations suggest that alternating regions of C-Ru alignment are formed due to the lattice mismatch between the graphene and Ru(0001) substrate. The regions where C and Ru are aligned for sp^3 rehybridization are the fcc and hcp regions (Figure 1.1a). In the area between these regions, which we term the ridge region, the C atoms shift continuously relative to the underlying Ru atoms. In the atop region, the graphene physically protrudes away from the Ru(0001) surface, which precludes Ru-C bonding. There is no definite borderline between the different regions. Recent angle-resolved ultraviolet photoelectron spectroscopy experiments reported that the electronic structure of graphene on Ru(0001) splits into two, suggesting two broadly chemically different regions [57].

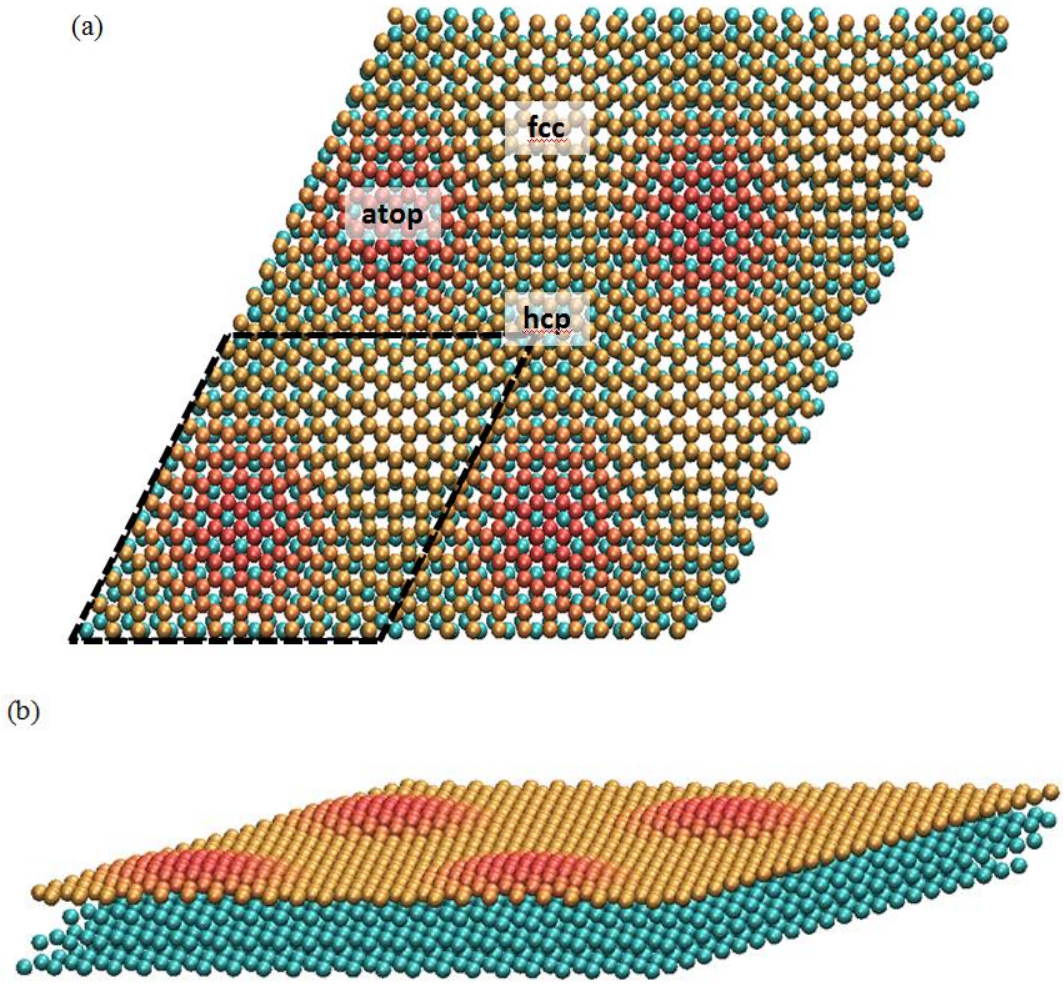

Figure 1.1: The relaxed moiré structure of (12×12) graphene (red, yellow)/(11×11) Ru(0001) (cyan) supercell obtained by a DFT calculation [58]. C atoms are colored with gradient based on their heights with respect to the Ru surface: the redder the higher. (a) Top view of the fcc (yellow), hcp (yellow), and atop (red) regions; The boxed hexagonal area is one unit cell. (b) Side view of moiré pattern.

First-principles electronic structure calculations are well suited to provide quantitative information regarding the kinetics of molecular-level processes. The surface mobility of clusters usually drops rapidly with increasing cluster size [59], so adatoms are expected to play an important role in cluster growth and mobility [60]. We aim to understand the adsorption and diffusion of small cluster species on graphene moiré as a

necessary step towards understanding mechanism of cluster nucleation and growth. To start, we will investigate Rh and Au monomers on g/Ru(0001). Rh and Au were chosen as our focus because of their distinct patterns in forming clusters on g/Ru(0001) [61]. We will characterize the adsorption and diffusion of Rh and Au adatoms on the full surface of g/Ru(0001) and in its different regions. The insight we gained allows us to extend our study to all 4d and 5d metal adatoms on g/Ru(0001).

Monomer diffusion alone, however, is not sufficient to describe the growth mechanism of clusters of these metals on the surface. Conventional descriptions of cluster diffusion assume that cluster mobility drops rapidly as the cluster size increases. For example, Voter showed that for Rh clusters on Rh(100), the diffusion constant scales as $n^{-1.76 \pm 0.06}$ for clusters larger than n = 15 atoms [62]. Examples are known, however, where diffusion of sizeable clusters occurs. Wen *et al*. reported that Ag clusters on Ag(100) containing hundreds of atoms have significant mobility [63] and other direct observations of large cluster diffusion on surfaces have also been made [64-66]. Multiple studies [67-76] have shown that small clusters (dimer, trimer, etc.) are mobile on many surfaces and their motion should be included in a proper description of cluster nucleation and growth. A recent study by Signor *et al*. on linear Cu trimers on Ag(111) showed that trimers, once formed, have significantly higher mobility than either monomers or dimers [70]. Xu *et al*. pointed out that for Pd diffusion on MgO(100), the tetramer is the fastest diffusing species at room temperature [71, 72]. Studies of small Ag, Au, Pd, Cu and Ca clusters on MgO(100) surface show that small clusters such as dimers, trimers, and tetramers are mobile on the surface at the operating temperature of molecular beam epitaxy (MBE) experiments and they display a variety of diffusion mechanisms [73, 74].

The discussion above indicates that a description of the mobility of small metal clusters on the g/Ru(0001) surface is necessary before efforts can be made to describe cluster nucleation and growth. We will thus address the issue of small cluster diffusion on this graphene moiré surface by reporting DFT calculation results of adsorption and diffusion of Rh and Au dimers and trimers on g/Ru(0001). We also extend our study to other 4d and 5d transition metals to give initial insight into their nucleation behavior on g/Ru(0001).

Gold nanoparticles have exhibited incredible catalytic activity in low temperature catalytic processes [77-79]. Since Haruta *et al*. showed that nanosized Au particles (< 5 nm) can be very effective catalysts [80], extensive studies have been carried out for the high catalytic activity of Au nanoparticles in various chemical processes, including low temperature CO oxidation [79-83], selective hydrogenation [84], NO_x reduction [85, 86], hydrogen peroxide formation [87], propene epoxidation [88, 89], and water-gas shift reaction [90, 91]. Mechanistic studies on the catalytic activity of nanosized Au in low temperature oxidation reactions indicate the importance of the synergistic effects between Au and oxide substrates [92] and the Au sites with low coordination number [93]. Therefore, to study the intrinsic catalytic activity of nanosized Au, Au clusters need to be studied on an oxygen-free substrate. One challenge in heterogeneous catalysis is to synthesize supported metal particles with maximum control over their composition and structure. To serve this purpose, the desired substrate needs to have periodic nucleation sites to disperse metal clusters so that they can be stabilized against aggregation [94]. One example of such material, which is also oxygen-free, is the graphene moiré on metal substrates, such as g/Ru(0001), the system we are investigating in this work.

Supported Au_8 clusters are known experimentally to exhibit a high chemical activity [78] and thus worthy of detailed investigation of its atomic-scale structure. A recent study on the Au_8 cluster on MgO(100) identified structures more stable than ever reported before and rationalized its high activity by predicting a high O_2 binding energy (up to 1 eV) to the cluster [95]. This has drawn us interest to characterize Au_8 clusters on g/Ru(0001). To study a larger cluster with more than a few atoms is challenging due to the enormous configurational space we have to examine. Specifically, we need to determine the lowest energy configuration of a Au_8 cluster on g/Ru(0001). Because the number of candidate local energy minima grows exponentially with the number of atoms, the computational effort scales exponentially with cluster size. To face this challenge, we adopted a computational method combining a Genetic Algorithm (GA) [95, 96] with Density Functional Theory (DFT) calculations to systematically scan for the low energy Au_8 structures on the surface of g/Ru(0001). This method has been successfully applied to study Au clusters on MgO(100) *F* centers [95] and large metal clusters in metal organic frameworks (MOFs) [75, 97]. We also estimated the diffusion barrier of Au_8 on g/Ru(0001) and provided a hypothesis of how Au clusters form on the surface.

The results outlined above used DFT calculations to investigate different species of small metal clusters on g/Ru(0001). These results give us insight into the mechanisms of cluster formation on g/Ru(0001), but they are not sufficient to help us understand all aspects of cluster nucleation and growth. It is thus necessary to focus on even larger clusters (>10 atoms) on supported graphene and seek suitable methods to describe and simulate this type of systems. DFT calculations generally provide high accuracy for material properties. However, because of the large computational cost, DFT methods are

limited to relatively small system sizes, typically a few hundred atoms. Because of the limitation in time and length scale that DFT method can describe, it is thus not able to address many important issues associated with large and complex microstructures. Classical molecular simulations, such as molecular dynamics (MD) and Monte Carlo, has been employed to examine systems with time and length scales that are beyond the reach of DFT methods. The advantage of these methods is their high computational speed and their ability to probe large systems at finite temperatures and under external driving forces.

The key component in classical molecular simulations is the inter-atomic potential that describes the bonding and non-bonding effects of valence electrons without explicitly describing the electrons themselves. It has not generally possible for empirical inter-atomic potentials to describe structures with more than one bonding type, because empirical potentials for different bonding types have different functional forms. The charge optimized many-body (COMB) potential [98-100] is one of several reactive force fields that can describe complex bonding environments in real materials. Another widely used potential of this kind is the reactive force field (ReaxFF) [101]. Both COMB and ReaxFF describe reactive processes by allowing bond formation and bond breaking during classical simulations. The force field parameters used in the potential terms are optimized relative to DFT and/or other quantum chemical calculations and/or reported experimental values in literature. Molecular simulations using COMB or ReaxFF are slower than using non-reactive force fields, but are still significantly faster than DFT calculations, allowing simulations of systems larger than 10^6 atoms at nanosecond time scales [102-106]. Here we focus our research on using the COMB potential.

The development of COMB potentials has gone through three major stages, denoted COMB1, COMB2, and COMB3, respectively. Each generation has made a significant improvement over the previous one. In particular, several functions in COMB3 have been refined in the aim of providing a general, flexible, and robust empirical potential formalism that is capable of treating all different types of bonds within a multi-component system in an integrated manner [98]. COMB1 has been successfully applied to reproduce the phase order of SiO_2 [100] and Cu [107]. COMB2 has been applied to Si-SiO_2 system and amorphous SiO_2 [99], the Cu-SiO_2 [108], Hf-HfO_2 [109], and Cu-Cu_2O [110] systems, and Cu adatoms on ZnO surfaces [111]. COMB3 was recently proposed and demonstrated to be able to describe organic-metal interaction in a dynamically changing environment [98]. All three generations of COMB have been implemented into the Large-scale Atomic/Molecular Massively Parallel Simulator (LAMMPS) program [112, 113].

A strong limitation of the COMB potential to date is that it has only been developed for a limited set of elements including C, H, O, Cu, Al, Zr, Zn, and Ti. As a result, it is not currently possible to study Rh or Au on supported graphene with COMB potential. To work within this limitation, we aim to investigate large Cu clusters on graphene supported by Cu(111) (denoted as g/Cu(111)). Epitaxial graphene has been grown on Cu(111) and it has been observed experimentally by scanning tunneling microscopy and spectroscopy [114-116]. Multiple moiré patterns were observed, which is a result of different rotational alignments of the graphene lattice with the underlying Cu(111) lattice. This indicates that the graphene is weakly coupled to the substrate. There are two predominant moiré patterns observed, which suggests that graphene has

preferred orientation with the underlying Cu(111). We will only simulate the large moiré pattern (~6.6 nm periodicity) when the graphene lattice is aligned with Cu(111) lattice with $0°$ rotation. Computational studies [117, 118] of graphene on transition metal surfaces predict that the lattice mismatch between graphene and Cu(111) is small (4.44%) and the binding is weak. It was also reported that the potential energy surface (PES) of graphene on Cu(111) is similar to that on Ru(0001), only with less corrugation [117]. This suggests that the fcc region of g/Cu(111) is the strongest adsorption region, which is the same as the case of g/Ru(0001). Cu adatoms have been theoretically studied on graphene [119], but unfortunately, there is no prior literature reporting Cu clusters on g/Cu(111) experimentally or computationally.

We will thus predict the morphology of Cu clusters on g/Cu(111) and investigate their mobility at elevated temperatures using MD simulations with the COMB3 potential. We focus our study on Cu_{19}, a magic size cluster. A few other clusters with different sizes are considered for the study of cluster diffusivity at different temperatures with respect to cluster size.

1.2 Thesis Organization

We performed Density Functional Theory (DFT) calculations to investigate the adsorption and diffusion properties of Rh and Au monomers on g/Ru(0001). Using the information, we conducted a statistical analysis by performing Monte Carlo simulations. The calculation details and results of Rh and Au monomers on g/Ru(0001) are presented in Chapter 2. Given the insight we gained from Chapter 2, we extended the study of adsorption and diffusion of metal monomers on g/Ru(0001) to include all 4d and 5d transition metals. The trends in adsorption energy and diffusion barriers of metal

monomers across the periodic table are discussed in Chapter 3. Given the importance of small cluster diffusion on various surfaces, the necessity to study small metal clusters on g/Ru(0001) motivated us to investigate the adsorption and diffusion properties of Rh and Au dimers and trimers on g/Ru(0001). The results of dimer/trimer adsorption configuration and diffusion energy barrier are presented in Chapter 4. In Chapter 5, we used the computational method combing Genetic Algorithm (GA) with DFT to study the thermodynamics of Au_8 cluster on g/Ru(0001). The most stable Au_8 configurations in the fcc and the ridge region are reported. We also proposed a hypothesis of Au film formation mechanism on g/Ru(0001) based on our Au_8 predictions and previous results of Au clusters in Chapter 2-4. Because of the limitation of system size we can study using DFT method, we continued on exploring large metal clusters on graphene moiré surface using Molecular Dynamics (MD) simulations. These simulations were performed via Large-scale Atomic/Molecular Massively Parallel Simulator (LAMMPS) and the intermolecular potential was described by the 3rd generation of charge optimized many-body (COMB3) potential. The results of simulating Cu clusters on graphene/Cu(111) are reported in Chapter 6. We will conclude all our work and give an outlook of this research field in Chapter 7.

1.3 References

[1] J.D. Aiken, R.G. Finke, J. Mol. Catal. A-Chem., 145 (1999) 1-44.

[2] J.P. Wilcoxon, B.L. Abrams, Chem. Soc. Rev., 35 (2006) 1162-1194.

[3] U. Heiz, A. Sanchez, S. Abbet, W.D. Schneider, Chem. Phys., 262 (2000) 189.

[4] A.M. Argo, B.C. Gates, J. Phys. Chem. B, 107 (2003) 5519-5528.

[5] S. Lee, C. Fan, T. Wu, S.L. Anderson, J. Am. Chem. Soc., 126 (2004) 5682.

[6] S. Vajda, M.J. Pellin, J.P. Greeley, C.L. Marshall, L.A. Curtiss, G.A. Ballentine, J.W. Elam, S. Catillon-Mucherie, P.C. Redfern, F. Mehmood, P. Zapol, Nat. Mater., 8 (2009) 213-216.

[7] B.C. Gates, Chem. Rev., 95 (1995) 511-522.

[8] S. Abbet, K. Judai, L. Klinger, U. Heiz, Pure Appl. Chem., 74 (2002) 1527-1535.

[9] L. Liu, Z. Zhou, Q. Guo, Z. Yan, Y. Yao, D.W. Goodman, Surf. Sci., 605 (2011) L47-L50.

[10] C. Becker, K. Wandelt, Top. Curr. Chem., 287 (2009) 45-86.

[11] A. Buchsbaum, M. De Santis, H.C.N. Tolentino, M. Schmid, P. Varga, Phys. Rev. B, 81 (2010) 115420.

[12] A. Uhl, Y. Lei, H. Khosravian, C. Becker, K. Wandelt, R.D. Adams, M. Trenary, R.J. Meyer, J. Phys. Chem. C, 114 (2010) 17062-17068.

[13] N. Nilius, E.D.L. Rienks, H.P. Rust, H.J. Freund, Phys. Rev. Lett., 95 (2005) 066101.

[14] I. Brihuega, C.H. Michaelis, J. Zhang, S. Bose, V. Sessi, J. Honolka, M.A. Schneider, A. Enders, K. Kern, Surf. Sci., 602 (2008) L95-L99.

[15] A.T. N'Diaye, S. Bleikamp, P.J. Feibelman, T. Michely, Phys. Rev. Lett., 97 (2006) 215501.

[16] A.T. N'Diaye, T. Gerber, C. Busse, J. Myslivecek, J. Coraux, T. Michely, New J. Phys., 11 (2009) 103045.

[17] J.L. Li, J.F. Jia, X.J. Liang, X. Liu, J.Z. Wang, Q.K. Xue, Z.Q. Li, J.S. Tse, Z.Y. Zhang, S.B. Zhang, Phys. Rev. Lett., 88 (2002) 066101.

[18] M. Fonin, Y.S. Dedkov, U. Rudiger, G. Guntherodt, Surf. Sci., 529 (2003) L275-L280.

[19] J.V. Lauritsen, J. Kibsgaard, S. Helveg, H. Topsoe, B.S. Clausen, E. Laegsgaard, F. Besenbacher, Nat. Nanotechnol., 2 (2007) 53-58.

[20] A.T. N'Diaye, S. Bleikamp, P.J. Feibelman, T. Michely, Phys. Rev. Lett., 97 (2006) 215501.

[21] A.T. N'Diaye, T. Gerber, C. Busse, J. Myslivecek, J. Coraux, T. Michely, New J. Phys., 11 (2009) 19.

[22] A.K. Engstfeld, S. Beckord, C.D. Lorenz, R.J. Behm, ChemPhysChem, 13 (2012) 3313-3319.

[23] B.F. Habenicht, Y. Xu, L. Liu, Graphene moiré supported metal clusters for model catalysis studies, in: Z. Chen, D. Jiang (Eds.) Graphene Chemistry: Theoretical Perspectives, Wiley, 2013.

[24] J. Wintterlin, M.L. Bocquet, Surf. Sci., 603 (2009) 1841-1852.

[25] D. Eom, D. Prezzi, K.T. Rim, H. Zhou, M. Lefenfeld, S. Xiao, C. Nuckolls, M.S. Hybertsen, T.F. Heinz, G.W. Flynn, Nano Lett., 9 (2009) 2844-2848.

[26] M. Weser, Y. Rehder, K. Horn, M. Sicot, M. Fonin, A.B. Preobrajenski, E.N. Voloshina, E. Goering, Y.S. Dedkov, Appl. Phys. Lett., 96 (2010) 012504.

[27] X. Chen, S. Liu, L. Liu, X. Liu, X. Liu, L. Wang, Appl. Phys. Lett., 100 (2012) 163106-163103.

[28] W. Kim, K. Yoo, E.K. Seo, S.J. Kim, C. Hwang, J. Korean Phys. Soc., 59 (2011) 71-74.

[29] M.-C. Wu, Q. Xu, D.W. Goodman, J. Phys. Chem., 98 (1994) 5104-5110.

[30] Y. Pan, H.G. Zhang, D.X. Shi, J.T. Sun, S.X. Du, F. Liu, H.J. Gao, Adv. Mater., 21 (2009) 2777-2780.

[31] W. Moritz, B. Wang, M.L. Bocquet, T. Brugger, T. Greber, J. Wintterlin, S. Gunther, Phys. Rev. Lett., 104 (2010) 136102.

[32] Z. Zhou, F. Gao, D.W. Goodman, Surf. Sci., 604 (2010) L31-L38.

[33] M. Sicot, S. Bouvron, O. Zander, U. Rudiger, Y.S. Dedkov, M. Fonin, Appl. Phys. Lett., 96 (2010) 093115.

[34] J. Coraux, A.T. N'Diaye, C. Busse, T. Michely, Nano Lett., 8 (2008) 565-570.

[35] J. Coraux, A.T. N'Diaye, M. Engler, C. Busse, D. Wall, N. Buckanie, F. Heringdorf, R. van Gastei, B. Poelsema, T. Michely, New J. Phys., 11 (2009) 023006.

[36] A.T. N'Diaye, J. Coraux, T.N. Plasa, C. Busse, T. Michely, New J. Phys., 10 (2008) 043033.

[37] J.H. Gao, N. Ishida, I. Scott, D. Fujita, Carbon, 50 (2012) 1674-1680.

[38] S.-Y. Kwon, C.V. Ciobanu, V. Petrova, V.B. Shenoy, J. Bareño, V. Gambin, I. Petrov, S. Kodambaka, Nano Lett., 9 (2009) 3985-3990.

[39] T.A. Land, T. Michely, R.J. Behm, J.C. Hemminger, G. Comsa, Surf. Sci., 264 (1992) 261-270.

[40] D.E. Starr, E.M. Pazhetnov, A.I. Stadnichenko, A.I. Boronin, S.K. Shaikhutdinov, Surf. Sci., 600 (2006) 2688-2695.

[41] Z. Liang, H. Khosravian, A. Uhl, R.J. Meyer, M. Trenary, Surf. Sci., 606 (2012) 1643-1648.

[42] B. Wang, M.L. Bocquet, S. Marchini, S. Gunther, J. Wintterlin, Phys. Chem. Chem. Phys., 10 (2008) 3530-3534.

[43] D.E. Jiang, M.H. Du, S. Dai, J. Chem. Phys., 130 (2009) 074705.

[44] L. Huang, Y. Pan, L. Pan, M. Gao, W. Xu, Y. Que, H. Zhou, Y. Wang, S. Du, H.J. Gao, Appl. Phys. Lett., 99 (2011) 163107-163103.

[45] Z. Zhou, B.F. Habenicht, Q. Guo, Z. Yan, Y. Xu, L. Liu, D.W. Goodman, Surf. Sci., 611 (2013) 67-73.

[46] S. Marchini, S. Gunther, J. Wintterlin, Phys. Rev. B, 76 (2007) 075429.

[47] D. Martoccia, P.R. Willmott, T. Brugger, M. Bjorck, S. Gunther, C.M. Schleputz, A. Cervellino, S.A. Pauli, B.D. Patterson, S. Marchini, J. Wintterlin, W. Moritz, T. Greber, Phys. Rev. Lett., 101 (2008) 126102.

[48] D. Martoccia, M. Bjorck, C.M. Schleputz, T. Brugger, S.A. Pauli, B.D. Patterson, T. Greber, P.R. Willmott, New J. Phys., 12 (2010) 043028.

[49] H. Zhang, Q. Fu, Y. Cui, D.L. Tan, X.H. Bao, J. Phys. Chem. C, 113 (2009) 8296-8301.

[50] B. Borca, F. Calleja, J.J. Hinarejos, A.L.V. de Parga, R. Miranda, J. Phys.-Condens. Matter, 21 (2009) 134002.

[51] Y. Pan, M. Gao, L. Huang, F. Liu, H.J. Gao, Appl. Phys. Lett., 95 (2009) 093106.

[52] K. Donner, P. Jakob, J. Chem. Phys., 131 (2009) 164701.

[53] E. Sutter, P. Albrecht, B. Wang, M.L. Bocquet, L.J. Wu, Y.M. Zhu, P. Sutter, Surf. Sci., 605 (2011) 1676-1684.

[54] Y. Xu, L. Semidey-Flecha, L. Liu, Z. Zhou, D.W. Goodman, Faraday Discuss., 152 (2011) 267-276.

[55] M. Gyamfi, T. Eelbo, M. Wasniowska, R. Wiesendanger, Phys. Rev. B, 84 (2011) 113403.

[56] T. Brugger, S. Gunther, B. Wang, J.H. Dil, M.L. Bocquet, J. Osterwalder, J. Wintterlin, T. Greber, Phys. Rev. B, 79 (2009) 045407.

[57] K. Katsiev, Y. Losovyj, Z. Zhou, E. Vescovo, L. Liu, P.A. Dowben, D.W. Goodman, Phys. Rev. B, 85 (2012) 195405.

[58] L. Semidey-Flecha, D. Teng, B. Habenicht, D.S. Sholl, Y. Xu, J. Chem. Phys., 138 (2013) 184710.

[59] A.F. Voter, Phys. Rev. B, 34 (1986) 6819-6829.

[60] D.S. Sholl, R.T. Skodje, Phys. Rev. Lett., 75 (1995) 3158.

[61] Z.H. Zhou, F. Gao, D.W. Goodman, Surf. Sci., 604 (2010) L31-L38.

[62] A.F. Voter, Phys. Rev. B, 34 (1986) 6819-6829.

[63] J.M. Wen, S.L. Chang, J.W. Burnett, J.W. Evans, P.A. Thiel, Phys. Rev. Lett., 73 (1994) 2591-2594.

[64] S.C. Wang, G. Ehrlich, Phys. Rev. Lett., 79 (1997) 4234-4237.

[65] J.T. Goldstein, C. Ehrlich, Surf. Sci., 443 (1999) 105-115.

[66] G. Ehrlich, Surf. Sci., 246 (1991) 1-12.

[67] W. Xu, J.B. Adams, Surf. Sci., 339 (1995) 247-257.

[68] K. Stolt, W.R. Graham, G. Ehrlich, J. Chem. Phys., 65 (1976) 3206-3222.

[69] H.W. Fink, G. Ehrlich, Surf. Sci., 150 (1985) 419-429.

[70] A.W. Signor, J.H. Weaver, Phys. Rev. B, 84 (2011) 165441.

[71] L.J. Xu, G. Henkelman, C.T. Campbell, H. Jonsson, Phys. Rev. Lett., 95 (2005) 146103.

[72] L.J. Xu, G. Henkelman, C.T. Campbell, H. Jonsson, Surf. Sci., 600 (2006) 1351-1362.

[73] G. Barcaro, A. Fortunelli, New J. Phys., 9 (2007) 22.

[74] R. Ferrando, A. Fortunelli, J. Phys.-Condens. Matter, 21 (2009) 264001.

[75] L.B. Vilhelmsen, K.S. Walton, D.S. Sholl, J. Am. Chem. Soc., 134 (2012) 12807-12816.

[76] D.S. Sholl, R.T. Skodje, Phys. Rev. Lett., 75 (1995) 3158-3161.

[77] B. Hvolbaek, T.V.W. Janssens, B.S. Clausen, H. Falsig, C.H. Christensen, J.K. Norskov, Nano Today, 2 (2007) 14-18.

[78] A. Sanchez, S. Abbet, U. Heiz, W.D. Schneider, H. Hakkinen, R.N. Barnett, U. Landman, J. Phys. Chem. A, 103 (1999) 9573-9578.

[79] G.C. Bond, D.T. Thompson, Catal. Rev.-Sci. Eng., 41 (1999) 319-388.

[80] M. Haruta, N. Yamada, T. Kobayashi, S. Iijima, J. Catal., 115 (1989) 301-309.

[81] M. Valden, X. Lai, D.W. Goodman, Science, 281 (1998) 1647-1650.

[82] M.S. Chen, D.W. Goodman, Science, 306 (2004) 252-255.

[83] M.M. Schubert, V. Plzak, J. Garche, R.J. Behm, Catal. Lett., 76 (2001) 143-150.

[84] S. Schimpf, M. Lucas, C. Mohr, U. Rodemerck, A. Bruckner, J. Radnik, H. Hofmeister, P. Claus, Catal. Today, 72 (2002) 63-78.

[85] M.A.P. Dekkers, M.J. Lippits, B.E. Nieuwenhuys, Catal. Today, 54 (1999) 381-390.

[86] A.C. Gluhoi, M.A.P. Dekkers, B.E. Nieuwenhuys, J. Catal., 219 (2003) 197-205.

[87] M. Okumura, Y. Kitagawa, K. Yamagcuhi, T. Akita, S. Tsubota, M. Haruta, Chem. Lett., 32 (2003) 822-823.

[88] B.S. Uphade, M. Okumura, S. Tsubota, M. Haruta, Appl. Catal. A-Gen., 190 (2000) 43-50.

[89] P. Landon, P.J. Collier, A.J. Papworth, C.J. Kiely, G.J. Hutchings, Chem. Commun., (2002) 2058-2059.

[90] R. Burch, Phys. Chem. Chem. Phys., 8 (2006) 5483-5500.

[91] H. Sakurai, T. Akita, S. Tsubota, M. Kiuchi, M. Haruta, Appl. Catal. A-Gen., 291 (2005) 179-187.

[92] M.M. Schubert, S. Hackenberg, A.C. van Veen, M. Muhler, V. Plzak, R.J. Behm, J. Catal., 197 (2001) 113-122.

[93] I.X. Green, W.J. Tang, M. Neurock, J.T. Yates, Science, 333 (2011) 736-739.

[94] P.J. Feibelman, Phys. Rev. B, 77 (2008) 165419.

[95] L.B. Vilhelmsen, B. Hammer, Phys. Rev. Lett., 108 (2012) 126101.

[96] D.M. Deaven, K.M. Ho, Phys. Rev. Lett., 75 (1995) 288-291.

[97] L.B. Vilhelmsen, D.S. Sholl, J. Phys. Chem. Lett., 3 (2012) 3702-3706.

[98] T. Liang, B. Devine, S.R. Phillpot, S.B. Sinnott, J. Phys. Chem. A, 116 (2012) 7976-7991.

[99] T.R. Shan, B.D. Devine, J.M. Hawkins, A. Asthagiri, S.R. Phillpot, S.B. Sinnott, Phys. Rev. B, 82 (2010) 235302.

[100] J.G. Yu, S.B. Sinnott, S.R. Phillpot, Phys. Rev. B, 75 (2007) 085311.

[101] A.C.T. van Duin, S. Dasgupta, F. Lorant, W.A. Goddard, J. Phys. Chem. A, 105 (2001) 9396-9409.

[102] H.P. Chen, R.K. Kalia, E. Kaxiras, G. Lu, A. Nakano, K. Nomura, A.C.T. van Duin, P. Vashishta, Z.S. Yuan, Phys. Rev. Lett., 104 (2010) 155502.

[103] A. Nakano, R.K. Kalia, K. Nomura, A. Sharma, P. Vashishta, F. Shimojo, A.C.T. van Duin, W.A. Goddard, R. Biswas, D. Srivastava, Comp. Mater. Sci., 38 (2007) 642-652.

[104] K.I. Nomura, R.K. Kalia, A. Nakano, P. Vashishta, A.C.T. van Duin, W.A. Goddard, Phys. Rev. Lett., 99 (2007) 148303.

[105] Y.K. Shin, T.R. Shan, T. Liang, M.J. Noordhoek, S.B. Sinnott, A.C.T. van Duin, S.R. Phillpot, MRS Bull., 37 (2012) 504-512.

[106] S.V. Zybin, W.A. Goddard, P. Xu, A.C.T. van Duin, A.P. Thompson, Appl. Phys. Lett., 96 (2010) 081918.

[107] J. Yu, S.B. Sinnott, S.R. Phillpot, Philos. Mag. Lett., 89 (2009) 136-144.

[108] T.R. Shan, B.D. Devine, S.R. Phillpot, S.B. Sinnott, Phys. Rev. B, 83 (2011) 115327.

[109] T.R. Shan, B.D. Devine, T.W. Kemper, S.B. Sinnott, S.R. Phillpot, Phys. Rev. B, 81 (2010) 125328.

[110] B. Devine, T.R. Shan, Y.T. Cheng, A.J.H. McGaughey, M. Lee, S.R. Phillpot, S.B. Sinnott, Phys. Rev. B, 84 (2011) 125308.

[111] Y.T. Cheng, T.R. Shan, B. Devine, D. Lee, T. Liang, B.B. Hinojosa, S.R. Phillpot, A. Asthagiri, S.B. Sinnott, Surf. Sci., 606 (2012) 1280-1288.

[112] S. Plimpton, J. Comput. Phys., 117 (1995) 1-19.

[113] LAMMPS, LAMMPS molecular dynamics package; http://lammps.sandia.gov.

[114] L. Gao, J.R. Guest, N.P. Guisinger, Nano Lett., 10 (2010) 3512-3516.

[115] Y. Ogawa, B.S. Hu, C.M. Orofeo, M. Tsuji, K. Ikeda, S. Mizuno, H. Hibino, H. Ago, J. Phys. Chem. Lett., 3 (2012) 219-226.

[116] L. Zhao, K.T. Rim, H. Zhou, R. He, T.F. Heinz, A. Pinczuk, G.W. Flynn, A.N. Pasupathy, Solid State Commun., 151 (2011) 509-513.

[117] K. Toyoda, K. Nozawa, N. Matsukawa, S. Yoshii, J. Phys. Chem. C, 117 (2013) 8156-8160.

[118] M. Vanin, J.J. Mortensen, A.K. Kelkkanen, J.M. Garcia-Lastra, K.S. Thygesen, K.W. Jacobsen, Phys. Rev. B, 81 (2010) 081408.

[119] M. Amft, S. Lebegue, O. Eriksson, N.V. Skorodumova, J. Phys.-Condens. Matter, 23 (2011) 395001.

CHAPTER 2

RH AND AU MONOMERS ON GRAPHENE/RU(0001)

2.1 Introduction

In this Chapter, we investigate and compare the adsorption and diffusion of the adatoms of two metals, Rh and Au (Rh_1 and Au_1), on the graphene/Ru(0001) (denoted as g/Ru(0001)) surface, using periodic density functional theory (DFT) calculations. Both have been observed experimentally to grow in a self-limiting manner, but Rh nucleates into well-dispersed small clusters whereas Au exclusively forms a few large 2D islands, each covering multiple moiré cells [1-3]. In previous studies [4, 5] the potential energy surface (PES) of an adatom on a graphene moiré was sampled along a single linear direction and not in its entirety. To tackle the practical challenges posed by the large size of the graphene moiré unit cell (Figure 2.1a) and the heterogeneity of the surface, we have taken a two-tiered approach by first studying the adsorption and diffusion of Rh_1 and Au_1 in detail on (3×3) model surfaces representing different regions of g/Ru(0001). The results identify the C-top and the C_6 ring center sites to be the key sites for the adsorption and diffusion of Rh_1 and Au_1. We have then carried out an extensive set of large-scale DFT calculations for Rh_1 and Au_1 adsorbed in all the non-equivalent C-top and C_6 ring center sites in the symmetry-irreducible zone of the graphene moiré unit cell of g/Ru(0001) (Figure 2.1a). The resulting PESs, which encompass the entire g/Ru(0001) moiré unit cell, quantitatively demonstrate how each adatom preferentially diffuses across the moiré. The global diffusion barriers are thus estimated to be 0.53 eV for Rh_1 and 0.71 eV for Au_1, which correspond to a global hopping rate between adjacent

moiré cells of 1.10×10^{3} and 9.97×10^{-1} s^{-1} at room temperature, respectively, and are primarily dictated by the global, not the local, corrugation in the PESs.

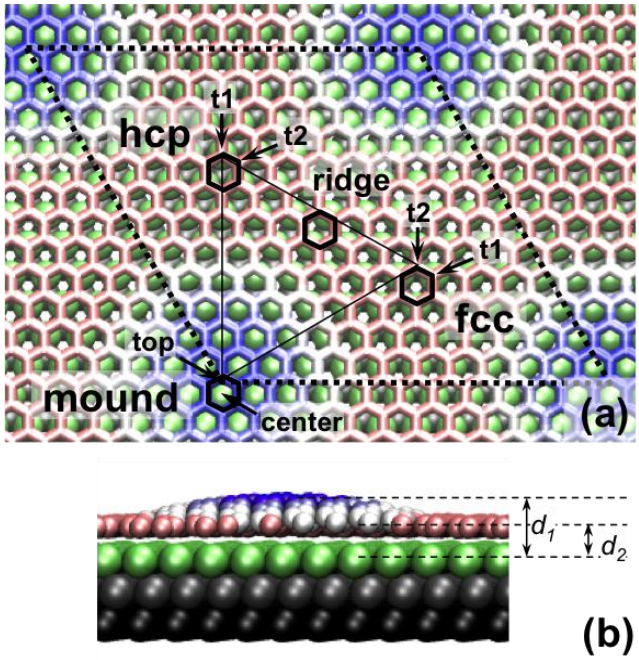

Figure 2.1: Schematic showing the optimized (12×12)-graphene moiré/(11×11)-Ru(0001) surface in (a) top and (b) side views. The top and lower layers of Ru are colored differently, and the C atoms are colored according to their heights, as an aid to the eye. For clarity, the C atoms are shown in the stick model in the top view and the ball model in the side view. In (a), the surface unit cell is outlined by black dashed lines; the symmetry-irreducible zone is indicated by the triangle; the high-symmetry regions are labeled; the high-symmetry C_6 rings represented by (3×3) surfaces are outlined by hexagons with sites labeled. In (b), d_1 and d_2 indicate the heights of the highest and lowest C atoms in the graphene moiré with respect to the top Ru layer at its bulk-truncated position, with d_1 = 3.693 Å; d_2 = 2.156 Å.

Furthermore we have performed Monte Carlo (MC) simulations to demonstrate how different nucleation and growth behavior results from the different mobility of

adatoms. The results suggest that even deposition of atoms across the surface and a lack of diffusion between moiré cells after deposition are key to cluster nucleation with high number density and narrow size distribution, whereas significant transport across moiré cells leads to agglomeration and formation of large particles. When the results of the DFT calculations and MC simulations are considered together with the experimentally observed nucleation and growth behavior of Rh and Au on g/Ru(0001), the possibility of a more mobile Au species than the Au adatom is identified.

2.2 Methods

Periodic DFT calculations were performed using the Vienna *Ab Initio* Simulation Package (VASP) [6-8] in the generalized gradient approximation (GGA-PBE) [9]. The core electrons were described by the PAW method [10, 11], and the Kohn-Sham valence states (including Ru(4d5s), Rh(4d5s), Au(5d6s), C(2s2p)) were expanded in plane wave basis sets up to 400 eV. A first-order Methfessel-Paxton scheme [12] was used to smear the electronic states with a width of 0.1 eV. The optimized Ru lattice constant a = 2.726 Å and c = 4.302 Å and graphene in-plane lattice constant of a = 2.460 Å (corresponding to a C-C bond length of 1.420 Å) were in close agreement with the experimental values (a = 2.706 Å and c = 4.28 Å for Ru; a = 2.46 Å for graphite) and previous DFT results [13-16]. A vacuum space of ca. 13 Å separated neighboring Ru slabs in the z direction to accommodate the graphene moiré. Spin polarization was checked for Rh_1 and Au_1 on all surface models. Both adatoms have residual magnetic moments when adsorbed on freestanding graphene, although the residual moments lower the electronic energy only by ~0.05 eV for Rh_1 and ~0.1 eV for Au_1 and can be ignored for the purpose of understanding the diffusion properties of the adatoms on g/Ru(0001).

The exact periodicity of g/Ru(0001) is still a subject of debate [13, 14, 17-22]. The (12×12)-graphene moiré on (11×11)-Ru(0001) model ("12-on-11", Figure 2.1a) is in close agreement with the majority of experimental evidence for the geometry of the graphene moiré [18, 20, 23-25] and is adopted in this study. The Ru(0001) substrate was modeled by a three-layer slab, with therefore a total of 363 Ru and 288 C atoms in the unit cell. An initially flat sheet of graphene, which was expanded by 1.58% in the *xy* plane to conform to the Ru(0001) surface lattice, was placed over the Ru surface and relaxed into the moiré structure by geometry minimization. After fully relaxing the C and top-layer Ru atoms to below 0.05 eV/Å in all degrees of freedom, the lowest point of the graphene layer was located at 2.156 Å above the position of the un-relaxed, bulk-truncated top Ru layer (Figure 2.1b). The reciprocal space was sampled at the Γ point only.

Small (3×3) unit cells of freestanding graphene and Ru-supported graphene (denoted (3×3) surfaces; Figure 2.2) were used in this study to allow the characteristics of the diffusion of the metal adatoms to be examined in detail. These (3×3) surfaces represent several different high-symmetry C_6 rings in the graphene moiré (highlighted in Figure 2.1). The flat freestanding graphene (18 C atoms) was at the equilibrium lattice constant of 2.460 Å (corresponding to a C-C bond length of 1.420 Å; Figure 2.2a). The Ru-supported graphene consisted of a layer of flat graphene laid on top of a three-layer Ru(0001) slab (18 C and 27 Ru atoms), in which the graphene lattice was stretched by 10.8% from its equilibrium distance of 2.460 to 2.726 Å (corresponding to a C-C bond length of 1.574 Å) to match the lattice size of the Ru(0001) surface. The fcc version exposed the fcc sites on the Ru(0001) surface through the C_6 rings (Figure 2.2b), while

the hcp version exposed the hcp sites on the Ru(0001) surface through the C_6 rings (Figure 2.2c). The ridge version (Figure 2.2d) had the C atoms offset along the direction of the C-C bond by 0.787 Å, i.e., half of the C-C bond length of 1.574 Å. After fully relaxing the C and top-layer Ru atoms to below 0.03 eV/Å, the graphene layer was located on an average at 2.100, 2.120, and 2.093 Å above the position of the un-relaxed, bulk-truncated top Ru layer for the fcc, hcp, and ridge versions. The reciprocal space of the (3×3) surfaces was sampled on a Γ-centered 5×5×1 Monkhorst-Pack *k*-point grid.

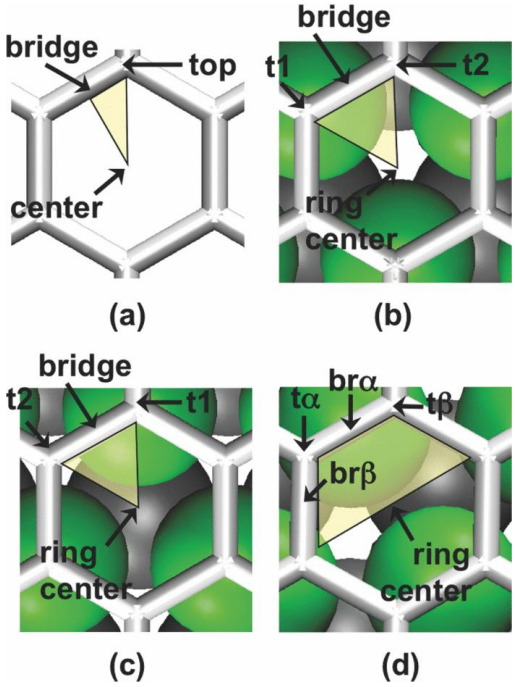

Figure 2.2: Schematics of the (3x3) surfaces: (a) freestanding graphene; (b) fcc, (c) hcp, and (d) ridge versions of Ru(0001)-supported graphene. The symmetry-irreducible zone of each surface is indicated by the shaded region, and the high-symmetry sites are labeled. Graphene is shown as bonds only. Top and second layer Ru atoms are shown as green and grey spheres, respectively.

The adsorption of the adatoms was studied on the graphene side of the slabs only, with the electrostatic potential adjusted accordingly [26]. The graphene and the top layer of Ru were fully relaxed, and the adatom was relaxed only in the *z* direction, for the (3×3) surfaces. For g/Ru(0001), the Ru slab was frozen at the positions when optimized without the adatom; the graphene moiré was fully relaxed; and the adatom was relaxed only in the *z* direction. Geometry optimization was converged such that the forces on all relaxed atoms fell below 0.05 eV/Å in all degrees of freedom. See Appendix A for the results of the convergence tests that we have performed to support the convergence criteria for geometry optimization. The adsorption energy of an adatom on a surface was calculated as $\Delta E = E_{total} - E_{surface} - E_{adatom}$, where E_{total} and $E_{surface}$ are the total energies of the surface with and without the adatom, respectively, and E_{adatom} is the total energy of the isolated metal atom in the gas phase, calculated in a cubic cell 26 Å on each side. A more negative ΔE indicates stronger adsorption. Minimum-energy diffusion paths were identified by examining the calculated PESs of each adatom on the various graphene surfaces. The energies of selected transition states (TS) of diffusion on the (3×3) surfaces were verified using the climbing-image nudged elastic band (CI-NEB) method [27].

Atomic charges were determined using the Bader method [28] and the density-derived electrostatic and chemical charges (DDEC) method described by Manz and Sholl [29, 30]. The Bader method partitions the total electron density into non-overlapping atomic volumes whose surfaces are perpendicular to the electron density gradient. The DDEC method partitions the total electron density into overlapping atomic distributions that are simultaneously optimized to be chemically meaningful and to reproduce the electrostatic potential surrounding a material. Bader charges were calculated using the

code of Henkelman and co-workers [31, 32]. DDEC charges were calculated using the DDEC code available at http://ddec.sourceforge.net/.

2.3 Results and Discussion

2.3.1 Graphene moiré on Ru(0001)

In the optimized 12-on-11 graphene moiré structure on Ru(0001), the highest C atom is in the mound region and is located at 3.693 Å, and the lowest C atom is in the low regions and is located at 2.156 Å (both relative to the top Ru layer at its un-relaxed, bulk truncated position), for a maximum corrugation of 1.537 Å (Figure 2.1b). Experimentally the corrugation height of the graphene moiré on Ru(0001) remains debated. The apparent corrugation measured by STM is observed to change with the bias voltage, being in excess of 1.0 Å at large negative bias but as low as 0.2 Å at large positive bias [17], indicating significant electronic effects. Goodman and coworkers have measured the corrugation in STM to be 1.5 Å at –0.3 V [2, 3]. XRD analysis performed by Martoccia *et al.* [21] and LEED analysis performed by Moritz *et al.* [20] have concluded that the physical corrugation is 0.82 Å and 1.5 Å, respectively, while Borca *et al.* have used He ion diffraction to determine it to be 0.15 Å [22]. For the 12-on-11 structure, GGA-PBE predicts a physical corrugation of 1.5-1.7 Å [4, 14], DFT-D2 predicts 1.195 Å [33], and the optB86b vdW density functional [34] predicts 1.45 Å [35, 36]. Because of the uncertainty in the experimentally measured corrugation of the graphene moiré on Ru(0001) and also a lack of evidence to suggest that vdW corrections would improve the description of the adatom adsorption, vdW interactions are not included in this study.

The graphene moiré on Ru(0001) can be divided into four regions (Figure 2.1a): a protruding mound region, two different low regions, and elsewhere in between that we term the ridge region, although a definite borderline cannot be drawn between them because the positions of the C sub-lattices shift continuously relative to the surface Ru atoms. In the low regions, one of the two C sub-lattices (designated t1) is located directly above the surface Ru atoms, and the other (designated t2) is located either above the hcp sites on the Ru(0001) surface exposing the fcc sites through C_6 rings (designated the fcc region), or above the fcc sites exposing the hcp sites through C_6 rings (designated the hcp region). In the mound region one sub-lattice is located above the fcc sites and the other one is located above the hcp sites. It has been observed that metal atoms deposited on g/Ru(0001) overwhelmingly nucleate into clusters in the fcc region and never in the mound region [1, 37-39]. The different chemical affinity of the fcc and mound regions has also been demonstrated directly using atomic force microscopy recently [40, 41]. It has been suggested that the significant difference in the chemical affinity between the fcc region and the mound region can be attributed to the fact that C atoms in the fcc region undergo sp^3 rehybridization and form metal-C bonds on the t1 sub-lattice and dangling bonds on the t2 sub-lattice primarily from the p_z states, whereas C atoms in the mound region are not electronically perturbed, when compared to the same graphene moiré without the Ru substrate (Figure 2.3) [4, 13, 14]. We have previously shown that Au_1 adsorbed in the fcc region strongly interacts with the Ru substrate through the graphene [3]. Carbon sp^3 rehybridization and through-graphene metal-metal interaction are therefore the underlying mechanism for the enhanced reactivity toward metal adatoms in the fcc region. sp^3 rehybridization and formation of dangling bonds also occur in the hcp

region, but the density of states at the Fermi level is lower (Figure 2.3), which may be a reason for the lower reactivity of the hcp region. Further analysis will be needed to elucidate the connection between the local electronic structure and surface reactivity that quantitatively explains the different reactivity of the two low regions.

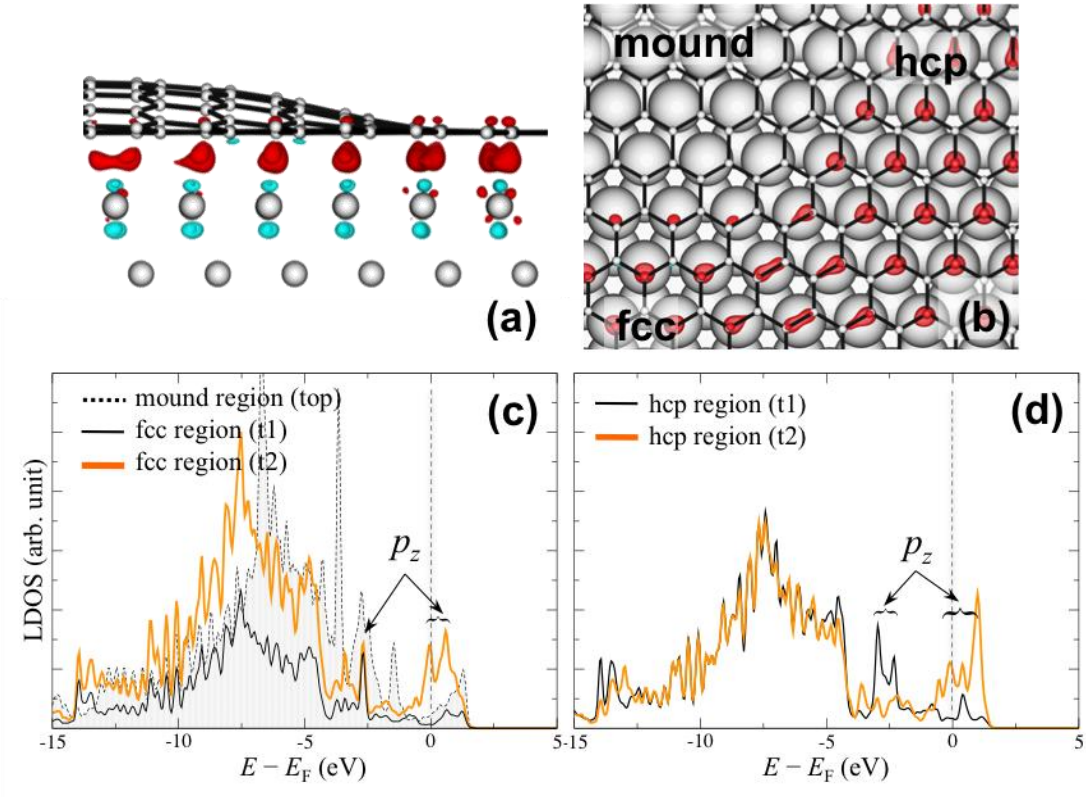

Figure 2.3: (a, b) top and side views of the charge density difference ($\Delta\rho = \rho_{total} - \rho_{Ru} - \rho_{graphene}$) plots for graphene moiré on Ru(0001). The isosurfaces shown are ± 0.008 e/Å^3 (red/dark = density accumulation; blue/light = density depletion). The graphene moiré is shown as a hexagonal wire network. (c, d) Local density of states (LDOS) of the *p* states of several C atoms in g/Ru(0001). See Figure 2.1 for site designation. The Fermi level is indicated by a vertical dashed line. The states near the Fermi level primarily composed of p_z states are indicated for t1 and t2.

The graphene moiré on Ru(0001) gains an average of 0.039 electrons per C atom according to Bader charge analysis and loses an average of 0.014 electrons per C atom according to DDEC charge analysis. Both of these charge analysis methods indicate there is little charge transfer between the metal and graphene on a per-atom basis. Experimentally it has been observed that the C π states are downshifted on Ru(0001), which suggests that the graphene becomes p-doped [42]. The surface work function is calculated to be 3.57 eV, consistent with the 3.5~3.9 eV reported in previous theoretical and experimental studies [4, 14, 42].

2.3.2 Adsorption and diffusion of Rh_1 on the (3×3) model surfaces

Because the mound region is located at up to 3.693 Å above the Ru(0001) surface and is effectively decoupled from it, we use freestanding graphene to represent it. Freestanding graphene (Figure 2.2a) has twelve-fold symmetry, so we sampled this surface in a triangular symmetry-irreducible zone of the C_6 ring at the C top, C-C bridge, and C_6 center sites, plus 4 different points inside the zone, for a total sampling density of 61 points per C_6 ring. The resultant potential energy surfaces (PESs) are shown in Figure 2.4a. The most stable adsorption site is the C_6 ring center site (ΔE = –1.52 eV).

The (3×3) Ru(0001)-supported graphene surfaces representing the fcc and hcp regions of the graphene moiré have six-fold symmetry in the C_6 ring (Figures 2.2b and 2.2c). These surfaces are sampled in the triangular symmetry-irreducible zone at the t1, t2, bridge, and ring center sites, plus 6 different points inside the zone, for a total sampling density of 49 points per C_6 ring. The resulting PESs are shown in Figures 2.4b (fcc) and 2.4c (hcp). The minimum-energy adsorption site on both surfaces is slightly off the t1 site toward the center of the ring, with ΔE = –2.56 and –2.27 eV, respectively. On

the (3×3) ridge surface (Figure 2.2d), the C_6 ring has a lower, two-fold symmetry. The symmetry-irreducible zone of this surface is sampled at two different top and bridge sites (tα/tβ and brα/brβ; see Figure 2.2d), and the ring center site, plus 14 different points, for a total sampling density of 38 points per C_6 ring. The top sites are all local maxima on this surface (ΔE = –1.83 eV in the tα site and –1.89 eV in the tβ site; Figure 2.4d). A low energy corridor occurs across the C_6 ring, with the minimum energy occurring at the brα position (ΔE = –2.16 eV).

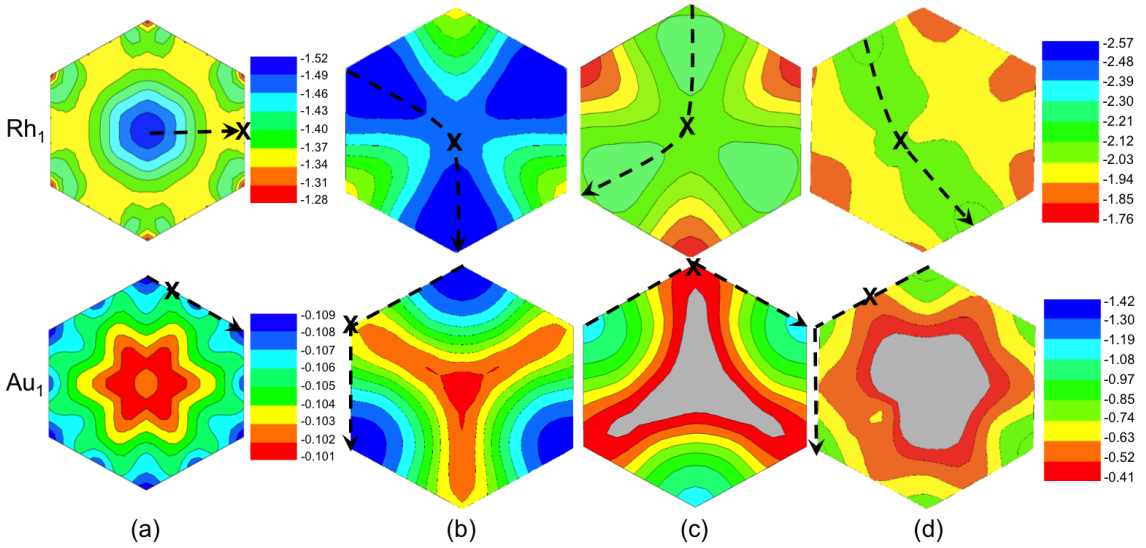

Figure 2.4: PESs for Rh_1 and Au_1 on the (3×3) surfaces: (a) freestanding graphene; (b) fcc, (c) hcp, and (d) ridge versions of Ru(0001)-supported graphene. Upper panel is for Rh_1, and lower panel is for Au_1. Contours are generated based on interpolation as an aid to the eye only. The minimum-energy diffusion path between adjacent local minima is indicated on each surface for each adatom by the dashed line. The corresponding transition state is indicated by "X".

The detailed PESs show that on the (3×3) freestanding graphene (Figure 2.4a), the diffusion between adjacent C_6 rings preferentially occurs across the C-C bond at the bridge site, with a barrier of E_a = 0.17 eV. On the (3×3) fcc (Figure 2.4b) and hcp (Figure 2.4c) surfaces, the minimum-energy diffusion path goes through the ring center, with E_a = 0.16 and 0.15 eV respectively. On the fcc surface we have verified the ring center to be the minimum-energy TS for local diffusion using CI-NEB calculations, and the energy of the CI-NEB TS agrees with that of the ring center site on the PES to within 0.03 eV. On the ridge surface (Figure 2.4d), the minimum-energy diffusion path between two adjacent local minima (the brα sites) runs across the C_6 ring, slightly off the center, with E_a = 0.15 eV.

2.3.3 Adsorption and diffusion of Au_1 on the (3×3) model surfaces

The PESs for Au_1 calculated on the same set of (3×3) surfaces are shown in Figure 2.4. The most stable sites are the top site on the freestanding graphene (ΔE = –0.11 eV; Figure 2.4a); the t2 site on the fcc and hcp surfaces (ΔE = –1.42 and –1.13 eV respectively; Figures 2.4b and 2.4c); and the tβ site on the ridge surface (ΔE = –0.92 eV; Figure 2.4d). Qualitatively the Au_1 PESs have the opposite topology of the Rh_1 PESs. Since the ring center site is usually the local maximum, Au_1 diffuses preferentially along the C-C bonds, unlike Rh_1. This is consistent with the closed d shell of the Au atom and the inability of the Au atom to coordinate simultaneously to as many ligands, including π-bonding to arenes, as Rh is able to. On the freestanding graphene (Figure 2.4a), diffusion preferentially occurs between adjacent top sites with a barrier of E_a = 0.002 eV. The very small diffusion barriers for Au_1 and Rh_1 on freestanding graphene are in agreement with previous calculations by Yazyev *et al.* [43]. On the fcc (Figure 2.4b) and

hcp (Figure 2.4c) surfaces, Au_1 preferentially diffuses between adjacent t2 sites via the t1 site, with E_a = 0.76 and 0.66 eV respectively. On the fcc surface the t1 site has also been verified to be the minimum-energy TS for local diffusion using CI-NEB calculations, and the energy of the CI-NEB TS agrees with that of the t2 site on the PES to within 0.02 eV. On the ridge surface (Figure 2.4d), Au_1 diffusion preferentially occurs between two adjacent tβ sites with E_a = 0.32 eV.

2.3.4 Coarse-grained PESs for Rh_1 and Au_1 on g/Ru(0001)

The PESs for Rh_1 and Au_1 on the (3×3) model surfaces suggest that the key local minima and transition states for diffusion are either the C-top site or the C_6 ring center site; or near a top site or the center site, in which case the energetic error introduced by approximation with the nearest top or center site is small. For instance, on the ridge surface, the transition state for Rh_1 diffusion is located slightly off the ring center and is less than 0.1 eV lower in energy than the center site, and the transition state for Au_1 diffusion is located at a bridge site that is 0.2 eV higher in energy than the nearby tα site (Figure 2.4c). As a reasonable first approximation, one can limit the computational effort by constructing a coarse-grained PES that includes only the top and ring center sites. There are a total of 91 non-equivalent C-top and C_6 ring center sites in the triangular symmetry-irreducible zone of the graphene moiré (indicated in Figure 2.1a), which nonetheless still require a significant amount of computing resources. We point out that at least 10 times more calculations would be needed to obtain a PES at the same level of resolution as on the (3×3) model surfaces.

The resulting coarse-grained PESs for Rh_1 and Au_1 on g/Ru(0001) are shown in Figure 2.5. They show how the metal-C bond strength varies continuously with position

on g/Ru(0001). The adsorption of Rh_1 is overall the most stable in the fcc region, less stable in the hcp region, and least stable in the mound region. The global minimum-energy adsorption site is a t1 site near the center of the fcc region (labeled "A" in Figure 2.5a; ΔE = –2.40 eV). The adsorption of Au_1 is likewise the most stable in the fcc region and least stable in the mound region, although the PES for Au_1 is somewhat flatter across the fcc and hcp regions than that for Rh_1. The global minimum-energy adsorption site is the t2 site at the center of the fcc region (labeled "D" in Figure 2.5b; ΔE = –1.57 eV). Wang *et al.* reported the most stable site on g/Ru(0001) for Au_1 to be a t2 site in the fcc region with ΔE = –1.40 eV [4], with which our value is in good agreement. Improving upon the previous work, these PESs provide a comprehensive view of how the fcc region presents a deeper and wider basin than the hcp region on the graphene moiré/Ru(0001) for the adatoms, which is consistent with the experimental observation that Rh and Au [1], and indeed other metals including Pt, Ru, Co, and Pd [1, 37, 39], all preferentially nucleate in the fcc region on g/Ru(0001) at the lowest coverage. Nucleation outside the fcc region is only possible at very low surface temperature [37, 44]. The PESs also show how the metal-C bond strength varies systematically with position, which provides important information for estimating the maximum size of a nucleating single-layer metal cluster before the onset of multi-layer growth [45].

Rh_1 in site A pushes the C atom beneath it downward slightly by 0.032 Å from its initial position in the clean graphene moiré, forming a Rh-C bond of 2.007 Å. Au_1 in site B pulls the C atom beneath it upward by 0.359 Å, forming an Au-C bond of 2.144 Å, which is also in agreement with Wang *et al*. who reported that Au_1 in the most stable site pulls the C atom beneath 0.35 Å above its initial position with a Au-C bond length of

2.12 Å [4]. Changes of less than 0.1 Å are seen in the vertical position of the C atoms beneath the adatoms in the mound region.

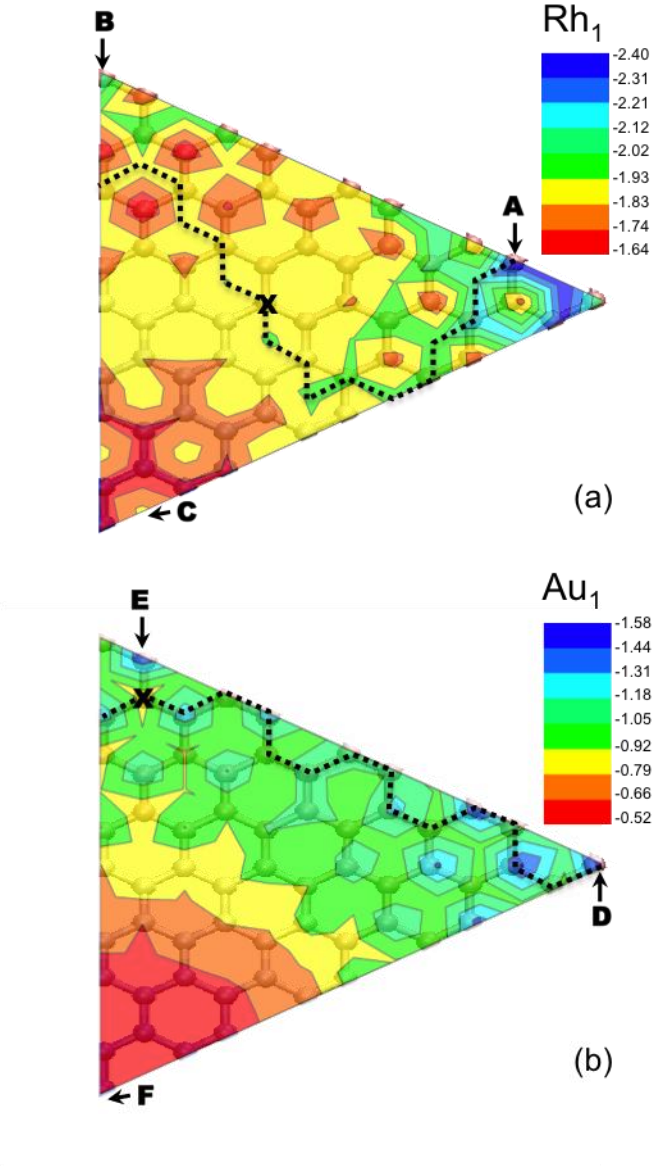

Figure 2.5: Potential energy surfaces (PESs) for (a) Rh_1 and (b) Au_1 sampled at the top and ring center sites in the symmetry-irreducible zone of the full g/Ru(0001) surface. Contours are generated based on interpolation and overlaid onto the graphene network as an aid to the eye only. The minimum-energy diffusion path for each adatom is marked by a dashed line. Key adsorption sites in high-symmetry regions ("A", "B", "C" for Rh_1; "D", "E", and "F" for Au_1), and the highest-energy site on each path ("X"), are labeled; see text for detail and the Appendix material for the adsorption energy at each site.

Using the coarse-grained PESs we can determine the minimum-energy diffusion paths for Rh_1 and Au_1 from the global minimum-energy adsorption site in the fcc region of one moiré cell to that in an adjacent moiré cell. The diffusion paths are determined based the following rules: Starting at the global minimum-energy adsorption site in the fcc region (site A or D in Figure 2.5), the adatom travels to the most stable of the nearest-neighbor C-top or C_6 ring center site, and the process is repeated until the adatom reaches any point along the boundary of the triangular symmetry-irreducible zone that connects the hcp and mound regions. A less-than-most-stable site may be visited if by doing so the adatom can avoid visiting an even less stable site. Based on the insights gained from the (3×3) model surfaces, we constrain Rh_1 to hop between top and ring center sites, and Au_1 to traverse along C-C bonds only.

The minimum-energy diffusion paths thus identified and the highest-energy site along each path are marked in Figure 2.5. Alternate paths exist with only somewhat higher global barriers, which can be accessed with increasing probability at increasing temperature. The highest-energy site on the diffusion path for Rh_1 occurs in the middle of the triangular zone with ΔE = –1.87 eV, giving a global diffusion barrier of E_a = (–1.87) – (–2.40) = 0.53 eV relative to the global minimum-energy adsorption site in the fcc region. We describe the diffusion of the adatom from the global minimum-energy adsorption site in one moiré cell to that in another in the way usually done for local hopping, by assuming a rate of the Arrhenius form, $r = A \cdot \exp(-E_a/kT)$. The pre-exponential factor is taken to be $A = 10^{12}$ s^{-1}, i.e., 1/10 of that for local diffusion, 10^{13} s^{-1} [46]. The estimated global hopping rate between fcc regions in adjacent moiré cells at room temperature (298 K) is therefore 1.10×10^3 s^{-1} for Rh_1.

The highest-energy site on the diffusion path for Au_1 occurs in the hcp region with ΔE = –0.86 eV. The global diffusion barrier for Au_1 is therefore E_a = (–0.86) – (–1.57) = 0.71 eV, and the global hopping rate for Au_1 is 9.97×10^{-1} s^{-1}, over a thousand times slower than Rh_1. The preferred direction of hopping is mostly along the fcc-hcp line for Au_1, but by deviating closer to the mound region Rh_1 lowers the diffusion barrier by a few hundredths of an eV. As mentioned before, the (3×3) surfaces suggest that the energy of the global diffusion transition state may be under-estimated by up to 0.2 eV by not including bridge sites in the coarse-grained PES for Au_1, and over-estimated by up to 0.1 eV for Rh_1 if a local saddle point occurs off-center or off-top. Nonetheless this would not change the conclusion that Rh_1 has a lower global diffusion barrier than Au_1 on g/Ru(0001). That the diffusion barrier of Au_1 is higher than that of Rh_1 even though the minimum adsorption energy of Au_1 (–1.57 eV) is weaker than that of Rh_1 (–2.40 eV) might appear counterintuitive. The conventional rule of thumb states that the diffusion barrier is approximately 0.1~0.2 times the adsorption energy [47], but as noted previously by Nilekar *et al.* this rule does not reflect any fundamental physical principle [48].

It is instructive to compare the coarse-grained PESs with the PESs calculated on the (3×3) model surfaces. The global minimum ΔE, which is located in the fcc region, is closely captured by the (3×3) fcc surface, being 0.17 eV too stable for Rh_1 and 0.15 eV too unstable for Au_1 compared to the full moiré surface results (Table 2.1). The charge on each adatom, on which the Bader and DDEC methods agree closely, is also closely captured by the (3×3) fcc surface (Table 2.1). Under-prediction is seen for both adatoms using the freestanding graphene, indicating that the mound region of the graphene moiré is clearly chemically different from freestanding graphene, but for the diffusion of both

adatoms the mound region is of no consequence. Furthermore, we note that the energetic difference between the transition state identified on the (3×3) ridge surface and the most stable site on the (3×3) fcc surface comes to 0.56 eV for Rh_1 and 0.81 eV for Au_1. These values closely reflect the global diffusion barriers determined using the coarse-grained PESs on the full graphene moiré surface (0.53 and 0.71 eV, respectively). These smaller diffusion barriers result in a 3-times (49-times) faster hopping rate for Rh_1 (Au_1), but the hopping rate for Rh_1 remains orders of magnitude higher than that for Au_1. This suggests that this particular set of (3×3) model surfaces may be used to rapidly estimate the global diffusion barriers for other adatoms on g/Ru(0001), and produce at least a qualitative trend for the facility of diffusion of different adatoms on the graphene moiré, at significantly less computational cost than required to tackle the full moiré surface.

Table 2.1: Adsorption energies (ΔE, in eV) and charge of Rh_1 and Au_1 on the graphene moiré/Ru(0001) surface and on the (3×3) model surfaces of freestanding graphene and Ru-supported graphene.

moiré site	ΔE	Bader	DDEC	(3×3) / site	ΔE	Bader	DDEC
Rh_1							
A / t1	-2.40	+0.23	+0.12	fcc / off-t1	-2.56	+0.32	+0.21
B / t1	-2.14			hcp / off-t1	-2.27		
C / ring center	-1.86			freestanding / ring center	-1.52		
Au_1							
D / t2	-1.57	-0.12	-0.18	fcc / t2	-1.42	-0.09	-0.12
E / t2	-1.43			hcp / t2	-1.13		
F / top	-0.53			freestanding / top	-0.11		

See Figure 2.2 for site designations on the (3×3) model surfaces, and Figure 2.5 for site designations on g/Ru(0001).

2.3.5 Statistical analysis

Our DFT results thus indicate a considerably faster hopping rate for Rh_1 than for Au_1 on g/Ru(0001), particularly at low to moderate temperatures. To explore the consequences of this observation we have performed lattice-based Monte Carlo (MC) simulations. The graphene moiré unit cell is represented as a (12×12) lattice of identical sites. The simulation surface contains a total of 4 moiré cells with 576 identical sites. We randomly deposit 28 atoms (~0.05 ML) onto this surface, with each atom having a

probability of ¼ of being deposited in a given moiré cell. Only monomer hopping is considered in the simulation. An atom always binds to a site where there is already an atom in a nearest neighbor site, but the probability of sticking to a site without any nearest-neighbor atom, α, is varied in the simulations.

In this context, α is varied to represent different characteristic diffusion lengths. First we stipulate that there is no diffusion across moiré cell boundaries and that all atoms deposited into a moiré cell stay in that cell and form one cluster, corresponding to $\alpha = 1$. The resulting probability mass function (pmf) is plotted in Figure 2.6a. Under the given assumptions, the cluster size should follow a binomial distribution, and the probability of observing a cluster of size k after deposition of n atoms is given by $P(k) = C_n^k \, p^k \, (1 - p)^{n-k}$ for $k = 0, 1, \ldots, n$, where $C_n^k = n! / (k! \cdot (n-k)!)$, and p is the probability of an atom falling into a moiré cell being considered. The cluster size with the highest probability to occur is therefore 7 atoms, that is, 28 atoms divided evenly amongst the 4 moiré cells. The results of the MC simulations closely reflect this (Figure 2.6a). When α decreases to 0.1 (Figure 2.6b), which is equivalent to atoms having longer characteristic diffusion lengths, the peak in the cluster size distribution is still located at around 7 atoms but visibly broadened. When α is significantly smaller still (Figure 2.6c), the peak cluster size distribution around 7 atoms disappears completely and much larger clusters as well as empty moiré cells appear. These results suggest that even deposition of atoms and a lack of diffusion across moiré cells after deposition are important for cluster nucleation with high number density and narrow size distribution.

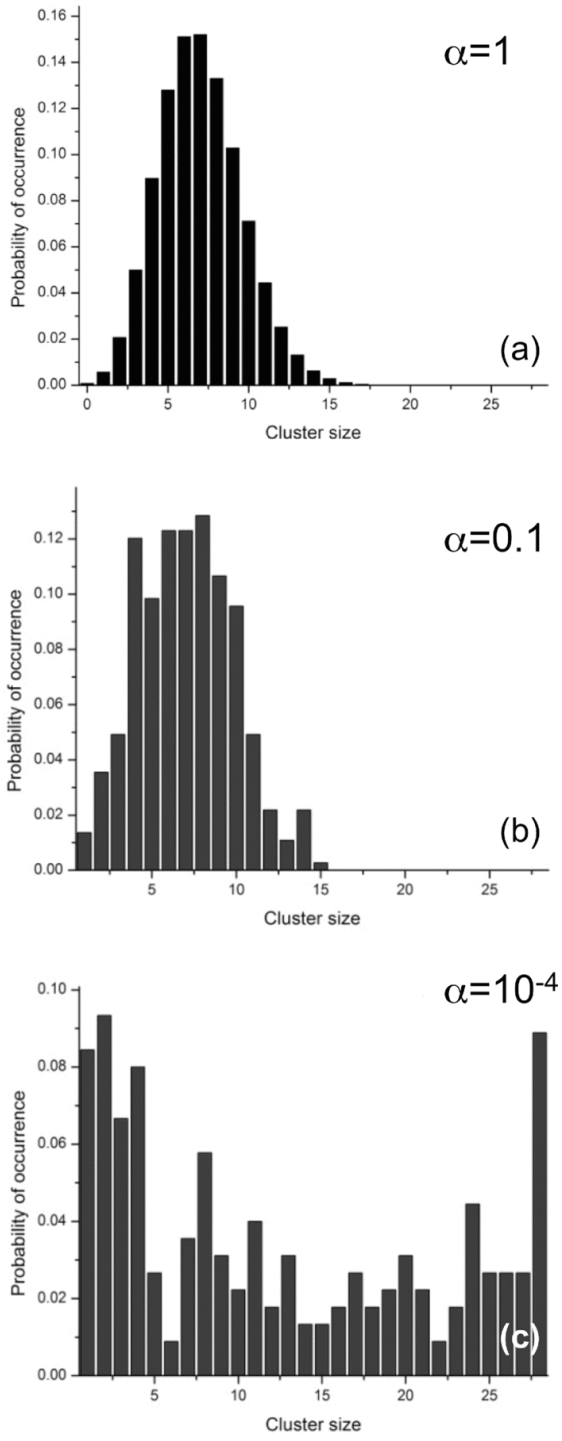

Figure 2.6: Simulation results for the probability mass function of 0.05 ML of adatom deposited on g/Ru(0001). (a) $\alpha = 1$ (following binomial distribution); (b) $\alpha = 0.1$; (c) $\alpha = 10^{-4}$. Results are based on 100 simulations for each value of α.

A limited-diffusion nucleation mode is consistent with the uniform Ir clusters formed at low coverage on g/Ir(111) [49], but inconsistent with the nucleation and growth behavior of Rh and Au deposited on graphene moiré/Ru(0001). The binomial distribution would imply that a cluster is found in every moiré cell, which is not what is observed for Rh. Zhou *et al.* [1] have reported that Rh deposited on g/Ru(0001) at room temperature occupies only 10~20% of all the moiré cells. The α for Rh is clearly not unity. Au, on the other hand, forms a handful of large 2D Au islands, with the number density being far lower than that of the Rh clusters at identical coverages [1-3]. Considering the results of the MC simulations above, one would conclude that α for Au should be further from unity than α of Rh is. The DFT-calculated global hopping rates for Rh_1 and Au_1 on g/Ru(0001), however, indicate that Rh_1 has a much longer characteristic diffusion length than Au_1. This apparent contradiction suggests that it is insufficient to consider the adatom as the sole diffusing species in explaining the nucleation and growth behavior of at least Au deposited on g/Ru(0001). Previous studies have suggested that small metal clusters such as dimers, trimers, and tetramers can have higher surface mobility than the adatom (e.g. Pd, Ca, and Li on MgO(100) [50-53]; Cu on Ag(111) [54]). The results of studying Rh and Au dimers and trimers on g/Ru(0001) are discussed in Chapter 4.

2.4 Conclusions

An extensive set of periodic density functional theory calculations were performed to investigate the adsorption and diffusion of the Rh and Au adatom on the (12×12)-graphene moiré on (11×11)-Ru(0001). By analyzing detailed potential energy surfaces (PESs) for Rh_1 and Au_1 on small (3×3) model surfaces representing high-

symmetry regions on g/Ru(0001), the C-top and C_6 ring center sites were identified to be the key sites in the diffusion of the adatoms. Each adatom adsorbed in all 91 non-equivalent C-top and C_6 ring center sites in the symmetry-irreducible zone of the graphene moiré unit cell on g/Ru(0001) was calculated directly, yielding a coarse-grained PES. These PESs, which encompass the full g/Ru(0001) surface, demonstrate that the global minimum-energy adsorption sites for both Rh_1 and Au_1 are located in the fcc region and the global maximum located in the mound region, and that the hcp region represents a smaller and shallower energy basin than the fcc region, all of which are consistent with the experimentally observed preferential nucleation in the fcc region by Rh and Au on g/Ru(0001). The lowest adsorption energy is –2.40 eV for Rh_1 and –1.57 eV for Au_1, both found in the fcc region.

The minimum-energy global diffusion path between fcc regions of adjacent moiré cells on g/Ru(0001) runs nearly directly between the fcc and hcp regions for Au_1, but deviates toward the mound region for Rh_1. The global diffusion barriers are 0.53 eV for Rh_1 and 0.71 eV for Au_1, corresponding to a hopping rate between fcc regions of adjacent moiré cells of 1.10×10^{3} and 9.97×10^{-1} s^{-1} at room temperature, respectively. The consequences of different mobility of adatoms to cluster nucleation and growth were explored by performing Monte Carlo-based statistical analysis. It was demonstrated that even deposition coupled with a lack of transport across moiré cells is key to maximizing cluster number density and size uniformity, whereas significant transport across moiré cells leads to agglomeration and formation of large particles. However, experimentally Rh has been observed to form clusters at greater number density than Au on g/Ru(0001) [1]. The apparent discrepancy between the experiment and the clearly greater mobility of

Rh_1 than Au_1 as predicted by theory suggests the need to take additional diffusing species, such as larger clusters, into account in understanding the nucleation and growth behavior of Au.

2.5 References

[1] Z. Zhou, F. Gao, D.W. Goodman, Surf. Sci., 604 (2010) L31-L38.

[2] L. Liu, Z. Zhou, Q. Guo, Z. Yan, Y. Yao, D.W. Goodman, Surf. Sci., 605 (2011) L47-L50.

[3] Y. Xu, L. Semidey-Flecha, L. Liu, Z. Zhou, D.W. Goodman, Faraday Discuss., 152 (2011) 267-276.

[4] B. Wang, S. Gunther, J. Wintterlin, M.L. Bocquet, New J. Phys., 12 (2010) 043041.

[5] O.V. Yazyev, A. Pasquarello, Phys. Rev. B, 82 (2010) 045407.

[6] G. Kresse, J. Hafner, Phys. Rev. B, 49 (1994) 14251-14269.

[7] G. Kresse, J. Furthmuller, Comp. Mater. Sci., 6 (1996) 15-50.

[8] G. Kresse, J. Furthmuller, Phys. Rev. B, 54 (1996) 11169-11186.

[9] J.J. Perdew, K. Burke, M. Ernzerhof, Phys. Rev. Lett., 77 (1996) 3865.

[10] P.E. Blochl, Phys. Rev. B, 50 (1994) 17953-17979.

[11] G. Kresse, J. Joubert, Phys. Rev. B, 59 (1999) 1758-1775.

[12] M. Methfessel, A.T. Paxton, Phys. Rev. B, 40 (1989) 3616-3621.

[13] B. Wang, M.L. Bocquet, S. Marchini, S. Gunther, J. Wintterlin, Phys. Chem. Chem. Phys., 10 (2008) 3530-3534.

[14] D.E. Jiang, M.H. Du, S. Dai, J. Chem. Phys., 130 (2009) 074705.

[15] K.T. Chan, J.B. Neaton, M.L. Cohen, Phys. Rev. B, 77 (2008) 235430.

[16] L.B. Hu, X.R. Hu, X.B. Wu, C.L. Du, Y.C. Dai, J.B. Deng, Phys. B-Condens. Matter, 405 (2010) 3337-3341.

[17] A.L. Vázquez de Parga, F. Calleja, B. Borca, M.C.G. Passeggi, J.J. Hinarejos, F. Guinea, R. Miranda, Phys. Rev. Lett., 100 (2008) 056807.

[18] D. Martoccia, P.R. Willmott, T. Brugger, M. Bjorck, S. Gunther, C.M. Schleputz, A. Cervellino, S.A. Pauli, B.D. Patterson, S. Marchini, J. Wintterlin, W. Moritz, T. Greber, Phys. Rev. Lett., 101 (2008) 126102.

[19] Y. Pan, H.G. Zhang, D.X. Shi, J.T. Sun, S.X. Du, F. Liu, H.J. Gao, Adv. Mater., 21 (2009) 2777-2780.

[20] W. Moritz, B. Wang, M.L. Bocquet, T. Brugger, T. Greber, J. Wintterlin, S. Gunther, Phys. Rev. Lett., 104 (2010) 136102.

[21] D. Martoccia, M. Bjorck, C.M. Schleputz, T. Brugger, S.A. Pauli, B.D. Patterson, T. Greber, P.R. Willmott, New J. Phys., 12 (2010) 043028.

[22] B. Borca, S. Barja, M. Garnica, M. Minniti, A. Politano, J.M. Rodriguez-Garcia, J.J. Hinarejos, D. Farias, A.L.V. de Parga, R. Miranda, New J. Phys., 12 (2010) 093018.

[23] M.-C. Wu, Q. Xu, D.W. Goodman, J. Phys. Chem., 98 (1994) 5104-5110.

[24] S. Marchini, S. Gunther, J. Wintterlin, Phys. Rev. B, 76 (2007) 075429.

[25] Y. Pan, D.X. Shi, H.J. Gao, Chinese Phys., 16 (2007) 3151-3153.

[26] J. Neugebauer, M. Scheffler, Phys. Rev. B, 46 (1992) 16067-16080.

[27] G. Henkelman, B.P. Uberuaga, H. Jonsson, J. Chem. Phys., 113 (2000) 9901-9904.

[28] R.F.W. Bader, Atoms in Molecules - A Quantum Theory, Oxford University Press, Oxford, 1990.

[29] T.A. Manz, D.S. Sholl, J. Chem. Theory Comput., 6 (2010) 2455-2468.

[30] T.A. Manz, D.S. Sholl, J. Chem. Theory Comput., 8 (2012) 2844-2867.

[31] G. Henkelman, A. Arnaldsson, H. Jónsson, Comput. Mat. Sci., 36 (2006) 254.

[32] W. Tang, E. Sanville, G. Henkelman, J. Phys.-Condens. Matter, 21 (2009) 084204.

[33] D. Stradi, S. Barja, C. Díaz, M. Garnica, B. Borca, J.J. Hinarejos, D. Sánchez-Portal, M. Alcamí, A. Arnau, A.L. Vázquez de Parga, R. Miranda, F. Martín, Phys. Rev. Lett., 106 (2011) 186102.

[34] J. Klimes, D.R. Bowler, A. Michaelides, Phys. Rev. B, 83 (2011) 195131.

[35] B.F. Habenicht, Y. Xu, L. Liu, Graphene moiré supported metal clusters for model catalysis studies, in: Z. Chen, D. Jiang (Eds.) Graphene Chemistry: Theoretical Perspectives, Wiley, 2013.

[36] Z. Zhou, B.F. Habenicht, Q. Guo, Z. Yan, Y. Xu, L. Liu, D.W. Goodman, Surf. Sci., 611 (2013) 67-73.

[37] K. Donner, P. Jakob, J. Chem. Phys., 131 (2009) 164701.

[38] Y. Pan, M. Gao, L. Huang, F. Liu, H.J. Gao, Appl. Phys. Lett., 95 (2009) 093106.

[39] E. Sutter, P. Albrecht, B. Wang, M.L. Bocquet, L.J. Wu, Y.M. Zhu, P. Sutter, Surf. Sci., 605 (2011) 1676-1684.

[40] E.N. Voloshina, Y.S. Dedkov, S. Torbrugge, A. Thissen, M. Fonin, Appl. Phys. Lett., 100 (2012) 241606.

[41] E.N. Voloshina, E. Fertitta, A. Garhofer, F. Mittendorfer, M. Fonin, A. Thissen, Y.S. Dedkov, Sci. Rep., 3 (2013) 1072.

[42] T. Brugger, S. Gunther, B. Wang, J.H. Dil, M.L. Bocquet, J. Osterwalder, J. Wintterlin, T. Greber, Phys. Rev. B, 79 (2009) 045407.

[43] O.V. Yazyev, A. Pasquarello, Phys. Rev. B, 82 (2010) 045407.

[44] A.T. N'Diaye, T. Gerber, C. Busse, J. Myslivecek, J. Coraux, T. Michely, New J. Phys., 11 (2009) 103045.

[45] P.J. Feibelman, Phys. Rev. B, 80 (2009) 085412.

[46] D. Teng, D.S. Sholl, Surf. Sci., (2014) (in press).

[47] J.V. Barth, Surf. Sci. Rep., 40 (2000) 75-149.

[48] A.U. Nilekar, J. Greeley, M. Mavrikakis, Angew. Chem. Int. Edit., 45 (2006) 7046-7049.

[49] A.T. N'Diaye, S. Bleikamp, P.J. Feibelman, T. Michely, Phys. Rev. Lett., 97 (2006) 215501.

[50] L. Xu, G. Henkelman, C.T. Campbell, H. Jonsson, Phys. Rev. Lett., 95 (2005) 146103.

[51] L. Xu, G. Henkelman, C.T. Campbell, H. Jonsson, Surf. Sci., 600 (2006) 1351-1362.

[52] L. Xu, G. Henkelman, Phys. Rev. B, 82 (2010) 115407.

[53] L. Xu, G. Henkelman, Phys. Rev. B, 77 (2008) 205404.

[54] A.W. Signor, J.H. Weaver, Phys. Rev. B, 84 (2011) 165441.

CHAPTER 3

4D AND 5D METAL MONOMERS ON GRAPHENE/RU(0001)

3.1 Introduction

Graphene has been synthesized on several metal surfaces [1], including Co(0001) [2], Ni(111) [3, 4], Ru(0001) [5-11], Rh(111) [12], Ir(111) [13-15], Pd(111) [16, 17], Cu(111) [18, 19], and Pt(111) [20]. On these surfaces, except Co(0001) and Ni(111), graphene develops a moiré superstructure as a consequence of a sufficiently large mismatch between the lattice constants of graphene and the metal surface. Here we take the graphene moiré on Ru(0001) as an example. The graphene moiré on Ru(0001) can be grown to continuous, micron-scale size domains without defects or interruption by steps [5-11, 21] and is stable in air up to 500 K [10, 22], which makes it a potential support material for model catalysts under mild conditions. The graphene moiré is seen in scanning tunneling microscopy (STM) as periodic arrays of regions with different contrasts (Figure 3.1) [5, 6, 23-25].

The pioneering work by N'Diaye *et al.* demonstrated that the graphene moiré formed on the Ir(111) surface (denoted as g/Ir(111)) can function as a template for metal nanoparticle formation. Super-lattices of Ir clusters with highly uniform size formed from Ir atoms vapor-deposited on g/Ir(111) were reported [26], followed by super-lattices of clusters of Pt and W, and of Re and Au under appropriate conditions [27]. An initial nucleation phase was seen in which the number density of Ir clusters grew with increasing amount of Ir atoms deposited but the average cluster size remained constant. The percentage of the moiré cells that are each occupied by an individual cluster (the

filling factor) reached 100% at ca. 0.05 ML, corresponding to an average size of 6~7 atoms per cluster. Further deposition increased the size of existing clusters [26].

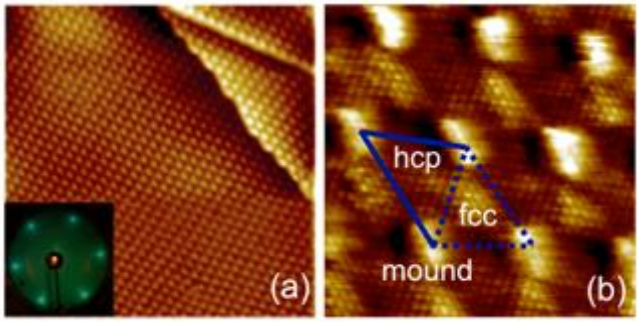

Figure 3.1: (a) STM image of single-layer graphene on Ru(0001) (V_{sample} = +0.1 V, $I_{tunneling}$ = 0.2 nA, 100×100 nm^2) with a typical low energy electron diffraction pattern shown in inset. Reproduced with permission from [24], © 2012 by the American Physical Society. (b) Zoomed in STM image (V_{sample} = –0.3 V, $I_{tunneling}$ = 1.0 nA, 8×8 nm^2) with the moiré supercell and its different regions indicated. Both STM images were obtained at room temperature.

Potentially the deposited metal, the substrate metal, and the graphene-substrate coupling could all be varied [28-32] to produce a series of cluster materials. So far a few combinations have been attempted on graphene moiré other than g/Ir(111), including Co, Fe, Ru, Rh, Pd, Pt, and Au on g/Ru(0001) [11, 25, 33-38]; a mixture of Ru and Pt on g/Ru(0001) [30]; Ni on g/Rh(111) [12]; and Au on g/Pt(111) [39]. The desired monodispersity and structural uniformity of the clusters have been elusive. Zhou *et al.* [11] reported that at sub-monolayer coverage, Rh formed dispersed nanoparticles several nanometers in diameter on g/Ru(0001) at room temperature. Deposition of 0.1~0.6 ML

of Pd, Co, or Au atoms resulted in the formation of a few very large particles [11, 25]. Rh, Pd, Co, and Au failed to occupy most of the moiré cells with individual clusters. At ca. 0.15 ML, Engstfeld *et al.* [30] reported that the filling factor topped at ca. 50% for Ru and 30% for Pt when deposited on g/Ru(0001) at ca. 300 K. A filling factor of nearly 100% on g/Ru(0001), however, was achieved by Donner *et al.* for Pt at 140~180 K [35] and by Engstfeld *et al.* at 230-250 K for Ru [30]. The experimental results on g/Ru(0001) so far are summarized in Table 3.1.

Table 3.1: Summary of experimental conditions and results in previous studies of self-assembled metal clusters formed on graphene moiré/Ru(0001).

Reference	Metal deposited	Deposition temperature	Deposition rate	Coverage deposited	Maximum filling factor achieved
Pan *et al.* [a]	Pt	RT	0.01 ML/min	0.02-0.36 ML	10-40% *
Donner *et al.* [b]	Pt	140-180 K	0.03 ML/min	0.06-0.24 ML	53-100%
Zhou *et al.* [c]	Co, Pd, Au	RT	0.1 ML/min	0.1-0.6 ML	very low *
	Rh			0.05-0.80 ML	15% *
Sutter *et al.* [d]	Ru	200 K	n/a	0.30 ML	30% *
Engstfeld *et al.* [e]	Ru	309 K	n/a	$\leq$ 0.15 ML	50%
		230-250 K			100%
	Pt	305 K			30%

RT = room temperature. n/a = no information given. * = estimated based on published STM images. Filling factor is as the percentage of moiré cells filled by individual clusters.

[a] Ref. [34]

[b] Ref. [35]

[c] Ref. [11]

[d] Ref. [36]

[e] Ref. [30]

To begin to quantify the diffusion of small metal species on g/Ru(0001), we have performed an extensive DFT-based study of the diffusion of the Rh and Au adatoms on the full (12×12)-graphene moiré-(11×11)-Ru(0001) surface [40]. The results were presented in Chapter 2. We demonstrated that the global diffusion barrier of the adatoms (for traversing between the fcc regions of neighboring moiré cells) can be efficiently estimated by studying the local adsorption and diffusion characteristics in the different regions of the graphene moiré, represented by small graphene/Ru(0001) surface models that reflect the different positions of the graphene lattice relative to the Ru surface in each region (Figure 2.2). This insight allowed us to estimate the global diffusion barrier for Rh_1 and Au_1 to be 0.56 and 0.81 eV respectively, in close agreement with the global diffusion barriers determined using the PESs of the full moiré surface (0.53 eV for Rh_1 and 0.71 eV for Au_1). In this Chapter, we use the small surface models to study the adsorption and diffusion of the adatoms of all 18 4d and 5d transition metals (Y, Zr, Nb, Mo, Tc, Ru, Rh, Pd, Ag, La, Hf, Ta, W, Re, Os, Ir, Pt, and Au) on g/Ru(0001). We show that the fcc region is the globally preferred adsorption site for all of these metals, and that the earlier 4d and 5d metal adatoms tend to have stronger adsorption energies and moreover, higher global diffusion barriers. The findings are discussed in the context of available experimental observations to shed light on the fundamental factors that affect the nucleation behavior of different metals on g/Ru(0001).

3.2 Methods

Periodic DFT calculations were performed using the Vienna *Ab Initio* Simulation Package [41-43] in the generalized gradient approximation (GGA-PBE) [44]. The core electrons were described by the projector augmented wave method [45], while the Kohn-

Sham valence states (Y(4s4p4d5s); Zr(4p4d5s); Nb(4p4d5s); Mo(4p4d5s); Tc(4p4d5s); Ru(4d5s); Rh(4d5s); Pd(4d5s); Ag(4d5s); La(4p5s5d6s); Hf(5d6s); Ta(5d6s); W(5d6s); Re(5p5d6s); Os(5d6s); Ir(5d6s); Pt(5d6s); Au(5d6s)) were expanded in plane wave basis sets up to 400 eV. Electronic energy was converged to 10^{-5} eV. A first-order Methfessel-Paxton scheme [46] was used to smear the electronic states with a width of 0.1 eV. The optimized Ru lattice constant a = 2.726 Å and c = 4.302 Å and graphene lattice constant a = 2.460 Å are in good agreement with the experimental values (a = 2.706 Å and c = 4.28 Å; a = 2.46 Å) and the previous computational results [47-50]. A vacuum space of ~13 Å was used to separate neighboring images in the z direction. Our previous study suggested that spin polarization was not important [40], so it was not included in these calculations.

Freestanding graphene and Ru(0001)-supported graphene with (3×3) surface unit cells (Figure 2.2) were used in this study to represent several different high-symmetry C_6 rings in the graphene moiré supercell on Ru(0001) (highlighted in Figure 2.1a). The freestanding graphene unit cell (consisting of 18 C atoms; Figure 2.2a) was at the equilibrium lattice constant of 2.460 Å (corresponding to a C-C bond length of 1.420 Å). The Ru(0001)-supported graphene consisted of a single layer of flat graphene laid on top of a three-layer Ru(0001) slab (for a total of 18 C and 27 Ru atoms in the unit cell), where the graphene in-plane lattice was stretched by 10.8% from 2.460 Å to 2.726 Å (corresponding to a C-C bond length of 1.574 Å) to match the lattice size of the Ru(0001) surface. The fcc version exposed the fcc sites on the Ru(0001) surface through the C_6 rings (Figure 2.2b), while the hcp version exposed the hcp sites on the Ru(0001) surface through the C_6 rings (Figure 2.2c). In the ridge version (Figure 2.2d) the C atoms were

offset along the direction of the C-C bond by 0.787 Å, i.e., half of the C-C bond length of 1.574 Å. After fully relaxing the C and top-layer Ru atoms to below 0.03 eV/Å, the graphene layer was located at 2.100, 2.120, and 2.093 Å above the bulk-truncated position of the initial un-relaxed Ru(0001) surface in the fcc, hcp, and ridge versions, respectively. The minimum Ru-graphene separation in the full graphene moiré/Ru(0001) unit cell was calculated to be 2.156Å [40]. The experimentally measured Ru-graphene separation ranged from 1.5-2.2Å [36]. A Γ-centered 5×5×1 Monkhorst-Pack *k*-point grid was used to sample the reciprocal space of the unit cells of both the freestanding and the Ru(0001)-supported graphene.

The adsorption of the adatoms was studied on the graphene side of the slabs only, with the electrostatic potential adjusted accordingly [51]. The adatom, the graphene, and the top layer of Ru were relaxed in the *z* direction only. Geometry optimization was converged to when the forces on all relaxed atoms fell below 0.05 eV/Å in all degrees of freedom. The adsorption energy of an adatom on a surface was calculated as $\Delta E = E_{total} - E_{surface} - E_{adatom}$, where E_{total} and $E_{surface}$ are the total energies of the surface with and without the adatom, respectively, and E_{adatom} is the total energy of the isolated metal atom in the gas phase, calculated in a cubic cell 26 Å on each side. A more negative ΔE indicates stronger adsorption.

3.3 Results and Discussion

3.3.1 Fcc and hcp g/Ru(0001) surfaces

On the (3×3) fcc and the hcp g/Ru(0001) surfaces there are four high-symmetry sites in the C_6 ring: two C top sites, the bridge site in the middle of each C-C bond, and the ring center site (Figures 2.2b and 2.2c). The two C top sites are differentiated by

whether there is a Ru atom beneath; the t1 C is located above a 1st layer Ru atom, whereas the t2 C is located above a surface hollow site. To generate the PES of each adatom on the two surfaces, we calculated the adsorption energy of each adatom at two positions that trisect each of the three lines that connect the ring center site and the t1, t2, and bridge sites in addition to the high-symmetry sites, for a total of 10 calculations describing 1/6 of the C_6 ring (the highlighted triangular section in Figures 2.2b and 2.2c), or for a total sampling density of 49 points per C_6 ring. For each calculation, the adatom is fixed in the *x* and *y* direction and only allowed to relax in the *z* direction. The PESs for Y, Rh, Pt, and Au on the fcc g/Ru(0001) surface are shown Figure 3.2 as examples for early, mid, and late transition metals. The PESs for the other metals, as well as the corresponding PESs on the hcp g/Ru(0001) surface, are found in Appendix B. The minimum adsorption energy and the corresponding adsorption site on the fcc and the hcp surfaces are listed in Table 3.2 for the 18 adatoms. Our previous study [40] found that the (3×3) g/Ru(0001) surfaces provide close approximations of the minimum adsorption energies of the adatoms as calculated on the full graphene moiré/Ru(0001) surface (e.g. in the fcc region, (3×3) vs. full moiré: Rh: –2.65 vs. –2.40 eV; Au: –1.42 vs. –1.57 eV).

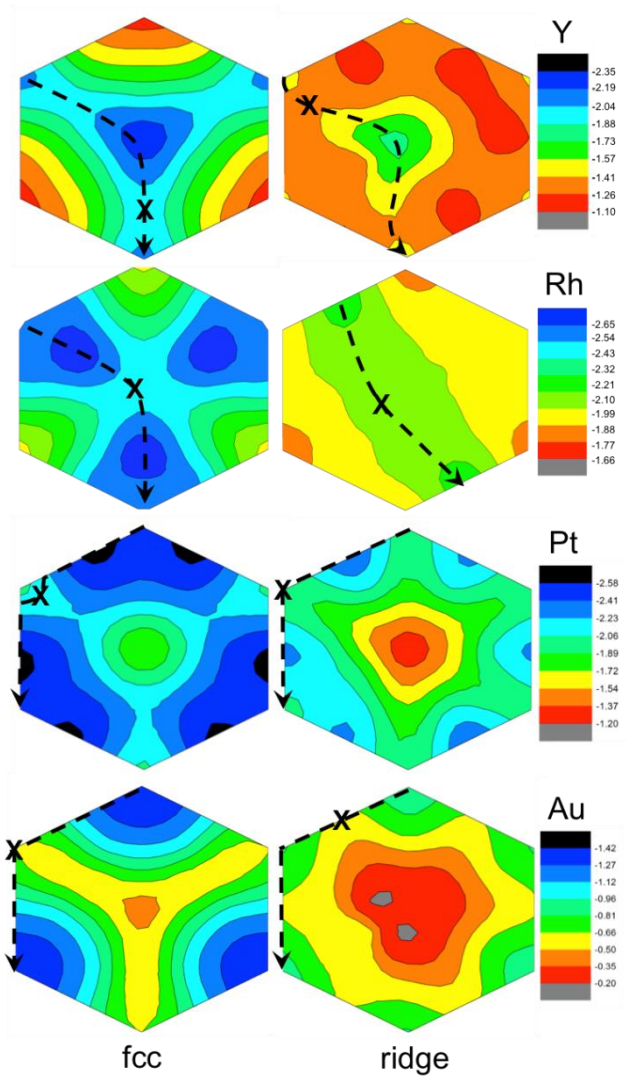

Figure 3.2: Potential energy surfaces of the Y, Rh, Pt, and Au adatom on the (3×3) fcc (left) and ridge (right) g/Ru(0001) surfaces. Adsorption energy is in eV. One C_6 ring is shown for brevity. Contours are generated based on interpolation as an aid to the eye. The minimum-energy diffusion path between adjacent local minima is indicated on each surface by a dashed line. One transition state on each path is marked by "X".

For all the adatoms in this study, adsorption is stronger in the fcc region than in the hcp region. This is consistent with the observation that clusters nucleate preferentially in the fcc region of graphene moiré/Ru(0001) for all the metals investigated

experimentally so far. Nucleation outside the fcc region is seen experimentally only when the surface temperature is very low [27, 35]. When the minimum adsorption energy for each adatom (ΔE_{fcc}) is plotted against the atomic number of the metal (Figure 3.3), the curves exhibit a double valley behavior for both the 4d and the 5d metals, with the peaks (weaker adsorption) corresponding to metals with a half-filled or completely filled d shell (i.e. $4d^5 5s^1$ for Mo and $5d^5 6s^2$ for Re; $4d^{10} 5s^1$ for Ag and $5d^{10} 6s^1$ for Au). It is commonly accepted that a half-filled or completely filled d-shell is more stable than other configurations. To the extent that the metal adatom-surface interaction primarily involves the d states from the metals, a more stable d-shell should result in less stable adsorption of the metal adatom.

The 4d and 5d metals exhibit similar adsorption site preference. As can be seen in Table 3.2, the preferred adsorption site is the ring center for the early transition metals, and shifts to the bridge site and finally the top site going from the left to the right of the periodic table. In addition, the metals with half-filled and completely filled d-shells (Mo, Ag, and Au) prefer less-coordinated sites than the neighboring metals on the periodic table. Both suggest that the d-shell characteristics of the metal atom play a key role in the site preference.

Table 3.2: Minimum-energy adsorption site, associated adsorption energy (ΔE, in eV), and activation barrier for diffusion (E_a, in eV) on freestanding graphene and graphene/Ru(0001).

adatom	freestanding graphene			graphene/Ru(0001)				
metal	Site	ΔE	E_a	site	ΔE_{fcc}	ΔE_{hcp}	$E_{a,fcc}$	$E_{a,moiré}$
Y	center	-1.49	0.37	center	-2.31	-2.15	0.34	0.88
Zr	center	-2.09	0.64	center	-3.01	-2.79	0.49	1.20
Nb	center	-1.59	0.55	center	-2.58	-2.21	0.38	1.15
Mo	bridge	-0.17	0.01	t1	-1.17	-0.83	0.07	0.80
Tc	center	-1.00	0.57	center	-1.86	-1.53	0.30	0.83
Ru	center	-1.59	0.65	t1	-2.40	-2.00	0.22	0.87
Rh	center	-1.54	0.17	t1	-2.56	-2.27	0.25	0.56
Pd	bridge	-1.07	0.04	bridge	-1.43	-1.35	0.18	0.24
Ag	Top	-0.03	0.00	t2	-0.57	-0.36	0.49	0.53
La	center	-1.97	0.29	center	-2.59	-2.42	0.36	1.00
Hf	center	-1.56	0.39	center	-3.17	-2.87	0.57	1.38
Ta	center	-1.72	0.82	center	-3.34	-2.95	0.82	1.73
W	bridge	-0.49	0.03	t1	-2.17	-1.83	0.23	1.07
Re	top	-0.04	0.00	t1	-1.49	-1.11	0.20	0.96
Os	center	-0.99	0.58	t1	-2.38	-1.96	0.44	0.99
Ir	bridge	-1.21	0.09	t1	-2.62	-2.20	0.52	0.86
Pt	bridge	-1.51	0.17	bridge	-2.59	-2.31	0.39	0.75
Au	top	-0.10	0.00	t2	-1.41	-1.13	0.76	0.81

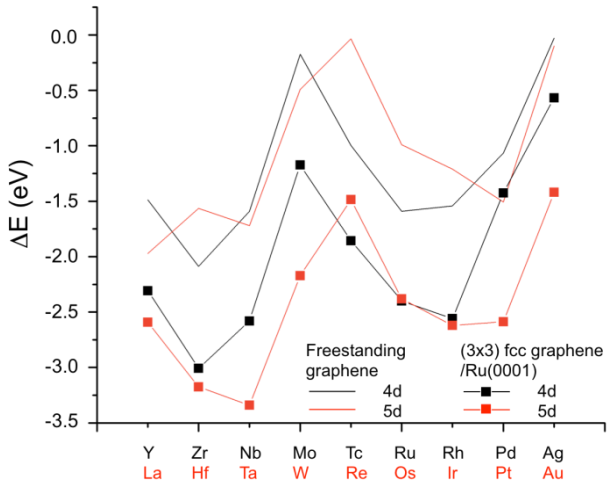

Figure 3.3: Minimum adsorption energies (ΔE) of the 18 4d and 5d transition metal adatoms on the freestanding graphene and (3×3) fcc graphene/Ru(0001) surfaces, plotted as a function of the atomic number. Lines are guides to the eye. See Table 3.2 for the minimum-energy adsorption site for each metal adatom.

Next, we examined the PESs of the adatoms to assess the local diffusion properties of each adatom, here taking the fcc region as an example. Each PES plot reveals the contours of the local potential energy surface for an adatom, thereby allowing us to visually identify the minimum-energy diffusion path for the adatom to diffuse from the minimum-energy adsorption site across the C_6 ring, and to estimate the diffusion activation barrier ($E_{a,fcc}$) associated with the path, defined to be the difference between the maximum and minimum energies on the path, without having to perform transition state calculations.

The early-to-mid transition metals (e.g. Y and Rh, Figure 3.2) prefer to adsorb in the ring center site and t1 site, and their minimum-energy diffusion paths traverse the C_6 ring between the ring center site and t1 site while avoiding the t2 site. The late transition metals (e.g. Pt and Au, Figure 3.2) are the least stable in the ring center site, so their

minimum-energy diffusion paths avoid the ring center site and run along the C-C bonds instead. The $E_{a,fcc}$ for the 18 adatoms thus estimated are listed in Table 3.2. The $E_{a,fcc}$ for the 4d metals are on average smaller than those for the 5d metals. Our results in Chapter 2 verified the local diffusion barrier for Rh_1 and Au_1 using the climbing-image nudged elastic band method [52] to be 0.22 and 0.76 eV, respectively, with which the estimated values based on the PESs (0.25 and 0.76 eV) are in close agreement [40]. Recent DFT calculations by Wang *et al.* found the diffusion barrier for Pd_1 on g/Ru(0001) to be ≤ 0.2 eV, and that the barrier roughly scales with 0.2 eV per contacting Pd atom for larger Pd clusters [38]. This agrees with our estimated value of diffusion barrier (0.24 eV) for Pd_1 on g/Ru(0001). By assuming that the local hopping of adatoms follows an Arrhenius rate of $r = A \cdot \exp(-E_a/kT)$ with a standard pre-exponential factor of $A = 10^{13}$ s^{-1} [53], we calculate all of the adatoms to have hopping rates significantly greater than 1 s^{-1} on the fcc g/Ru(0001) surface at room temperature, with the exception of Ta and Au. Thus nearly all of the metal adatoms can diffuse rapidly at room temperature in the fcc region of g/Ru(0001).

3.3.2 Freestanding graphene

To gain an idea of how the Ru(0001) substrate affects the adsorption of adatoms on graphene compared to freestanding graphene, we calculated the PESs of all 18 adatoms on freestanding graphene. The freestanding graphene also approximately represents the mound region of the graphene moiré [40] due to the graphene being effectively decoupled from the Ru substrate in this region [47, 48, 54]. Besides the high-symmetry top, bridge, and ring center sites, the adsorption of each adatom is calculated at two additional positions between each pair of the high-symmetry sites, for a total

sampling density of 61 points per C_6 ring. The minimum adsorption energies (ΔE) for all 18 adatoms on the freestanding graphene are also plotted in Figure 3.3, and are listed with the preferred adsorption sites in Table 3.2. Our results agree closely with previously reported DFT adsorption energies for several metal adatoms on freestanding graphene [49, 50, 55-58]. Like on g/Ru(0001), ΔE on the freestanding graphene exhibits a double valley behavior with peaks corresponding to metals with a half-filled or completely filled d shell (Mo, Re, Ag, and Au). The near-zero adsorption energies for the four metal adatoms also suggest that the metal s-carbon sp interaction is weak. A similar double valley behavior has been reported for 3d metal adatoms adsorbed on freestanding graphene, with the weakest adsorption energy occurring for Mn and Cu [55, 59]. The early transition metal adatoms preferentially adsorb in the ring center site, and the trend is for the preferred adsorption site to shift to the bridge site and finally to the top site going from the left to the right of the periodic table. As on the fcc g/Ru(0001) surface, Mo, Ag, Re, and Au prefer less-coordinated sites than the neighboring metals on the periodic table.

As Figure 3.3 shows, the adsorption of the adatoms on the freestanding graphene is consistently weaker than on the fcc g/Ru(0001) surface. The differences are over 1 eV for some metals. This is consistent with the fact that the original graphite basal plane (including graphene) is well known to be chemically inert. When graphene is supported on the Ru(0001) surface, the interaction between the two surfaces partially disrupts the π-bonding network in the graphene, causing some regions in the graphene to sp^3-rehybridize, as mentioned in Chapter 2, which enables through-carbon metal-metal

bonding [25, 54] that substantially enhances the adsorption of even the Mo, Re, Ag, and Au adatoms, which have half-filled or completely filled d shells.

Figure 3.4 shows the PESs for the Y, Rh, Pt, and Au adatoms as examples. The PESs for the remaining adatoms are found in the Appendix B. For the adatoms that preferentially adsorb in the ring center site, the minimum-energy diffusion paths begin at the ring center and cross the C-C bond. For the later transition metals that preferentially adsorb in the bridge or the top site, the minimum-energy diffusion paths run along the C-C bond and avoid the ring center. This pattern is the same as on the fcc g/Ru(0001) surface as discussed above. Overall, not every adatom has a lower diffusion activation energy on the freestanding graphene than on the fcc g/Ru(0001) surface, but all except Ta have a hopping rate that is greater than 1 s^{-1} at room temperature.

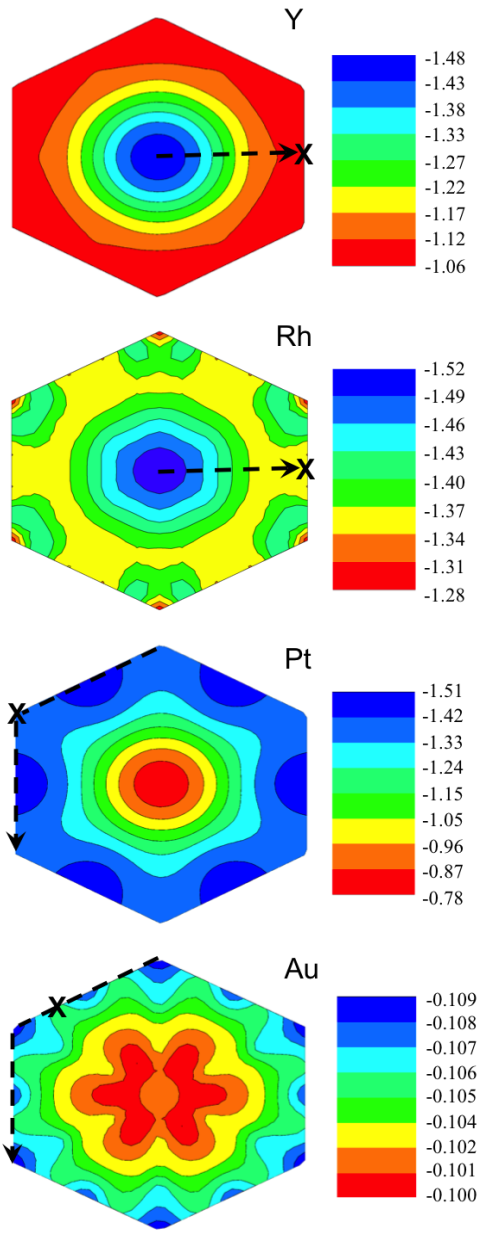

Figure 3.4: Potential energy surfaces of the Y, Rh, Pt, and Au adatoms on freestanding graphene. Adsorption energy is in eV. One C_6 ring is shown for brevity. Contours are generated based on interpolation as an aid to the eye. The minimum-energy diffusion path between adjacent local minima is indicated on each surface by a dashed line. One transition state on each path is marked by "X".

3.3.3 Diffusion between moiré cells

An additional (3×3) surface model was used to represent the ridge region between the fcc and hcp regions on the moiré where the C and the Ru atoms are misaligned. This surface has a lower, two-fold symmetry (highlighted in Figure 2.2d), vs. the six-fold symmetry of the fcc and hcp regions. There are five high symmetry sites, including two top sites, two bridge sites, and a ring center site (Figure 2.2d). To construct the PESs on the ridge surface two additional calculations are performed between each of the top and bridge sites with the ring center site, resulting in a total sampling density of 38 sites per C_6 ring. Figure 3.2 shows the PESs of the Y, Rh, Pt, and Au adatoms on the ridge surface. Those of the other metals are included in the Appendix B.

Our previous study [40] found that the (3×3) ridge and fcc g/Ru(0001) surfaces can be used together to generate good estimates for the global diffusion barriers for metal adatoms. For instance, the energetic difference between the minimum-energy diffusion transition state identified on the (3×3) ridge surface and the minimum-energy adsorption site on the (3×3) fcc surface are 0.56 eV for Rh_1 and 0.81 eV for Au_1, in close agreement with the global diffusion barriers ($E_{a,moiré}$) determined using the coarse-grained PESs on the full graphene moiré (0.53 and 0.71 eV, respectively) [40]. We can take advantage of this approach and explore the diffusion rates of the 18 4d and 5d transition metal adatoms on the graphene moiré on Ru(0001) at less computational cost than would be required to tackle the full moiré surface for each adatom. The $E_{a,moiré}$ thus estimated are listed in Table 3.2, and the corresponding global hopping rates at room temperature are plotted in Figure 3.5 based on the assumptions of Arrhenius rate and a pre-exponential factor of 10^{12} s^{-1}, i.e., 1/10 of the pre-exponential factor for local diffusion [60]. The values of

$E_{a,moiré}$ are generally higher than that of $E_{a,fcc}$, indicating that the corrugation of the moiré plays a dominant role in limiting the facility with which metal adatoms diffuse on the graphene surface. The earlier transition metal adatoms tend to have lower global hopping rates, and the 4d metal adatom generally has a higher diffusion rate than the 5d metal adatom in the same group in the periodic table.

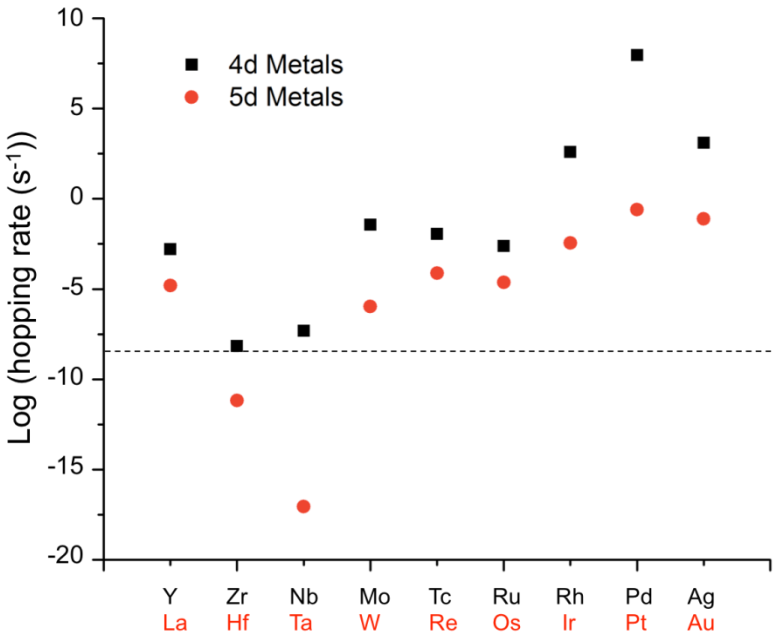

Figure 3.5: Global hopping rates (s^{-1}) of the 18 4d and 5d transition metal adatoms on g/Ru(0001) at 298 K, plotted as a function of atomic number of the metal. The horizontal dashed line indicates 10^{-8} s^{-1}; see text for detail.

Before further discussion we briefly comment on the generally accepted rule of thumb that the surface diffusion barrier of an adatom is 10~20% of its adsorption energy

[53]. To assess its applicability to the global diffusion of the metal adatoms on g/Ru(0001), $E_{a,moiré}$ is plotted against ΔE_{fcc} for the 4d and 5d metals in Figure 3.6. There is considerable scatter in the plot. A rough linear trend with a slope of 0.21 and $R^2 = 0.56$ can be obtained if Ta, Rh, and Pd are excluded as outliers. Individual examples counter to the rule can be found, e.g., the Rh and Au adatoms, for which the adsorption energy is stronger for the former and the global diffusion barrier is higher for the latter [40]. Thus the rule can break down for diffusion traversing multiple chemically heterogeneous domains on a given surface, as is true for graphene moiré on Ru(0001). As noted by Nilekar *et al.*, this rule offers a convenient way to estimate diffusion barriers but does not reflect any fundamental physical principle [61].

As has been pointed out, substrate temperature is an important factor in template-controlled cluster formation [62]. We illustrate the effects of the factors that can influence the outcome of cluster nucleation on graphene moiré in Figure 3.7. Based on Figure 3.6 we assume here for simplicity that there is a linear relation between the global diffusion barrier and the adsorption energy of the metal adatoms. A strong adsorption energy would increase the probability that a metal adatom nucleates a metal cluster, but decrease the diffusion length of the adatom so that it visits fewer moiré cells, which could result in nucleation outside fcc regions and uneven cluster sizes. A weak adsorption energy would increase the diffusion length and allow better sampling of the surface, but reduce the probability for an adatom to nucleate a cluster, leading to fewer and larger clusters. An intermediate adsorption energy (ΔE_0) should exist where the filling factor is maximized as nucleation density is balanced by diffusion length.

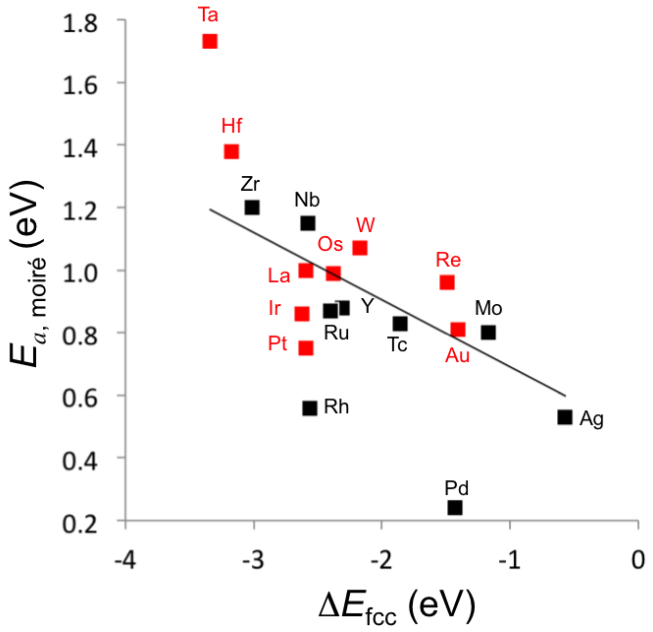

Figure 3.6: Global diffusion barriers ($E_{a,moiré}$) plotted against the global minimum adsorption energy (ΔE_{fcc}, as found on the fcc surface) for the 18 4d and 5d transition metal adatoms on g/Ru(0001). The line is the result of linear regression as described in the text.

ΔE_0 is influenced by both the substrate temperature (T) and by the coverage of the metal atoms deposited (θ). A change in either of the two would shift both of the lines in Figure 3.7 and therefore shift the location of the maximum filling on the ΔE axis: Higher temperature would decrease the nucleation probability and increase the diffusion length, thereby shift ΔE_0 to stronger-adsorbing metals ($\Delta E_0'$ in Figure 3.7) whereas higher coverage would increase the nucleation probability and decrease the diffusion length, thereby shift ΔE_0 to weaker-adsorbing metals ($\Delta E_0''$ in Figure 3.7). It should be noted that we are focusing on the nucleation phase of the cluster formation on g/Ru(0001), which occurs within a fraction of a monolayer equivalent for the deposited metal. The

nucleation density, diffusion length, and coverage could also be compared on the corresponding rates basis: The rate of deposition should have the same effect on the rate of nucleation and diffusion velocity as coverage does on nucleation density and diffusion length.

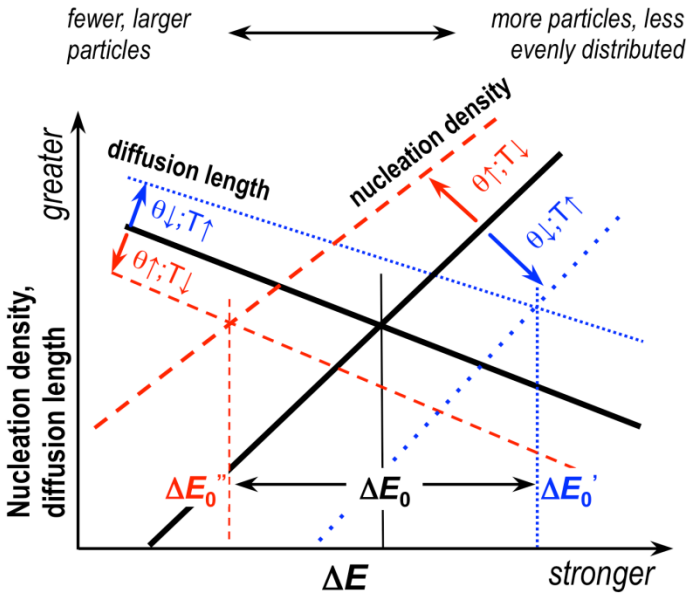

Figure 3.7: Schematic illustrating the effects of substrate temperature (T) and deposition coverage (θ) on the ability of transition metals with different adatom adsorption energies (ΔE) to achieve high filling of moiré cells with clusters of even size distribution. The intermediate adsorption energy that corresponds to the highest filling factor at given conditions, ΔE_0, is shown as a balance between the diffusion length and nucleation density, both of which are functions of T and θ. A change in T and θ therefore causes ΔE_0 to shift to a new value ($\Delta E_0'$ or $\Delta E_0''$). See text for discussion.

As mentioned at the beginning, a filling factor of nearly 100% on g/Ru(0001) was achieved for Pt at 140~180 K [35] and at 230-250 K for Ru [30], while 200 K was evidently too low a temperature for Ru [36]. Using the Arrhenius rate equation, it can be roughly estimated that the global hopping rate that allows both metals to achieve 100%

filling is 10^{-8}~10^{-9} s^{-1} (somewhat lower for Pt_1 and higher for Ru_1), using $E_{a,moiré} = 0.75$ for Pt_1 and 0.87 eV for Ru_1 (Table 3.2) and a pre-exponential factor of 10^{12} s^{-1}. The dashed line in Figure 3.5 marks 10^{-8} s^{-1}. If this is taken to be the global hopping rate that maximizes the filling factor at room temperature, then Figure 3.5 suggests that ΔE_0 occurs at Zr and Hf at room temperature. None of the 4d and 5d transition metals tested experimentally so far has exceeded 50% filling when deposited on g/Ru(0001) at room temperature (see Table 3.1; although it is unclear if any metal can achieve 100% filling at room temperature). When the temperature is lowered, ΔE_0 shifts to Ru and then to Pt [30, 35]. N'Diaye *et al.* showed that the filling factor can be increased for Au and Re on g/Ir(111) if the substrate temperature is lowered to 90 and 200 K respectively [27]. Liu and co-workers showed that high deposition coverage of Au resulted in the nucleation of more Au particles on g/Ru(0001) [33].

Several caveats to the discussion above need to be noted. The adatom adsorption energy is only a proxy for adatom mobility. Figure 3.6 shows that the correlation between the global diffusion barriers and minimum energy adsorption energies of the adatoms is considerably scattered, and the global diffusion barriers themselves are based on estimates. Second, adatoms may not be the main contribution to diffusion. Our results in Chapter 4 indicate that the Au dimer has higher mobility on g/Ru(0001) than the Au adatom because Au_2 favors the upright configuration [60]. A further issue is that the disparity between the affinities of the early transition metals for graphene and for Ru may lead to the facile penetration and intercalation of the deposited metal below the graphene, as has been demonstrated for Ce on g/Ru(0001) for instance [29]. Nonetheless, Figure 3.7 suggests a simple way to conceptualize and predict the effects of the key

factors controlling cluster nucleation on graphene moiré that is qualitatively consistent with existing experimental results and may be exploited by experimental researchers who wish to test the deposition of additional metals on g/Ru(0001).

3.4 Conclusions

Long-range moiré superstructures develop in graphene formed on a number of single crystal surfaces, which can function as templates to drive the self-assembly of superlattices of metal clusters for model catalyst studies. To shed light on, and make predictions for, the nucleation behavior of different metals deposited on the graphene moiré/Ru(0001) surface, we have performed periodic density function theory calculations using a series of (3×3) surface models representing the fcc, hcp, mound, and ridge regions of the graphene moiré to investigate the adsorption and diffusion characteristics, and to estimate the global diffusion barriers, for all 18 4d (Y-Ag) and 5d (La-Au) metal adatoms on g/Ru(0001).

For all the adatoms, the global minimum-energy adsorption site is found in the fcc region and the global maximum in the mound region, consistent with the previous experimental observations that nucleation almost exclusively occurred in the fcc region and never in the mound region [11, 30, 34-36]. For each series of the transition metals, those that have a half-filled or completely filled d shell have the weaker adsorption energies. By comparing the g/Ru(0001) surfaces with the freestanding graphene, it is clearly seen that the Ru substrate enhances the adsorption of all 18 adatoms on graphene.

Diffusion within the fcc region is facile at room temperature for most adatoms (with the notable exception of Ta), but an additional barrier is imposed by the corrugation of the graphene moiré for traversing between moiré cells. Ta is an outlier due to its

considerably strong adsorption on g/Ru(0001), which is partly attributed to the strong interaction between Ta and Ru. Overall, the adatoms of the earlier transition metals have lower global mobility than those of the later ones, and the adatom of a 5d transition metal has lower global mobility than that of the corresponding 4d transition metal in the same group in the periodic table. We postulate that the maximum filling factor of the graphene moiré cells is achieved as a balance between nucleation density and diffusion length, both of which can be connected to the global mobility of the metal adatom (if it dominates surface diffusion), which is in turn connected to the adsorption energy of the adatom of g/Ru(0001). Substrate temperature and coverage of metal atoms deposited are expected to influence nucleation density and diffusion length in opposite ways, thereby shifting the intermediate adsorption energy where the filling factor is maximized to different metals. The expected effects are consistent with available experimental results, suggesting that these insights may help experimental researchers achieve dense super-lattices of clusters of additional transition metals on g/Ru(0001), for applications including model catalysis studies.

3.5 References

[1] J. Wintterlin, M.L. Bocquet, Surf. Sci., 603 (2009) 1841-1852.

[2] D. Eom, D. Prezzi, K.T. Rim, H. Zhou, M. Lefenfeld, S. Xiao, C. Nuckolls, M.S. Hybertsen, T.F. Heinz, G.W. Flynn, Nano Lett., 9 (2009) 2844-2848.

[3] Y. Gamo, A. Nagashima, M. Wakabayashi, M. Terai, C. Oshima, Surf. Sci., 374 (1997) 61-64.

[4] M. Weser, Y. Rehder, K. Horn, M. Sicot, M. Fonin, A.B. Preobrajenski, E.N. Voloshina, E. Goering, Y.S. Dedkov, Appl. Phys. Lett., 96 (2010) 012504.

[5] M.-C. Wu, Q. Xu, D.W. Goodman, J. Phys. Chem., 98 (1994) 5104-5110.

[6] S. Marchini, S. Gunther, J. Wintterlin, Phys. Rev. B, 76 (2007) 075429.

[7] Y. Pan, D.X. Shi, H.J. Gao, Chinese Phys., 16 (2007) 3151-3153.

[8] D. Martoccia, P.R. Willmott, T. Brugger, M. Bjorck, S. Gunther, C.M. Schleputz, A. Cervellino, S.A. Pauli, B.D. Patterson, S. Marchini, J. Wintterlin, W. Moritz, T. Greber, Phys. Rev. Lett., 101 (2008) 126102.

[9] W. Moritz, B. Wang, M.L. Bocquet, T. Brugger, T. Greber, J. Wintterlin, S. Gunther, Phys. Rev. Lett., 104 (2010) 136102.

[10] H. Zhang, Q. Fu, Y. Cui, D.L. Tan, X.H. Bao, J. Phys. Chem. C, 113 (2009) 8296-8301.

[11] Z. Zhou, F. Gao, D.W. Goodman, Surf. Sci., 604 (2010) L31-L38.

[12] M. Sicot, S. Bouvron, O. Zander, U. Rudiger, Y.S. Dedkov, M. Fonin, Appl. Phys. Lett., 96 (2010) 093115.

[13] J. Coraux, A.T. N'Diaye, C. Busse, T. Michely, Nano Lett., 8 (2008) 565-570.

[14] J. Coraux, A.T. N'Diaye, M. Engler, C. Busse, D. Wall, N. Buckanie, F. Heringdorf, R. van Gastei, B. Poelsema, T. Michely, New J. Phys., 11 (2009) 023006.

[15] A.T. N'Diaye, J. Coraux, T.N. Plasa, C. Busse, T. Michely, New J. Phys., 10 (2008) 043033.

[16] S.-Y. Kwon, C.V. Ciobanu, V. Petrova, V.B. Shenoy, J. Bareño, V. Gambin, I. Petrov, S. Kodambaka, Nano Lett., 9 (2009) 3985-3990.

[17] J.H. Gao, N. Ishida, I. Scott, D. Fujita, Carbon, 50 (2012) 1674-1680.

[18] X. Chen, S. Liu, L. Liu, X. Liu, X. Liu, L. Wang, Appl. Phys. Lett., 100 (2012) 163106-163103.

[19] W. Kim, K. Yoo, E.K. Seo, S.J. Kim, C. Hwang, J. Korean Phys. Soc., 59 (2011) 71-74.

[20] T.A. Land, T. Michely, R.J. Behm, J.C. Hemminger, G. Comsa, Surf. Sci., 264 (1992) 261-270.

[21] P.W. Sutter, J.I. Flege, E.A. Sutter, Nat. Mater., 7 (2008) 406-411.

[22] B. Borca, F. Calleja, J.J. Hinarejos, A.L.V. de Parga, R. Miranda, J. Phys.-Condens. Matter, 21 (2009) 134002.

[23] A.L. Vázquez de Parga, F. Calleja, B. Borca, M.C.G. Passeggi, J.J. Hinarejos, F. Guinea, R. Miranda, Phys. Rev. Lett., 100 (2008) 056807.

[24] K. Katsiev, Y. Losovyj, Z. Zhou, E. Vescovo, L. Liu, P.A. Dowben, D.W. Goodman, Phys. Rev. B, 85 (2012) 195405.

[25] Y. Xu, L. Semidey-Flecha, L. Liu, Z. Zhou, D.W. Goodman, Faraday Discuss., 152 (2011) 267-276.

[26] A.T. N'Diaye, S. Bleikamp, P.J. Feibelman, T. Michely, Phys. Rev. Lett., 97 (2006) 215501.

[27] A.T. N'Diaye, T. Gerber, C. Busse, J. Myslivecek, J. Coraux, T. Michely, New J. Phys., 11 (2009) 103045.

[28] Z. Zhou, B.F. Habenicht, Q. Guo, Z. Yan, Y. Xu, L. Liu, D.W. Goodman, Surf. Sci., 611 (2013) 67-73.

[29] L. Huang, Y. Pan, L. Pan, M. Gao, W. Xu, Y. Que, H. Zhou, Y. Wang, S. Du, H.J. Gao, Appl. Phys. Lett., 99 (2011) 163107-163103.

[30] A.K. Engstfeld, S. Beckord, C.D. Lorenz, R.J. Behm, ChemPhysChem, 13 (2012) 3313-3319.

[31] R. Addou, A. Dahal, M. Batzill, Surf. Sci., 606 (2012) 1108-1112.

[32] A.B. Preobrajenski, M.L. Ng, A.S. Vinogradov, N. Martensson, Phys. Rev. B, 78 (2008) 073401.

[33] L. Liu, Z. Zhou, Q. Guo, Z. Yan, Y. Yao, D.W. Goodman, Surf. Sci., 605 (2011) L47-L50.

[34] Y. Pan, M. Gao, L. Huang, F. Liu, H.J. Gao, Appl. Phys. Lett., 95 (2009) 093106.

[35] K. Donner, P. Jakob, J. Chem. Phys., 131 (2009) 164701.

[36] E. Sutter, P. Albrecht, B. Wang, M.L. Bocquet, L.J. Wu, Y.M. Zhu, P. Sutter, Surf. Sci., 605 (2011) 1676-1684.

[37] M. Gyamfi, T. Eelbo, M. Waśniowska, R. Wiesendanger, Phys. Rev. B, 84 (2011) 113403.

[38] B. Wang, B. Yoon, M. König, Y. Fukamori, F. Esch, U. Heiz, U. Landman, Nano Lett., 12 (2012) 5907-5912.

[39] D.E. Starr, E.M. Pazhetnov, A.I. Stadnichenko, A.I. Boronin, S.K. Shaikhutdinov, Surf. Sci., 600 (2006) 2688-2695.

[40] L. Semidey-Flecha, D. Teng, B.F. Habenicht, D.S. Sholl, Y. Xu, J. Chem. Phys., 138 (2013) 184710.

[41] G. Kresse, J. Furthmuller, Comp. Mater. Sci., 6 (1996) 15-50.

[42] G. Kresse, J. Furthmuller, Phys. Rev. B, 54 (1996) 11169-11186.

[43] G. Kresse, J. Hafner, Phys. Rev. B, 49 (1994) 14251-14269.

[44] J.J. Perdew, K. Burke, M. Ernzerhof, Phys. Rev. Lett., 77 (1996) 3865.

[45] P.E. Blochl, Phys. Rev. B, 50 (1994) 17953-17979.

[46] M. Methfessel, A.T. Paxton, Phys. Rev. B, 40 (1989) 3616-3621.

[47] B. Wang, M.L. Bocquet, S. Marchini, S. Gunther, J. Wintterlin, Phys. Chem. Chem. Phys., 10 (2008) 3530-3534.

[48] D.E. Jiang, M.H. Du, S. Dai, J. Chem. Phys., 130 (2009) 074705.

[49] K.T. Chan, J.B. Neaton, M.L. Cohen, Phys. Rev. B, 77 (2008) 235430.

[50] L.B. Hu, X.R. Hu, X.B. Wu, C.L. Du, Y.C. Dai, J.B. Deng, Phys. B-Condens. Matter, 405 (2010) 3337-3341.

[51] J. Neugebauer, M. Scheffler, Phys. Rev. B, 46 (1992) 16067-16080.

[52] G. Henkelman, B.P. Uberuaga, H. Jonsson, J. Chem. Phys., 113 (2000) 9901-9904.

[53] J.V. Barth, Surf. Sci. Rep., 40 (2000) 75-149.

[54] B. Wang, S. Gunther, J. Wintterlin, M.L. Bocquet, New J. Phys., 12 (2010) 043041.

[55] O.V. Yazyev, A. Pasquarello, Phys. Rev. B, 82 (2010) 045407.

[56] K. Okazaki-Maeda, Y. Morikawa, S. Tanaka, M. Kohyama, Surf. Sci., 604 (2010) 144-154.

[57] R. Varns, P. Strange, J. Phys.-Condens. Matter, 20 (2008) 225005.

[58] X. Liu, C.Z. Wang, M. Hupalo, W.C. Lu, M.C. Tringides, Y.X. Yao, K.M. Ho, Phys. Chem. Chem. Phys., 14 (2012) 9157-9166.

[59] H. Valencia, A. Gil, G. Frapper, J. Phys. Chem. C, 114 (2010) 14141-14153.

[60] D. Teng, D.S. Sholl, Surf. Sci., (2014) (in press).

[61] A.U. Nilekar, J. Greeley, M. Mavrikakis, Angew. Chem. Int. Edit., 45 (2006) 7046-7049.

[62] C. Becker, K. Wandelt, Top. Curr. Chem., 287 (2009) 45-86.

CHAPTER 4

RH AND AU DIMERS AND TRIMERS ON GRAPHENE/RU(0001)

4.1 Introduction

We aim to understand the adsorption and diffusion of small cluster species on graphene moiré as a step towards understanding mechanism of cluster nucleation and growth. We previously studied Rh and Au monomers on graphene/Ru(0001) (denoted as g/Ru(0001)) [1]. Rh and Au were chosen as our focus because of their distinct patterns in forming clusters on g/Ru(0001) [2]. We characterized the adsorption and diffusion of Rh and Au adatoms on the full surface of g/Ru(0001) and in its different regions. A supercell of (12×12) graphene/(11×11) Ru(0001) with a periodicity of ~30 Å was used to perform the computational calculations since this surface unit cell is the one most experimental groups have observed and identified [3-6]. A detailed study of monomer adsorption and diffusion in different regions was achieved by using a smaller (3×3) unit cell representation of each region. We have found that Rh and Au monomers are energetically most stable in the fcc region. Their diffusion between two neighboring fcc regions proceeds through the ridge and hcp regions. The overall diffusion barrier for a monomer to diffuse across the moiré surface in this way was found to be 0.53 eV for Rh and 0.71 eV for Au.

Our previous results for Rh and Au monomers on g/Ru(0001) show that they are both mobile on the moiré surface. Monomer diffusion alone, however, is not sufficient to describe the growth mechanism of clusters of these metals on the surface. Conventional descriptions of cluster diffusion assume that cluster mobility drops rapidly as the cluster

size increases. For example, Voter showed that for Rh clusters on Rh(100), the diffusion constant scales as $n^{-1.76 \pm 0.06}$ for clusters larger than n = 15 atoms [7]. Examples are known, however, where diffusion of sizeable clusters occurs. Wen *et al*. reported that Ag clusters on Ag(100) containing hundreds of atoms have significant mobility [8] and other direct observations of large cluster diffusion on surfaces have also been made [9-11]. Multiple studies [12-21] have shown that small clusters (dimer, trimer, etc.) are mobile on surfaces and their motion should be included in a proper description of cluster nucleation and growth. For example, a recent study by Signor *et al*. on linear Cu trimers on Ag(111) showed that trimers, once formed, have significantly higher mobility than either monomers or dimers [15]. Xu *et al*. pointed out that for Pd diffusion on MgO(100), the tetramer is the fastest diffusing species at room temperature [16, 17]. Studies of small Ag, Au, Pd, Cu and Ca clusters on MgO(100) show that small clusters such as dimers, trimers, and tetramers are mobile on the surface at the operating temperature of molecular beam epitaxy (MBE) experiments and they display a variety of diffusion mechanisms [18, 19].

The discussion above indicates that a description of the mobility of small metal clusters on the g/Ru(0001) surface is necessary before efforts can be made to describe cluster nucleation and growth. In this Chapter, we address the issue of small cluster diffusion on this graphene moiré surface by reporting DFT calculation results of the lowest-energy structures, diffusion energy barriers, and room temperature hopping rates of dimers and trimers for Rh and Au. We also extend our study to other 4d and 5d transition metals to give initial insight into their nucleation behavior on g/Ru(0001).

4.2 Methods

All periodic DFT calculations [22] were performed using the Vienna *Ab Initio* Simulation Package (VASP) [23-26]. A cutoff energy of 400 eV was used with the Perdew-Burke-Ernzerhof (PBE) [27, 28] exchange-correlation functional within the generalized gradient approximation (GGA). First-order Methfessel-Paxton smearing [29] was used with a width of 0.1 eV and the core electrons were described by the projector augmented-wave (PAW) method [30, 31]. The optimized Ru lattice constant, a = 2.726 Å and c = 4.035 Å, and the graphene lattice constant, a = 2.46 Å, are in good agreement with reported experimental and computational values [6, 32-34]. A vacuum space of 12.85 Å was used to separate the Ru slab replicas. The impact of spin polarization was checked for Rh_2 and Au_2 on all surface models. The residual magnetic moments lower the total energy by less than 0.001 eV in every case, indicating that the more numerically efficient calculations that neglect spin polarization are sufficient.

Performing DFT calculations for the full graphene moiré on Ru(0001) is challenging because of the large size of the supercell. Motivated by our earlier work on metal monomers on this surface [1], we used smaller supercells to approximate the graphene moiré in the fcc, hcp, and ridge regions. A (3×3) Ru(0001) supercell was used to study the adsorption and diffusion of dimer and trimer in each of the three distinct regions in detail. Each supercell contains a layer of graphene on top of a three-layer Ru(0001) slab, giving a total of 18 C atoms and 27 Ru atoms. The graphene was stretched by 10.8% from its equilibrium lattice constant to match the lattice constant of Ru surface. This smaller supercell was verified to produce consistent results with calculations on full supercell. The differences in adsorption energy of Rh and Au

monomers in the fcc region between the (3×3) supercell and full (12×12) supercell are less than 5% [1]. As described in Chapter 2, in the (3×3) supercells, the graphene layer was shifted horizontally in different extents with respect to the Ru slab to expose different sites of Ru through the center of 6-carbon rings. No carbon atom was constrained in the fcc and hcp regions because of their 3-fold symmetry. In the ridge region, however, the in-plane coordinates of two adjacent carbon atoms were constrained to keep the graphene in the right position with respect to Ru surface. We also performed calculations with a (3×3) unit cell of freestanding graphene with 18 C atoms at its equilibrium lattice constant. This is a reasonable representation of the atop region of the graphene moiré because the C atoms in the atop region are located at 3.70 Å above the Ru layer and the Ru substrate effect on graphene is negligible [1]. Using freestanding graphene to approximate atop region was supported by the analysis of Wang *et al*. who proposed that the atop regions form an array of electronically disconnected nanographene islands [35]. A 3×3×1 Γ-centered k-point mesh was used to sample reciprocal space for all calculations in the (3×3) supercell.

Ground-state energy calculations were performed with the bottom two layers of Ru slab fixed. All other atoms were allowed to fully relax, except the two carbon atoms in the ridge region as mentioned above. Geometry relaxations were achieved using a combination of conjugate-gradient and quasi-Newton optimization until the forces on all atoms were less than 0.03 eV/Å. The adsorption energy of a dimer on the surface was given by $E_{ads} = E_{dimer+surface} - E_{surface} - E_{dimer(g)}$, where $E_{dimer+surface}$ and $E_{surface}$ are the total energies of the surface with and without the dimer, and $E_{dimer(g)}$ is the total energy of the

dimer in gas phase. The adsorption energy formula for a trimer is similar. With this definition, a more negative E_{ads} indicates a stronger adsorption.

Diffusion barriers were calculated using the climbing image nudged elastic band (NEB) method [36]. A number of different diffusion pathways in both stepwise and concerted modes were investigated for each dimer and trimer species in different regions of graphene moiré. The initial and final states are assumed to be the most stable configuration of the diffusing species in each region. We fixed the bottom two Ru layers and allowed the top-layer Ru and graphene to relax during NEB calculations. NEB calculations that did not allow relaxation of C atoms gave energy barriers 0.6-1.5 eV higher than those allowing graphene relaxation, highlighting the importance of local buckling of the graphene layer in adatom and cluster diffusion.

The diffusion path with the lowest energy barrier was chosen to further calculate the hopping rate at room temperature using harmonic transition state theory (hTST) [37, 38]: $k^{hTST} = (\prod_i^{3N} \upsilon_i^{init} / \prod_i^{3N-1} \upsilon_i^{\ddagger}) \exp[-(E^{\ddagger} - E^{init}) / k_B T]$, where $E^{\ddagger}$ and E^{init} is the energy of the transition state (TS) and initial state local minimum (LM), respectively, and the υ_i's are the corresponding normal mode frequencies. In the vibrational frequency calculations, we fixed all Ru and C atoms and only considered the vibration of atoms in the adsorbed ad-species. The resulting vibrational frequencies were computed using finite-difference displacements of 0.04 Å. The hTST method was applied only to single-step diffusion mechanisms. For multi-step mechanisms, a pre-exponential factor of 1×10^{13} s^{-1} was assumed for each individual step and the net prefactor was approximated by $(1/n^2) \times 10^{13}$ s^{-1}, where n is the number of steps in the diffusion path.

A caveat regarding our DFT results is that calculations using GGA-PBE functional generally over-predict adsorption energies and in some circumstances, the local density approximation (LDA) functional gives more accurate results than GGA functionals [39]. No exchange-correlation functional is ideal for all situations, so reliance on any particular functional is a necessary compromise in DFT calculations such as those we report below. Using the PBE functional allowed us to maintain consistency with our earlier results [36].

4.3 Results

4.3.1 Adsorption of Rh_2 and Au_2 on g/Ru(0001)

The adsorption of dimer species was investigated in each different moiré region on g/Ru(0001). The most stable configuration of dimer was found in each region by studying multiple distinct dimer configurations. The adsorption energy of the dimer was calculated, and this energy was compared with the adsorption energy of two well separated monomers on the surface to obtain the dimer formation energy. The results of dimer adsorption for each moiré region are discussed below.

4.3.1.1 Fcc region

The most stable configuration of a Rh dimer in the fcc region is shown in Figure 4.1a. The adsorption energy for this configuration on the surface is –2.85 eV, with a Rh-Rh bond length of 2.55 Å. The dimer is almost horizontal at an average distance of 1.96 Å above the surface, with one atom of the dimer 0.15 Å higher than the other. The nearest underlying *top1* (*top2*) C atoms to the adsorbed Rh_2 are pulled up by ~0.2 (~0.33) Å from their initial positions when no adatom is adsorbed. We performed a similar calculation with the LDA functional, finding that the height of these C atoms was

uniformly ~0.006 Å lower than in our PBE calculations. Compared to the adsorption energy of two Rh monomers in the fcc region (–1.86 eV), the system gains 0.99 eV from bringing two monomers together to form a dimer. The adsorbed dimer is stretched significantly from its gas phase equilibrium bond length (2.21 Å). It is important to note that the adsorption sites for the adatoms in the Rh dimer are different from that of a monomer. Specifically, a Rh monomer binds preferentially near the top of a C atom that is above a first-layer Ru atom (denoted a *top1* site), while the atoms in a Rh dimer prefer to bind at a bridge site and near a *top1* site. Thus, the geometry of the dimer is not simply the addition of two monomers.

The Au dimer, whose most stable configuration can be seen in Figure 4.1b, behaves quite differently from the Rh dimer. The Au dimer is vertical with respect to the surface at a distance of 2.11 Å. The adsorption energy of the dimer is –0.99 eV, with a Au-Au bond length of 2.56 Å. This bond length is similar to the bond length (2.53 Å) in the gas phase. The atom of the dimer that binds to the surface is on top of a C atom that is above a second-layer Ru atom (denoted a *top2* site). This underlying *top2* C atom is lifted up by 0.48 Å from its initial position when no adatom is adsorbed. This binding site is the same as that for a Au monomer, but the system gains 0.44 eV by forming a vertical dimer instead of two separate monomers on the surface. This is in agreement with previous studies that Au dimer prefers to be adsorbed in an upright position perpendicular on graphene, MgO(100), and FeO/Pt(111) surfaces [18, 40-42]. This upright configuration is stabilized because the presence of metal atoms above those directly interacting with the surface increases the adhesion energy and this effect is called the “metal-on-top” stabilization mechanism [43].

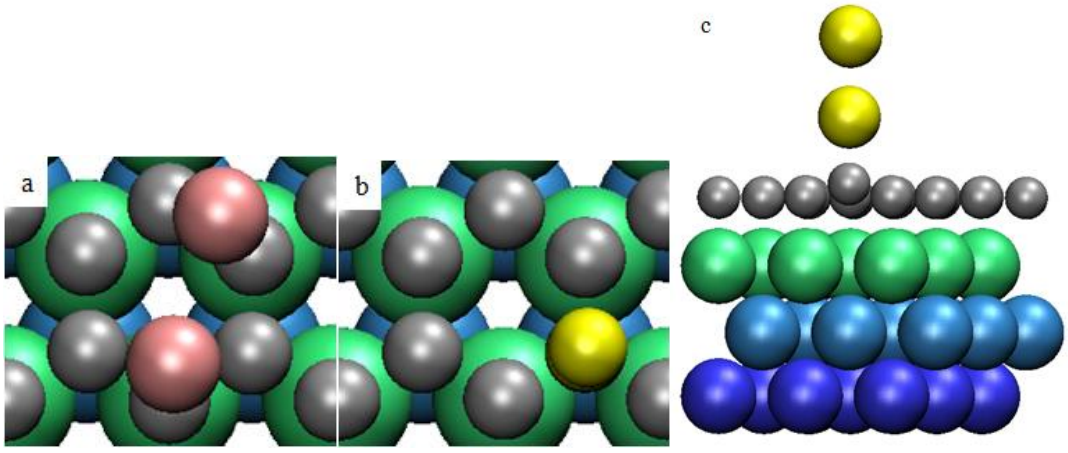

Figure 4.1: The most stable dimer configuration in the fcc region for (a) Rh (pink), top view; (b) Au (yellow), top view; (c) Au, side view. Three Ru (green, light blue, dark blue) layers are shown, with the bottom layer (dark blue) hidden behind the top layer (green) in the top views. The grey atoms are C.

Our calculations described below show that the fcc region is the most favorable binding region for Rh_2 and Au_2. Thus, in our discussion of the net diffusion of dimers on the surface provided below, the most stable configuration of each dimer in the fcc region is the initial and final state for overall diffusion process.

4.3.1.2 Hcp region

Our previous study also shows that the adsorption of metal monomers in the hcp region is weaker than the fcc region [1]. This observation also applies to dimers for which we find the adsorption is less favorable in the hcp region than in the fcc region by 0.27 eV and 0.18 eV for Rh_2 and Au_2, respectively. The most stable configurations of a Rh and Au dimer in the hcp region are shown in Figure C.1 in the Appendix C. The binding site for the dimer in the hcp region is the same as that in the fcc region for both

Rh and Au. Rh_2 is horizontal with respect to the surface with the adsorption energy of –2.58 eV and a Rh-Rh bond length of 2.53 Å. The Rh dimer is about 1.95 Å above the surface, and one atom is 0.14 Å higher than the other atom in the direction normal to the surface. The Au dimer is vertical with respect to the surface with the adsorption energy of –0.81 eV and a Au-Au bond length of 2.55 Å. The lower atom in this dimer is 2.14 Å above the surface.

4.3.1.3 Ridge region

The most stable configurations of Rh_2 and Au_2 in the ridge region are shown in Figure C.2. Both atoms of the Rh_2 dimer are adsorbed at a bridge site (denoted *bri1* since a first-layer Ru atom is directly underneath this site) of graphene. The adsorption energy of the Rh dimer on the ridge region surface is –2.48 eV and the Rh-Rh bond length is 2.51 Å. The dimer is almost flat above the surface at an average distance of 2.03 Å. Au_2 is again vertical with respect to the surface and is also adsorbed at a *bri1* site with an adsorption energy of –0.69 eV. The Au-Au bond distance is 2.52 Å and the lower atom in the dimer is 2.24 Å above the surface.

Comparing the adsorption energy, equilibrium bond length, and height above the surface for each dimer adsorbed in the fcc, hcp, ridge, to the atop region shows a decrease in the adsorption energies and the equilibrium bond lengths and an increase in the height of dimer above the surface. The equilibrium bond lengths in the ridge region are quite similar to those of the gas phase dimers, indicating that the surface in the ridge region has little effect on the adsorbed dimers. It is because the graphene π-bonding network is intact and not sp^3-rehybridized in the ridge region, and thus its surface reactivity does not increase as much as in the fcc and hcp region and the interaction with ad-dimer is purely

van der Waals. The adsorption of dimer is the least favorable in the atop region compared to other regions, where the binding energy is –1.14 eV and –0.45 eV for Rh_2 and Au_2, respectively. We therefore exclude the atop region from our consideration of dimer diffusion across the moiré surface. From our previous monomer results in both the full moiré supercell and smaller (3×3) local regions [1], we found that the fcc region is the global minimum (GM) region, the ridge region is the TS region for monomers, and that the diffusion in the hcp region does not affect the overall barrier for surface diffusion. The results above show that this is also true for metal dimers: the most stable dimer configuration in the fcc region is the GM and the TS for dimer diffusion within the ridge region defines the rate-limiting TS for the overall dimer diffusion across the graphene moiré surface.

4.3.2 Diffusion of Rh_2 and Au_2 on g/Ru(0001)

To describe the diffusion of Rh and Au dimer on the graphene moiré surface, we investigated their diffusion in the fcc and ridge regions. We defined the overall dimer diffusion barrier as the energy difference between the TS in the ridge region and the GM in the fcc region. The diffusion barrier of each dimer within the fcc region was also calculated for comparison. The dimer hopping rate within the fcc region was calculated using hTST by performing vibrational frequency analysis.

4.3.2.1 Dimer diffusion in the fcc region

We performed NEB calculations for multiple different diffusion mechanisms, including both stepwise and concerted motions. The diffusion modes considered for Rh dimer in the fcc region are shown in Figure C.3. The initial and final state is the most

stable dimer configuration in the fcc region. The diffusion mode with the lowest activation energy was taken to be the diffusion mechanism that controls dimer diffusion.

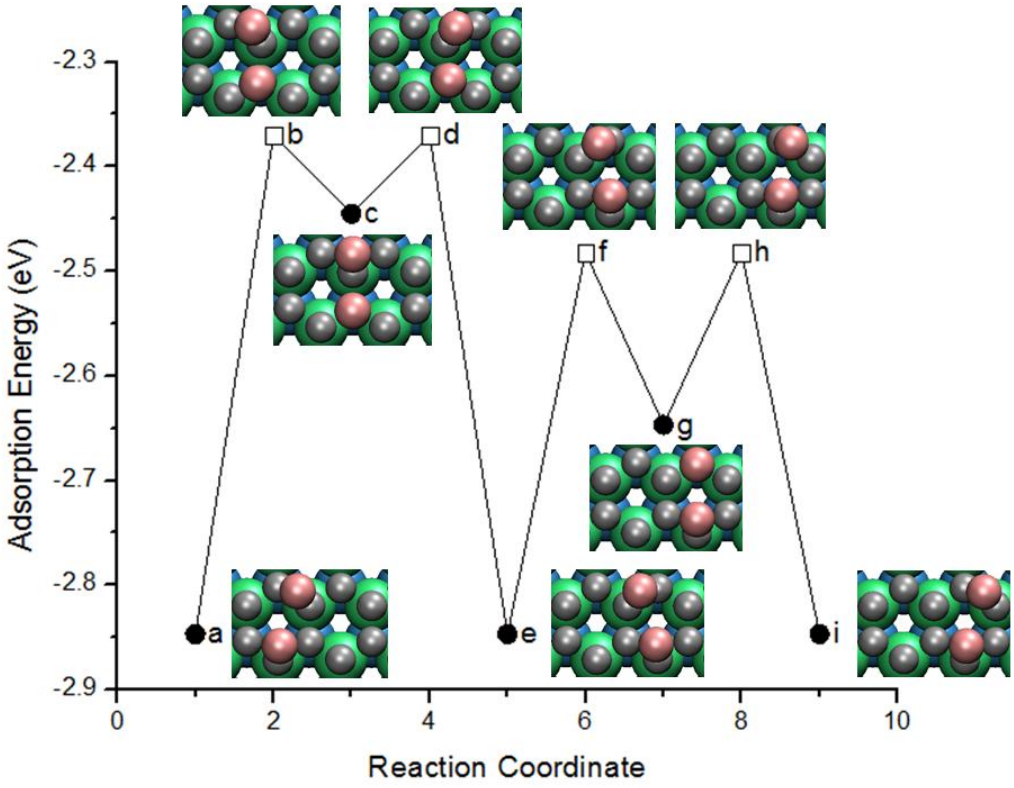

Figure 4.2: The diffusion path of Rh_2 in the fcc region. Circles (squares) indicate stable local minima (transition states). The element colors are the same as before.

For the Rh dimer, diffusion occurs by a stepwise mechanism that goes through four major steps as shown in Figure 4.2. Figure 4.2a, 4.2c, 4.2e, 4.2g, and 4.2i are all LM's. Each figure between two LM's is a TS. Therefore, the total overall energy barrier

for Rh_2 to diffuse by this process within the fcc region is 0.48 eV. The graphene layer buckles with Rh_2 displacement. When Rh_2 diffuses, the underlying C atoms in the TS configuration are lifted up by ~0.2Å from the LM configuration. The diffusion of Rh_2 does not interrupt the sp^3 rehybridization of graphene in the fcc region. Estimating the prefactor for this overall process as described above gives a prefactor of 6.25×10^{11} s^{-1}. The Rh dimer hopping rate within the fcc region at room temperature (300 K) is therefore ~5.40×10^{3} s^{-1}. Comparing this value to the monomer hopping rate of 2.05×10^{9} s^{-1} inside the fcc region at 300 K, the diffusion of Rh_2 is significantly slower.

For a Au dimer, diffusion occurs via a concerted mode that goes through two symmetric steps, as shown in Figure 4.3. The energy barrier for the diffusion is 0.50 eV, and some buckling of the graphene layer occurs during diffusion. With a pre-exponential factor of 2.50×10^{12} s^{-1}, the Au dimer hopping rate within the fcc region at room temperature (300 K) is 9.96×10^{3} s^{-1}. For Au monomer within the fcc region, the hopping rate is 1.71×10^{-1} s^{-1} at 300 K. Thus, at this temperature the diffusion of a Au dimer is orders of magnitude faster than Au monomers within the fcc region.

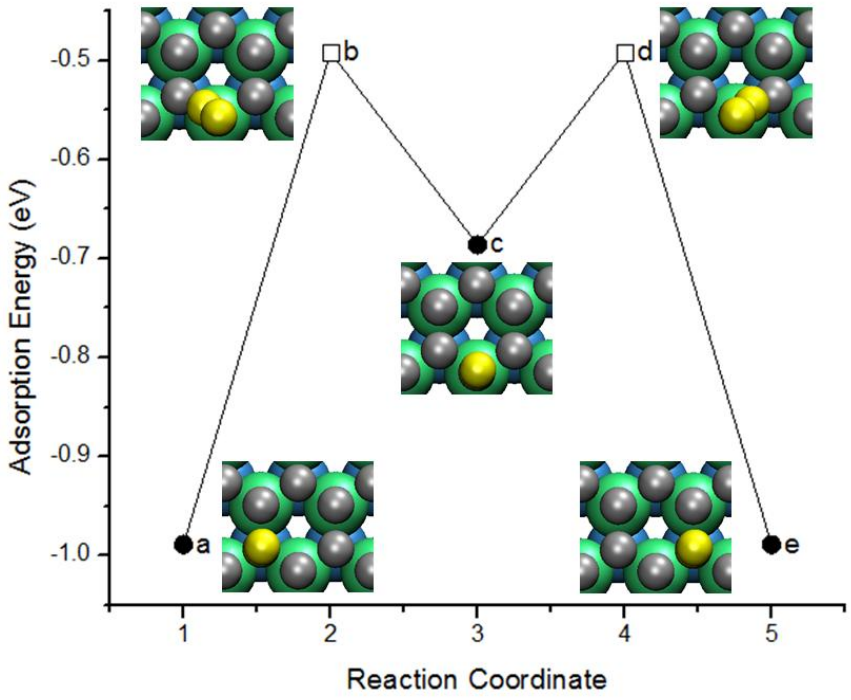

Figure 4.3: The diffusion path of Au_2 in the fcc region. Circles (squares) indicate stable local minima (transition states). The element colors are the same as before.

4.3.2.2 Dimer diffusion across the graphene moiré

To determine the diffusion barrier for the dimer across the graphene moiré, we need to study its diffusion in the ridge region. In the ridge region, NEB calculations were performed by taking the most stable dimer configuration in the ridge region as the initial and final states. Again, both stepwise and concerted modes were investigated.

For a Rh dimer, its diffusion mode in the ridge region is a stepwise mechanism that has a barrier of 0.46 eV. To move from the initial state to final state, Rh dimer has to go through four steps. The TS with the highest energy in this process, which is shown in Figure 4.4a, is also the TS for the overall diffusion across the moiré surface. The energy

difference between this TS and the most stable dimer configuration in the fcc region, 0.82 eV, is the overall diffusion barrier for Rh_2 across the moiré.

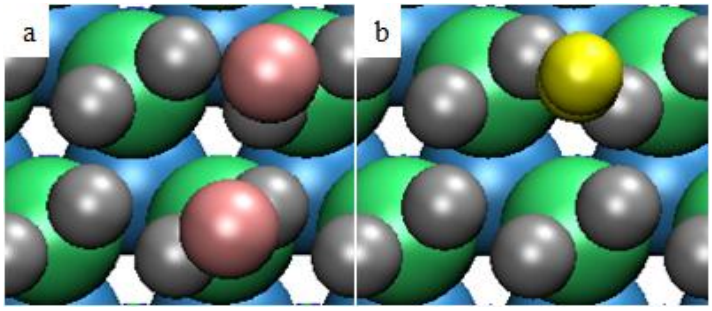

Figure 4.4: The dimer TS for diffusion of (a) Rh and (b) Au in the ridge region, which is also the TS for overall diffusion on graphene moiré. The element colors are the same as before.

Net diffusion across the moiré involves multiple local hops from one carbon ring to another. Since the pre-exponential factor is the rate when temperature is infinitely large, the ratio of net hopping prefactor and local hopping prefactor is the inverse ratio of the mean square distance of the net hopping range and local hopping range. The local hopping within the fcc region is the hop across one carbon ring. The diffusion from the fcc to the ridge region at infinite temperature passes through 3-4 carbon rings. Therefore, the net hopping prefactor is approximately 10 times smaller than the local hopping prefactor in the fcc region. We verified this observation by kinetic Monte Carlo (KMC) simulation of Au monomers hopping on the graphene moiré surface. KMC simulates the time evolution of a system if the rates of all local processes are known given the current

configuration of the atoms. Using a local hopping prefactor of 1×10^{13} s^{-1} in these simulations and performing the KMC simulation at various temperatures gave a net diffusion prefactor of 1.69×10^{12} s^{-1}, which is roughly 1/10 of the local prefactor. We then used the factor of 1/10 to compute the net hopping rate for the rest of the diffusing species in this Chapter. We thus calculated the Rh dimer hopping rate at room temperature (300 K) to be 1.05×10^{-3} s^{-1}, with a pre-exponential factor of 6.25×10^{10} s^{-1}.

The similar procedure was applied to Au dimer. In the ridge region, Au dimer diffuses in a concerted mode with a diffusion barrier of 0.21 eV. The TS is the configuration in between the initial and final states, in which two Au atoms are vertically bound to a bridge site with no Ru atom underneath (denoted as *bri* site). Similar as Rh dimer, the Au dimer TS in the ridge region is the TS for the overall diffusion on the moiré surface and it is shown in Figure 4.4b. Therefore, we can determine the overall diffusion barrier for Au dimer to be 0.51 eV. Using the factor of 1/10, the Au dimer hopping rate at room temperature (300 K) can be calculated to be 6.77×10^{2} s^{-1}, with a pre-exponential factor of 2.50×10^{11} s^{-1}. The hopping rate for a Au monomer is 1.18 s^{-1} on g/Ru(0001) at the same temperature, which is much slower than a Au dimer.

4.3.3 Adsorption of Rh_3 and Au_3 on g/Ru(0001)

The most stable trimer configuration in each moiré region was investigated in a similar way to the dimers. The trimer adsorption energy was calculated. The diffusion path for trimer across the moiré is the same as for dimer based on the reasoning above. Therefore, here we only report the trimer configurations in the fcc and ridge regions, since these define the overall diffusion barrier on the surface.

4.3.3.1 Fcc region

The most stable trimer configuration for Rh in the fcc region is a flat triangle with each adatom adsorbed at a *top2* site (Figure 4.5a). The adsorption energy for this trimer is –3.53 eV. The trimer is at an average of 2.31 Å above the surface with an average Rh-Rh bond length of 2.48 Å. The adsorbed trimer is stretched slightly from its gas phase equilibrium bond length of 2.38 Å.

The most stable trimer configuration for Au in the fcc region is also triangular, but standing up with respect to the surface. The adsorption energy for the trimer is –1.64 eV and the structure is shown in Figure 4.5b. The trimer forms an isosceles triangle, with the base length of 2.72 Å and the side length of 2.68 Å. The base Au atoms are adsorbed at *top2* sites and are 2.52 Å above the surface. The adsorbed trimer has the same side length as the equilibrium bond length of Au trimer in gas phase (2.68 Å). The stretched base Au-Au bond originates from the interaction between the base Au atom and the surface atoms, but the top Au atom shows almost no influence from the substrate.

4.3.3.2 Ridge region

Rh_3 prefers to form a triangular trimer in the ridge region, with each adatom binding to a bridge site of the 6-carbon ring (Figure 4.5d). One adatom binds to *bri1* site and two other adatoms bind to the *bri* site. The adsorption energy is –2.53 eV. The trimer is 2.09 Å above the surface and the average Rh-Rh bond length is 2.59 Å. The bond stretching due to the Rh-surface interaction is more significant and Rh_3 is closer to the surface in the ridge region than in the fcc region.

Au_3 favors a vertical triangular trimer in the ridge region (Figure 4.5e). The lower Au adatoms bind near the *top1* sites where the closest Ru atom to the carbon is a first-

layer Ru. We will refer to the other carbon atop sites in the ridge region as *top2* sites. The adsorption energy of Au trimer is –1.08 eV in the ridge region. The average Au-Au distance of the trimer is 2.72 Å and the trimer is 2.38 Å above the surface.

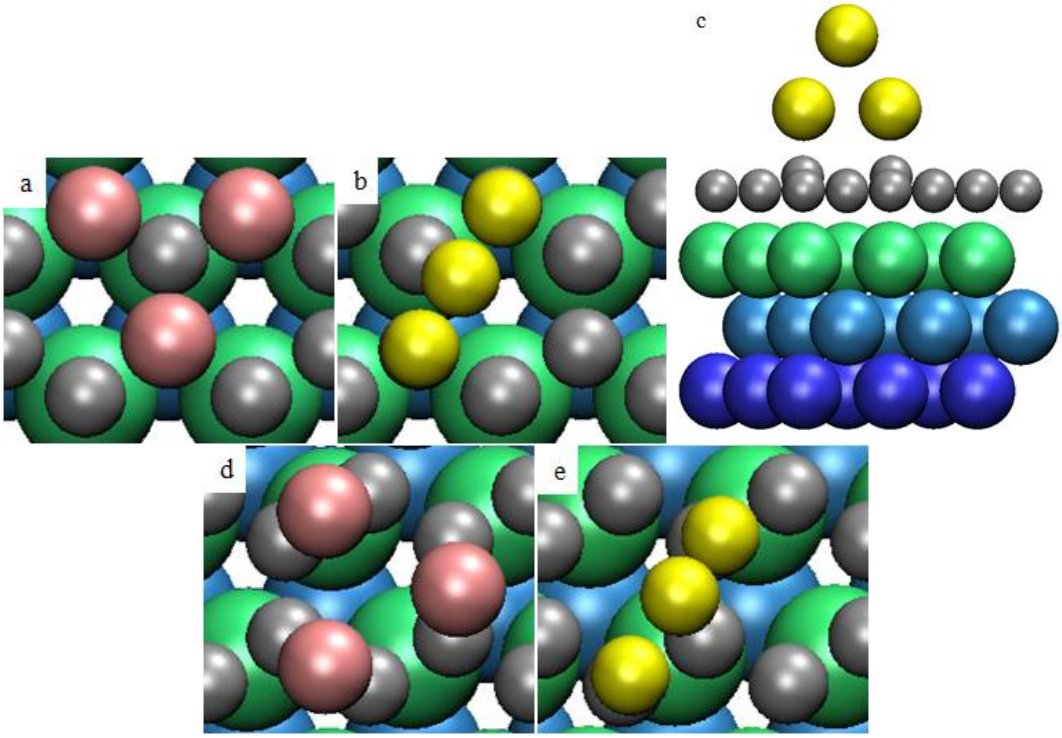

Figure 4.5: The most stable trimer configuration for (a) Rh in the fcc region; (b) Au in the fcc region, top view; (c) Au in the fcc region, side view; (d) Rh in the ridge region; (e) Au in the ridge region. The element colors are the same as for dimers.

4.3.4 Diffusion of Rh_3 and Au_3 on g/Ru(0001)

The diffusion of trimers was investigated using the approach described above for dimers. The calculations were performed using the climbing image NEB method,

assuming the trimer does not dissociate during the diffusion. The overall diffusion barrier on the moiré was estimated to be the energy difference between the trimer TS in the ridge region and the trimer LM in the fcc region. The trimer hopping rate over the graphene moiré surface was calculated using the same approach we used for dimers.

4.3.4.1 Trimer diffusion in the fcc region

The initial and final states in the NEB calculations are the most stable trimer configuration in the fcc region in neighboring two carbon rings. Both stepwise and concerted diffusion modes were investigated. We assigned the trimer diffusion mechanism to be the diffusion mode with the lowest diffusion barrier.

For Rh_3, the diffusion occurs via a concerted mode with the path shown in Figure 4.6. In the TS, trimer adatoms are sitting near *top1* sites. The diffusion barrier is 0.97 eV. Using hTST, the Rh trimer hopping rate within the fcc region at room temperature (300 K) is calculated to be 1.42×10^{-3} s^{-1}, with a pre-exponential factor of 2.41×10^{13} s^{-1}.

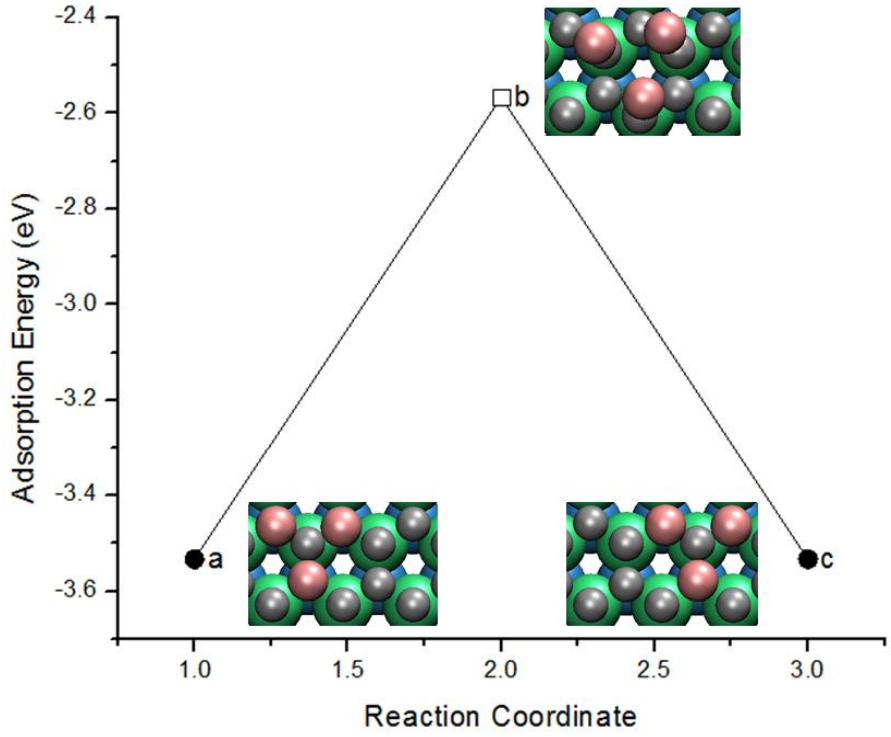

Figure 4.6: The diffusion path of Rh_3 in the fcc region. Circles (squares) indicate stable local minima (transition states). The element colors are the same as before.

The diffusion of Au_3 goes through two steps. In each step, one base adatom stays and two other adatoms moves together to form a "walking" mode. The diffusion path is shown in Figure 4.7. The first step from (a) to (c) is walking across two neighboring carbon rings, which has a diffusion barrier of 0.46 eV. The second step from (c) to (e) is walking within one carbon ring, with a diffusion barrier of 0.23 eV. The overall diffusion barrier for the entire process is therefore 0.46 eV. This corresponds to a Au trimer hopping rate of 4.68×10^{4} s^{-1} at 300 K with the pre-exponential factor of 2.50×10^{12} s^{-1}.

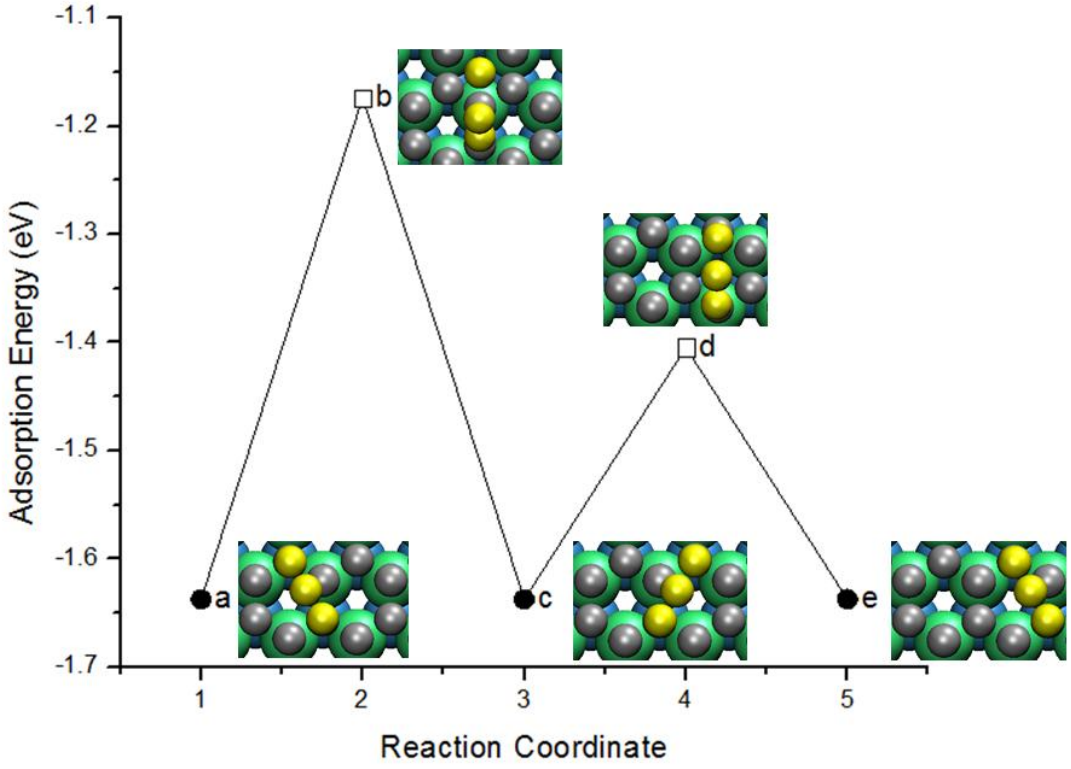

Figure 4.7: The diffusion path of Au_3 in the fcc region. Circles (squares) indicate stable local minima (transition states). The element colors are the same as before.

4.3.4.2 Trimer diffusion across the graphene moiré

We need to determine the diffusion barrier of trimers in the ridge region to calculate the overall barrier on graphene moiré. The initial and final states in the NEB calculations are the most stable trimer configurations in the ridge region in two neighboring carbon rings. As before, both stepwise and concerted diffusion mechanisms were examined.

For Rh_3, the diffusion mechanism is a combination of stepwise and concerted steps (Figure C.4). The net diffusion barrier for Rh_3 in the ridge region is 0.49 eV. The

overall barrier for Rh_3 diffusion on the graphene moiré is thus 1.50 eV. Based on our previous dimer result that the net diffusion prefactor is approximately 1/10 of the local prefactor, we calculated the net Rh_3 hopping rate across the surface at room temperature (300 K) to be 2.08×10^{-13} s^{-1}, with the pre-exponential factor of 2.41×10^{12} s^{-1}. This means that Rh_3 clusters make a negligible contribution to net mass transfer of Rh atoms on this surface.

For a Au trimer, diffusion in the ridge region goes through three steps, with one concerted move and two stepwise moves (Figure C.5). This gives a net diffusion barrier of 0.26 eV for Au_3 in the ridge region, which corresponds to an overall diffusion barrier of 0.81 eV on the graphene moiré surface. We can get a Au_3 hopping rate across the moiré of 6.17×10^{-3} s^{-1} at 300 K, with a pre-exponential factor of 2.50×10^{11} s^{-1}. This means that Au_3 hops much slower than Au monomers and dimers at 300 K.

4.4 Discussion

Comparing our results of Rh and Au monomers, dimers, and trimers together gives insights into how each metal adsorbs and diffuses on the g/Ru(0001) moiré surface.

Table 4.1: The adsorption energy (in eV) for Rh and Au monomer (M_1), dimer (M_2), and trimer (M_3) in the fcc region and the overall diffusing barrier (in eV) across the surface of g/Ru(0001).

	Rh		Au	
(eV)	E_{ads}	E_A	E_{ads}	E_A
M_1	-2.56	0.53	-1.42	0.71
M_2	-2.85	0.82	-0.99	0.51
M_3	-3.53	1.50	-1.64	0.81

Table 4.2: The hopping rate (in s^{-1}) at 300 K for Rh and Au monomer (M_1), dimer (M_2), and trimer (M_3) in the fcc region and the overall surface of g/Ru(0001).

	Rh		Au	
(s^{-1})	fcc	overall	fcc	overall
M_1	2.05×10^{9}	1.10×10^{3}	1.71×10^{-1}	9.97×10^{-1}
M_2	5.40×10^{3}	1.05×10^{-3}	9.96×10^{3}	6.77×10^{2}
M_3	1.42×10^{-3}	2.08×10^{-13}	4.68×10^{4}	6.17×10^{-3}

Table 4.1 contains the adsorption energy in the fcc region and the diffusion barrier across moiré for Rh and Au monomer, dimer, and trimer on g/Ru(0001) and a summary of different rates of these clusters on g/Ru(0001) at 300 K is provided in Table 4.2. For Rh, there is a change in the preferred binding sites in the fcc region as the cluster size increases (from center to bridge to top sites). This shows that the geometry of Rh clusters cannot readily be predicted from the addition of smaller clusters. Rh gains energy by forming larger clusters. Rh clusters are all horizontal with respect to the substrate and the energy needed to diffuse increases monotonically with the cluster size. The diffusion barrier within the fcc region is 0.16 eV, 0.48 eV, and 0.97 eV for Rh_1, Rh_2, and Rh_3, respectively. The barrier to diffuse on the full moiré surface also increases from 0.53 eV to 0.82 eV to 1.50 eV. The energy gained by forming a dimer from two Rh monomers is 0.99 eV, and the energy gain from combining a monomer and a dimer to form a trimer is 1.51 eV. These observations indicate that mass transfer of Rh on the surface at low and moderate temperatures occurs primarily through monomers. In the experiments, most Rh clusters prefer the fcc region but there are a few clusters observed in the hcp and atop region as well [2]. This is consistent with our description of cluster diffusion. Upon

deposition, most adatoms quickly diffuse to the fcc region and once clusters nucleate, their mobility decreases as they grow. The sintering mode is likely to be Ostwald ripening instead of migration of the whole cluster.

For Au, the binding sites remain the same (*top2* site) in the fcc region as the cluster size increases. The adsorption energies of Au_1 (–1.42 eV) and Au_3 (–1.64 eV) in the fcc region are similar, but the adsorption energy of Au_2 (–0.99 eV) is considerably lower. We observe the same trend for the adsorption energy in the ridge region. It is still thermodynamically favorable for Au to form larger clusters. The relatively weak binding of Au_2 explains why Au_2 has the lowest overall diffusion barrier (0.51 eV) on the full moiré surface. On the full moiré surface though, Au_2 diffuses the fastest, followed by Au_1, and then Au_3. Within the fcc region, Au_3 is the fastest diffusing species, followed by Au_2 and Au_1. This indicates that after deposition at room temperature, monomers quickly form dimers and trimers, which are very mobile in the fcc region. Au_2 can easily diffuse across the moiré surface and hence it is likely that these dimers are a building block to form larger Au clusters. If Au transport by dimers and as they aggregate, the most likely morphology of the islands formed is a double-layer structure. The experimental observation that the extended flat Au islands formed on g/Ru(0001) have a close-packed double-layer structure [44, 45] qualitatively supports our prediction of the role of Au dimers in this process.

It is useful to extend our analysis to other 4d and 5d transition metals. The results we obtained for dimer configurations of Rh and Au suggest an efficient method to predict if a metal dimer (or larger clusters) will be a faster diffusing species than monomers on g/Ru(0001). If the dimer prefers to lay flat on the surface, as Rh_2 does, it probably

diffuses more slowly than a monomer. If, however, the dimer prefers to stand up vertically on the surface as Au_2 does, it probably diffuses faster than a monomer. We used this descriptor to classify all 4d and 5d transition on g/Ru(0001). Our results are summarized in Table 4.3. Among the full set of 4d and 5d transition metals, only Re, Ag and Au are Au-like in the sense that their dimers prefer a vertical structure in the fcc region of graphene moiré. The other metals (Y, Zr, Nb, Mo, Tc, Ru, Rh, Pd, La, Hf, Ta, W, Os, Ir, Pt) are Rh-like in that they prefer to form horizontal dimers on the surface. We notice that Mo, Re, Ag and Au correspond to metals with a half-filled or completely filled d-shell (i.e. $4d^5 5s^1$ for Mo and $5d^5 6s^2$ for Re; $4d^{10} 5s^1$ for Ag and $5d^{10} 6s^1$ for Au). It is commonly accepted that a half-filled or completely filled d-shell is more stable than other configurations for d-shell, and thus these metals exhibit similar adsorption behavior. If one assumes that the metal s-graphene sp interaction is weak across the transition metals, then a more stable d-shell results in a less stable adsorption of the metal adatom. The weaker adsorption of metals with a half-filled or completely filled d-shell has been reported for 3d adatoms on freestanding graphene [46, 47]. In the case of a metal dimer, it prefers to have the vertical orientation with respect to the surface. Mo is an exception that prefers horizontal dimers, but its dimer adsorption is indeed weaker than other nearby metals in the periodic table. Our predicted results are consistent with the observation that Rh, Pt, and Ru exhibit similar nucleation behavior on g/Ru(0001) experimentally [2, 44, 48], which is different from Au. This suggests that classifying the dimer structure of each metal gives valuable information about the properties of larger clusters, although the experimental differences between Pd and Rh, Pt, and Ru indicate that this classification is incomplete.

Table 4.3: The adsorption energy of flat and vertical dimer in the fcc region of g/Ru(0001) for all 4d and 5d transition metals. The reference state is the bare fcc region and the dimer in gas phase. The dimer is adsorbed at the most preferred site for both orientations.

metal	E_{ads_flat} (eV)	E_{ads_ver} (eV)
Y	-3.72	-2.54
Zr	-3.48	-3.25
Nb	-3.16	-2.44
Mo	-2.08	-1.13
Tc	-9.99	-9.86
Ru	-3.50	-2.84
Rh	-2.51	-1.56
Pd	-4.03	-2.89
Ag	-1.29	-1.45
La	-4.92	-1.49
Hf	-3.93	-3.24
Ta	-4.40	-2.86
W	-3.11	-1.53
Re	-2.58	-5.18
Os	-3.68	-3.30
Ir	-4.59	-4.22
Pt	-4.32	-2.65
Au	-0.81	-0.99

4.5 Conclusions

We have examined the small metal cluster adsorption and diffusion on g/Ru(0001) and compared to our previous study of monomers. In particular, we studied Rh and Au, two metal species that exhibit distinctively different behaviors when forming clusters on g/Ru(0001). We have determined the lowest-energy structure, the diffusion barrier, and the room temperature hopping rate for Rh and Au dimers and trimers. All of

our calculations used DFT with the GGA-PBE functional. We cannot exclude the possibility that other exchange-correlation functionals could make different predictions for some cases. Our study show that Rh monomers diffuse faster than dimers and trimers. For Au, however, dimers diffuse faster than monomers and trimers on the moiré surface. This difference in diffusion behaviors is directly associated with the cluster orientation with respect to the surface. We also studied the orientation of dimers for all 4d and 5d transition metals on the surface. This analysis suggests that Re and Ag also form dimers that diffuse faster than monomers on the g/Ru(0001) surface, but that all other metals have diffusivities that decrease monotonically with cluster size.

4.6 References

[1] L. Semidey-Flecha, D. Teng, B. Habenicht, D.S. Sholl, Y. Xu, J. Chem. Phys., 138 (2013) 184710.

[2] Z.H. Zhou, F. Gao, D.W. Goodman, Surf. Sci., 604 (2010) L31-L38.

[3] Y. Pan, H.G. Zhang, D.X. Shi, J.T. Sun, S.X. Du, F. Liu, H.J. Gao, Adv. Mater., 21 (2009) 2777-2780.

[4] J. Wintterlin, M.L. Bocquet, Surf. Sci., 603 (2009) 1841-1852.

[5] S. Marchini, S. Gunther, J. Wintterlin, Phys. Rev. B, 76 (2007) 075429.

[6] B. Wang, M.L. Bocquet, S. Marchini, S. Gunther, J. Wintterlin, Phys. Chem. Chem. Phys., 10 (2008) 3530-3534.

[7] A.F. Voter, Phys. Rev. B, 34 (1986) 6819-6829.

[8] J.M. Wen, S.L. Chang, J.W. Burnett, J.W. Evans, P.A. Thiel, Phys. Rev. Lett., 73 (1994) 2591-2594.

[9] S.C. Wang, G. Ehrlich, Phys. Rev. Lett., 79 (1997) 4234-4237.

[10] J.T. Goldstein, C. Ehrlich, Surf. Sci., 443 (1999) 105-115.

[11] G. Ehrlich, Surf. Sci., 246 (1991) 1-12.

[12] W. Xu, J.B. Adams, Surf. Sci., 339 (1995) 247-257.

[13] K. Stolt, W.R. Graham, G. Ehrlich, J. Chem. Phys., 65 (1976) 3206-3222.

[14] H.W. Fink, G. Ehrlich, Surf. Sci., 150 (1985) 419-429.

[15] A.W. Signor, J.H. Weaver, Phys. Rev. B, 84 (2011) 165441.

[16] L.J. Xu, G. Henkelman, C.T. Campbell, H. Jonsson, Phys. Rev. Lett., 95 (2005) 146103.

[17] L.J. Xu, G. Henkelman, C.T. Campbell, H. Jonsson, Surf. Sci., 600 (2006) 1351-1362.

[18] G. Barcaro, A. Fortunelli, New J. Phys., 9 (2007) 22.

[19] R. Ferrando, A. Fortunelli, J. Phys.-Condens. Matter, 21 (2009) 264001.

[20] L.B. Vilhelmsen, K.S. Walton, D.S. Sholl, J. Am. Chem. Soc., 134 (2012) 12807-12816.

[21] D.S. Sholl, R.T. Skodje, Phys. Rev. Lett., 75 (1995) 3158-3161.

[22] D.S. Sholl, J.A. Steckel, Density functional theory: a practical introduction, Wiley, Hoboken, N.J., 2009.

[23] G. Kresse, J. Furthmuller, Comp. Mater. Sci., 6 (1996) 15-50.

[24] G. Kresse, J. Furthmuller, Phys. Rev. B, 54 (1996) 11169-11186.

[25] G. Kresse, J. Hafner, Phys. Rev. B, 47 (1993) 558-561.

[26] G. Kresse, J. Hafner, Phys. Rev. B, 49 (1994) 14251-14269.

[27] J.P. Perdew, K. Burke, M. Ernzerhof, Phys. Rev. Lett., 77 (1996) 3865-3868.

[28] J.P. Perdew, K. Burke, M. Ernzerhof, Phys. Rev. Lett., 78 (1997) 1396-1396.

[29] M. Methfessel, A.T. Paxton, Phys. Rev. B, 40 (1989) 3616-3621.

[30] P.E. Blochl, Phys. Rev. B, 50 (1994) 17953-17979.

[31] G. Kresse, D. Joubert, Phys. Rev. B, 59 (1999) 1758-1775.

[32] D.E. Jiang, M.H. Du, S. Dai, J. Chem. Phys., 130 (2009) 074705.

[33] K.T. Chan, J.B. Neaton, M.L. Cohen, Phys. Rev. B, 77 (2008) 235430.

[34] L.B. Hu, X.R. Hu, X.B. Wu, C.L. Du, Y.C. Dai, J.B. Deng, Phys. B-Condens. Matter, 405 (2010) 3337-3341.

[35] B. Wang, S. Gunther, J. Wintterlin, M.L. Bocquet, New J. Phys., 12 (2010) 043041.

[36] G. Henkelman, B.P. Uberuaga, H. Jonsson, J. Chem. Phys., 113 (2000) 9901-9904.

[37] G.H. Vineyard, J. Phys. Chem. Solids, 3 (1957) 121-127.

[38] C. Wert, C. Zener, Phys. Rev., 76 (1949) 1169-1175.

[39] P.J. Feibelman, Phys. Rev. B, 77 (2008) 165419.

[40] M. Amft, B. Sanyal, O. Eriksson, N.V. Skorodumova, J. Phys.-Condens. Matter, 23 (2011) 205301.

[41] R.H. Ouyang, W.X. Li, Phys. Rev. B, 84 (2011) 165403.

[42] V. Simic-Milosevic, M. Heyde, N. Nilius, T. Konig, H.P. Rust, M. Sterrer, T. Risse, H.J. Freund, L. Giordano, G. Pacchioni, J. Am. Chem. Soc., 130 (2008) 7814-7815.

[43] G. Barcaro, A. Fortunelli, J. Chem. Theory Comput., 1 (2005) 972-985.

[44] L. Liu, Z.H. Zhou, Q.L. Guo, Z. Yan, Y.X. Yao, D.W. Goodman, Surf. Sci., 605 (2011) L47-L50.

[45] Y. Xu, L. Semidey-Flecha, L. Liu, Z.H. Zhou, D.W. Goodman, Faraday Discuss., 152 (2011) 267-276.

[46] H. Valencia, A. Gil, G. Frapper, J. Phys. Chem. C, 114 (2010) 14141-14153.

[47] O.V. Yazyev, A. Pasquarello, Phys. Rev. B, 82 (2010) 045407.

[48] E. Sutter, B. Wang, P. Albrecht, J. Lahiri, M.L. Bocquet, P. Sutter, J. Phys.-Condens. Matter, 24 (2012) 314201.

CHAPTER 5

ENERGETICS OF AU_8 ON GRAPHENE/RU(0001)

5.1 Introduction

Gold nanoparticles have exhibited incredible catalytic activity [1-3]. Since Haruta *et al*. showed that nanosized Au particles (< 5 nm) can be very effective catalysts [4], extensive studies have been carried out of the high catalytic activity of Au nanoparticles in various chemical processes, including low temperature CO oxidation [3-7], selective hydrogenation [8], NO_x reduction [9, 10], hydrogen peroxide formation [11], propene epoxidation [12, 13], and water-gas shift chemistry [14, 15]. Mechanistic studies on the catalytic activity of nanosized Au in low temperature oxidation reactions indicate the importance of the synergistic effects between Au and oxide substrates [16] and the Au sites with low coordination number [17]. To study the intrinsic catalytic activity of nanosized Au, it is therefore of interest to study Au clusters on an oxygen-free substrate.

One challenge in heterogeneous catalysis is to synthesize supported metal particles with maximum control over their composition and structure. To serve this purpose, the desired substrate needs to have well separated nucleation sites to disperse metal clusters so that they can be stabilized against aggregation [18]. One example of such a material that is also oxygen-free is the graphene moiré on metal substrates, e.g. Ir(111) [19] or Ru(0001) [20]. The graphene moiré supported by Ru(0001) (denoted g/Ru(0001)) consists of three distinct binding regions: atop, fcc, and hcp regions [21, 22]. The atop region is a region of the graphene moiré with the atop site for the first layer of metal substrate centered in the carbon ring. The fcc and hcp regions are the two lower

regions where half of the carbon atoms are directly above the first layer of metal substrate atoms. These two regions are distinguished by which threefold coordinated hollow site is centered in the carbon ring. The intermediate region between the fcc and hcp regions is called the ridge region.

Our earlier studies of small Au clusters (Au_1, Au_2, Au_3) on g/Ru(0001) have provided us useful information and insight to understand Au cluster nucleation and growth on the graphene moiré surface [23-25]. Specifically, we studied the adsorption and diffusion of small Au clusters in the fcc (local minimum region) and ridge region (transition state region) and predicted that Au_2 is the fastest diffusing of these small species on g/Ru(0001) and is likely the building block to form large Au clusters. In order to gain a better understanding of the formation mechanism of Au islands on g/Ru(0001), which have a close-packed double-layer structure [20, 26], it is important to investigate larger Au clusters and study their lowest energy structures on the surface. Supported Au_8 clusters are known experimentally to exhibit a high chemical activity [2] and thus are worthy of investigation as examples of moderate size clusters. A recent study of the Au_8 cluster on MgO(100) rationalized its high activity by predicting a high O_2 binding energy (up to 1 eV) to the cluster [27]. This motivated us to characterize Au_8 clusters on g/Ru(0001).

Characterizing clusters with more than a few atoms is challenging because of the large configurational space we have to examine. Roughly speaking, the computational effort scales exponentially with cluster size, because the number of candidate local energy minima grows exponentially with the number of atoms. To address this challenge, we adopted a Genetic Algorithm (GA) combined with Density Functional

Theory (DFT) calculations to scan for low energy Au_8 structures on g/Ru(0001). This method has previously been successfully applied to study Au clusters on MgO(100) *F* centers [27] and large metal clusters in metal organic frameworks materials [28, 29].

In this Chapter, we address the issue of energetics of Au_8 cluster in the fcc and ridge region of g/Ru(0001) by reporting the GA-DFT calculation results of the lowest-energy cluster structures in these regions and estimating the diffusion barrier for Au_8 cluster. The most stable Au_8 cluster structure provides us insight into the formation mechanism of Au double-layer islands on g/Ru(0001).

5.2 Methods

A GA was used to systematically search for low energy structures of adsorbed Au_8 on g/Ru(0001). The implemented GA was recently developed for adsorbed clusters [27, 28]. The GA follows the scheme proposed by Deaven and Ho [30] with several improvements making the method more suitable for computationally expensive DFT calculations [27]. The optimization process contains two steps, in which a structural candidate is first relaxed in LCAO mode in the Grid-based Projector Augmented Wave (GPAW) DFT code [31, 32] and subsequently in the Vienna *Ab Initio* Simulation Package (VASP) [33-36] in a plane wave calculation if it is structurally different from previously encountered structures. The LCAO mode uses a basis set of atomic orbital-like functions rather than grid-based wave functions, which makes calculations considerably cheaper and faster. We used it to do fast initial relaxations and then plane-wave DFT calculations in VASP with core electrons described by the projector augmented-wave (PAW) method [37, 38]. All DFT calculations [39] were spin-polarized and we used a cutoff energy of 400 eV with the Perdew-Burke-Ernzerhof (PBE) [40, 41]

exchange-correlation functional within the generalized gradient approximation. First-order Methfessel-Paxton smearing [42] was used with a width of 0.2 eV. The reciprocal space is sampled with Γ point only. The optimized Ru lattice constant, a = 2.726 Å and c = 4.035 Å, and the graphene lattice constant, a = 2.46 Å, are in good agreement with reported experimental and computational values [43-46].

For Au_8 clusters in the fcc and ridge region of g/Ru(0001), energy minimization was achieved by placing an Au_8 cluster on top of a (5×5) supercell with a vacuum space of 18 Å to separate the Ru slab replicas. A 2-layer Ru(0001) slab was used in GA to reduce computational time. After several low energy Au_8 structures were identified in GA process, a 3-layer Ru(0001) was used in DFT calculations for further relaxation. Each supercell contains a layer of graphene on top of a 2-layer (3-layer) Ru(0001) slab, giving a total of 50 C atoms and 50 (75) Ru atoms. The graphene was slightly stretched to match the lattice constant of Ru surface. In the supercell, the graphene layer was shifted horizontally in different extents with respect to the Ru slab to expose different sites of Ru through the center of 6-carbon rings [23, 25]. The in-plane coordinates of two adjacent carbon atoms were constrained to keep the graphene in the right relative position with respect to Ru surface [24]. Ground-state energy calculations were performed with the bottom layer (two layers) of Ru slab fixed for the 2-layer (3-layer) Ru. All other atoms were allowed to fully relax.

A GA scheme consists of several steps. A starting population of 15 random Au_8 structures was generated and they were first relaxed in LCAO mode using GPAW and then in VASP through quasi-Newton optimization until the maximum force on any atom was below 0.05 eV/Å. Our implementation introduces a new structural comparison

criterion to determine if the two structures are similar. For two structures to be considered equivalent, the energy difference needs to be smaller than ΔE = 0.02 eV and the relative signed difference between a sorted list of all inter-atomic distances for each cluster needs to be smaller than 1.5% with no single difference larger than 0.7 Å [27]. We employed a two-step DFT optimization technique where a candidate is first relaxed in LCAO mode in GPAW and subsequently in VASP only if it is structurally different from previously encountered structures. This new technique reduces the computational cost since all rough optimizations are done with the fast LCAO mode and only a few relaxation steps are required with the computational expensive method in VASP. A population of 15 structurally different candidates with the lowest energies was maintained and used to generate new structures.

To ensure a survival of the fittest scheme, the most stable candidates need to be selected for pairing more frequently than their less stable counterparts. Each parent candidate was thus assigned a fitness F_i related to its energy and was selected with a probability P_i proportional to its fitness. To help ensure a diverse population, we chose to multiply F_i with a uniqueness factor U_i that decreases the probability of candidate i if it has previously been used for pairing or existing structures similar to it are outside of the population. The detailed expression of each term can be found in Reference [28]. The inclusion of U_i is a new addition to GA optimization methods.

When two structures have been selected for pairing, they are paired together through a cut-and-splice operator [30]. There is a 50% probability that the offspring candidate undergoes one of three mutations: rattle, twist, and close packing [27]. Close packing mutation is an additional implementation to the traditional GA scheme. More

details on the mutations in GA can be found in the Supporting Information of Reference [27].

The adsorption energy of an Au_8 cluster on the surface was given by $E_{ads} = E_{Au8+surface} - E_{surface} - E_{Au8(g)}$, where $E_{Au8+surface}$ and $E_{surface}$ are the total energies of the surface with and without the Au_8 cluster, and $E_{Au8(g)}$ is the total energy of the most stable Au_8 cluster in gas phase, whose structure is shown in Figure 5.1. With this definition, a more negative E_{ads} indicates a stronger adsorption. The lowest energy Au_8 structure in vacuum was found in a previous GA study of small gold clusters [47]. It is planar and the nearest-neighbor distance is 2.625 Å.

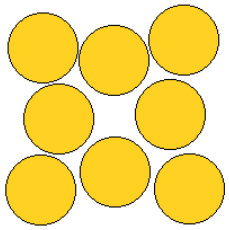

Figure 5.1: The lowest energy vacuum structure of Au_8 cluster [28, 47].

To analyze the adsorbed clusters, we looked at the net atomic charge of the cluster computed by both the Bader method [48] and the density derived electrostatic and chemical (DDEC) [49, 50] charges method. The Bader method partitions the total

electron density into non-overlapping atomic volumes whose surfaces are perpendicular to the electron density gradient [48]. The DDEC method partitions the total electron density into overlapping atomic distributions that are simultaneously optimized to be chemically meaningful and to reproduce the electrostatic potential surrounding a material [49]. Bader charges were computed using the program of Henkelman and co-workers [51, 52]. DDEC charges were computed using the program available at ddec.sourceforge.net, which implements the method described by Manz and Sholl [50].

A simulated scanning tunneling microscopy (STM) image was obtained for the most stable Au_8 cluster in the fcc region of g/Ru(0001) using STRender [53], which is a java program for a 3D visualization of atomic and magnetic structures. The simulated STM image illustrates the appearance of Au_8 cluster in the fcc region if it were observed experimentally.

A caveat regarding our results is that DFT calculations using GGA-PBE functional generally over-predict adsorption energies and in some circumstances, the local density approximation (LDA) functional gives more accurate results than GGA functionals [18]. No exchange-correlation functional is ideal for all situations, so reliance on any particular functional is a necessary compromise in DFT calculations such as those we report below. Using the PBE functional allowed us to maintain consistency with our earlier results [23-25].

5.3 Results and Discussion

5.3.1 Adsorption of Au_8 in the fcc region

We demonstrated in Chapters 2 and 4 that the fcc region is the most stable region for small Au clusters [23, 24]. The GA was used to test 107 different Au_8 candidates in

the fcc region. A histogram of the energies for these 107 structures relative to the most stable one can be seen in Figure 5.2. The structures are ranked in an energy-ascending order. The results of the 6 low energy Au_8 structures in the fcc region of g/Ru(0001) obtained by GA are summarized in Table 5.1. The adsorption energy of each cluster was calculated and the cluster charge using both Bader and DDEC method was reported. The adsorption site for all Au_8 clusters is the *top2* carbon site on the graphene moiré, where a 2^{nd}-layer Ru atom is directly under the C atom. This is consistent with the preferred adsorption site determined for Au_1, Au_2, and Au_3 in the fcc region of g/Ru(0001) [23, 24]. Two different adsorption energies are reported for each cluster, where the surface slab has either 2 layers or 3 layers of Ru(0001). The difference in the adsorption energy using different numbers of Ru layer results from the interlayer relaxation of the g/Ru(0001) slab, not structural change of the Au_8 cluster. The energy order varies slightly with the increase of Ru layers, but the most stable Au_8 structure stays the same. Charge analysis was performed on Au_8 clusters on g/Ru(0001) slab with 3 layers of Ru. Both charge methods indicate that all Au_8 clusters gain electrons (except structure F2 characterized using the Bader method), but there is no clear trend observable in the charges with respect to the descending adsorption energy. Instead, the DDEC charges for all clusters are (-0.35 ± 0.07) *e*. This shows that charge transfer is not the dominant reason for structure F1 to be energetically more favorable than other structures.

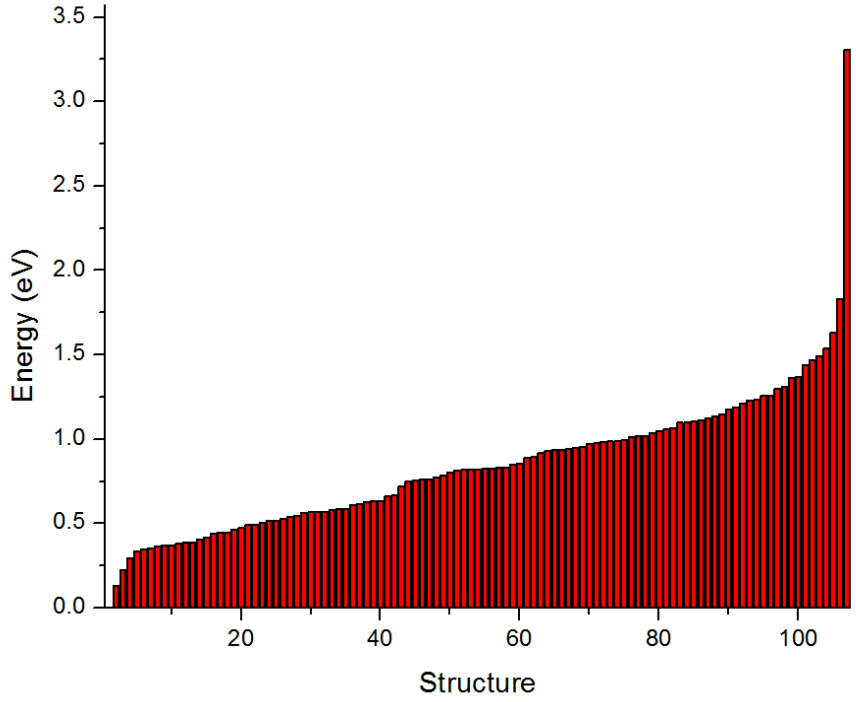

Figure 5.2: A histogram of the relative energies (in eV) compared to Structure #1 (F1) for all 107 Au_8 candidates in the fcc region of g/Ru(0001) generated from GA. They are ranked in energy-ascending order. Structure #1 (F1) has the lowest energy, for which the relative energy to itself is zero. All the other structures have higher (more positive) energies, which indicate weaker adsorption.

Table 5.1: The adsorption energy and charge of the 6 low energy Au_8 clusters in the fcc region of g/Ru(0001). Two different surface slabs were used, with graphene on top of a 2-layer Ru(0001) and a 3-layer Ru(0001).

Au_8 structure	E_{ads_Ru2L} (eV)	E_{ads_Ru3L} (eV)	Bader charge (*e*)	DDEC charge (*e*)
F1 (Figure 5.3)	-1.55	-2.10	-0.05	-0.30
F2 (Figure D.1b)	-1.41	-1.99	0.01	-0.29
F3 (Figure D.1c)	-1.33	-1.87	-0.11	-0.36
F4 (Figure D.1d)	-1.21	-1.67	-0.03	-0.28
F5 (Figure D.1e)	-1.21	-1.82	-0.16	-0.47
F6 (Figure D.1f)	-1.20	-1.58	-0.20	-0.39

The atomic structure of the most stable Au_8 structure (F1) in the fcc region with 2 layers of Ru is shown in Figure 5.3. The other seven structures are shown in Figure D.1 in Appendix D. In Figure 5.3, Au_8 cluster forms a double-layer "wall", of which the upper layer is 5 Å above the graphene surface. Four Au atoms are bound with an average distance of 2.16 Å above four *top2* C atoms that are lifted 0.40 Å higher than other C atoms. The average nearest neighbor Au-Au distance is 2.68 Å, which is 0.05 Å larger than the nearest neighbor distance (2.625 Å) of Au_8 in vacuum [47]. When number of Ru layers increases to 3, the Au_8 cluster binds 0.02 Å closer to the graphene surface, but the cluster structure has the same average nearest neighbor Au-Au distance as using 2 layers of Ru. The simulated STM image of this Au_8 configuration is shown in Figure 5.3c. The double-layer Au wall and the underlying Ru(0001) pattern can be seen, but the hexagonal graphene structure is not observable.

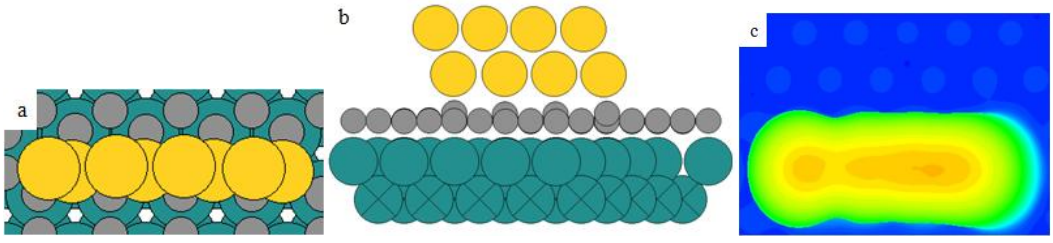

Figure 5.3: The most stable Au_8 (yellow) cluster adsorbed in the fcc region of graphene (grey) / Ru(0001) (green) with 2 layers of Ru. (a): Top view; (b): Side view. Fixed Ru atoms are labeled with X's; (c): Simulated STM image.

We have also studied the effect of unit cell size on the adsorption energy of Au_8 clusters. A (6×6) supercell of g/Ru(0001) was used with 3 layers of Ru. The results are tabulated in Table D.1 in Appendix D. The energy order is the same as using a (5×5) supercell, but the adsorption energy increases an average of 0.57 eV for all structures. This implies that the energy gained from Au_8 interacting with its periodic images is considerable in the data in Table 5.1, but it does not affect the relative stability of different Au_8 structures.

5.3.2 Adsorption of Au_8 in the ridge region

As shown in Chapter 2, the ridge region has been identified the least strongly adsorbed region that a small Au cluster passes through during its diffusion (transition state region) [23, 24]. The GA was used to test 112 different Au_8 candidates in the ridge region. A histogram of the energies for these 112 structures relative to the most stable one can be seen in Figure 5.4. The structures are ranked in an energy-ascending order. Table 5.2 exhibits the adsorption energy and charge of the 6 low energy Au_8 cluster structures in the ridge region of g/Ru(0001). As shown in Figure 5.5 and Figure D.2 in Appendix D, these 6 Au_8 structures are similar to the configuration of Au_8 in vacuum (see Figure 5.1), but are bent or twisted in different degrees. The difference in the adsorption energy exhibited among structures B1 to B6 originates partly from the different adsorption sites on the graphene moiré surface. The addition of a third Ru layer contributes to the decrease of the adsorption energy by an average of 0.08 eV in the ridge region, which is much smaller than the same contribution to the average increase of the adsorption energy (0.50 eV) in the fcc region. Calculations with a third Ru layer show that two Au_8 structures, B1 and B3, have the same adsorption energy and are both the

lowest energy structure in the ridge region. Compared to the fcc region, the relatively weak adsorption energies indicate that the ridge region of g/Ru(0001) interacts weakly with the adsorbed Au_8, which is also supported from the fact that all 6 low energy Au_8 structures deform very little from the most stable Au_8 structure in vacuum. All the Au_8 structures gain electrons using both Bader and DDEC charge analysis. The Bader charges are similar for all structures, but DDEC charges indicate that B1, B2, B4, and B6 obtain the same charge (~0.23 *e*), which is 0.1 *e* more significant than the charge transfer in B3 and B5 (–0.13 *e*) in the ridge region.

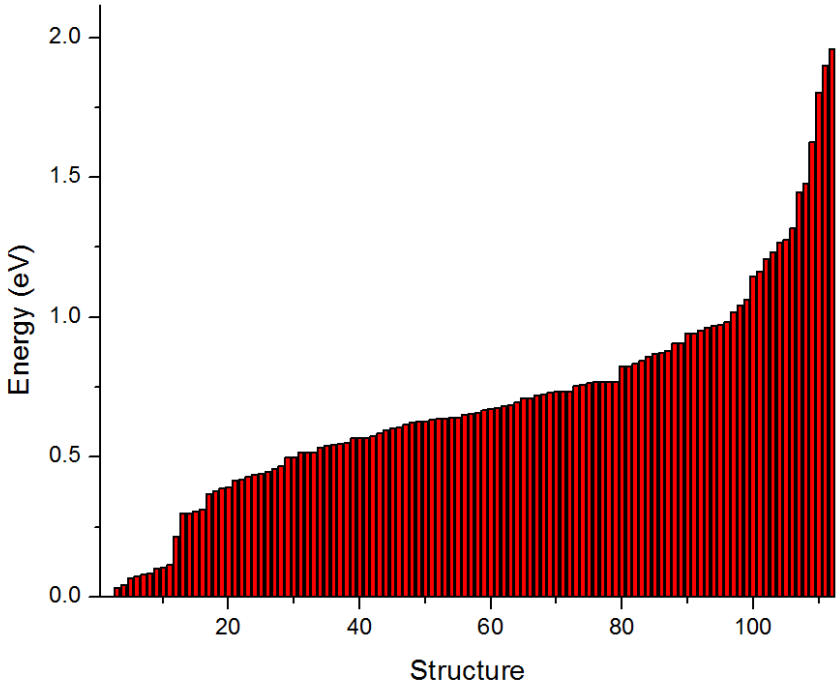

Figure 5.4: A histogram of the relative energies (in eV) compared to Structure #1 (B1) for all 112 Au_8 candidates in the ridge region of g/Ru(0001) generated from GA. They are ranked in energy-ascending order. Structure #1 (B1) has the lowest energy, for which the relative energy to itself is zero. All the other structures have higher (more positive) energies, which indicate weaker adsorption.

Table 5.2: The adsorption energy and charge of the 6 low energy Au_8 clusters in the ridge region of g/Ru(0001). Two different surface slabs were used, with graphene on top of a 2-layer Ru(0001) and a 3-layer Ru(0001).

Au_8 structure	E_{ads_Ru2L} (eV)	E_{ads_Ru3L} (eV)	Bader charge (*e*)	DDEC charge (*e*)
B1 (Figure 5.5)	-0.34	-0.22	-0.08	-0.23
B2 (Figure D.2b)	-0.32	-0.21	-0.07	-0.22
B3 (Figure D.2c)	-0.29	-0.22	-0.08	-0.13
B4 (Figure D.2d)	-0.27	-0.20	-0.10	-0.22
B5 (Figure D.2e)	-0.26	-0.19	-0.07	-0.13
B6 (Figure D.2f)	-0.25	-0.17	-0.10	-0.22

The top and side view of the most stable Au_8 structure (B1) in the ridge region with 2 layers of Ru was provided in Figure 5.5, while the rest of the structures are given in Figure D.2 in Appendix D. As shown in Figure 5.5, Au_8 forms a 3-D compact structure, in which two Au atoms are directly bound to the surface with an average distance of 2.37 Å. The average nearest neighbor Au-Au distance is 2.64 Å. This value is 0.02 Å larger than that of Au_8 in vacuum (2.625 Å), which indicates a closer resemblance to Au_8 structure in vacuum than the Au_8 structure in the fcc region. When number of Ru layers increases to 3, the Au_8 cluster binds 0.02 Å closer to the graphene surface, but the cluster structure stays the same.

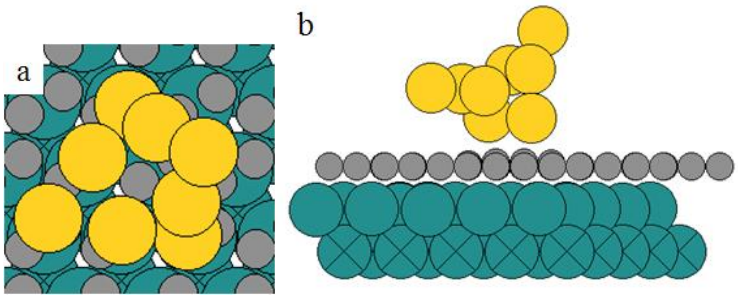

Figure 5.5: The most stable Au_8 (yellow) cluster adsorbed in the ridge region of graphene (grey) / Ru(0001) (green) with 2 layers of Ru. (a): Top view; (b): Side view. Fixed Ru atoms are labeled with X's.

The overall diffusion barrier for Au_8 on the g/Ru(0001) surface was estimated by examining cluster adsorption in the fcc and ridge region, since they are local minimum and transition state region, respectively. From the adsorption energy of the most stable Au_8 structure in these two regions, we calculated the lower bound of the diffusion barrier for Au_8 to be 1.21 eV (1.88 eV) on g/Ru(0001) with 2-layer (3-layer) Ru. This value indicates that it is unlikely for Au_8 to diffuse as a whole at moderate temperatures. In Chapters 2 and 4, we showed that the diffusion barrier of Au_1, Au_2, and Au_3 on g/Ru(0001) obtained from DFT calculations is 0.71 eV, 0.51 eV, and 0.81 eV, respectively. The diffusion of a Au_8 cluster is therefore orders of magnitude slower than smaller Au clusters on g/Ru(0001) at room temperature.

We thus propose that mass transfer during growth of Au clusters probably occurs through the dissociation of Au adatoms from the larger clusters. The sequential detachment of Au adatom instead of Au dimers from the larger cluster is strongly suggested by the thermochemistry of these processes. DFT calculations examining these two processes showed that detaching a Au dimer from Au_8 to form Au_6 + Au_2 is

energetically unstable by 1.57 eV, while the equivalent energy to remove a Au monomer from Au_8 is 0.91 eV. In both cases, the energy barrier associated with this process must be higher than these energies. This implies that pulling away a Au adatom from a large cluster is more likely than pulling away a Au dimer. When Au adatoms diffuse on the surface, they meet each other and form dimers that are more stable and, as shown earlier, diffuse faster than the individual monomers. These diffusing dimers subsequently coalesce and stack into double-layer islands. It is thus proposed that Au clusters sinter in the mode of Ostwald ripening instead of cluster agglomeration. In Ostwald ripening, surface adatoms of a smaller particle tend to detach from the particle and diffuse on the surface [54]. As more adatoms diffuse freely on the surface, they have a tendency to coalesce on the surface of larger particles. Eventually, smaller particles shrink while larger particles grow. In our case, all our results imply that the growth mechanism of Au islands is via Ostwald ripening, which includes these following steps: the detachment of Au adatoms from smaller clusters, the immediate formation of dimers and their fast diffusion on the surface, and the agglomeration of dimers onto the surface of larger clusters.

5.4 Conclusions

We have examined the energetics of Au_8 clusters in the fcc and ridge region of g/Ru(0001) by using GA-based DFT calculations. The most stable Au_8 structure and its energy in each of these two regions were reported and the diffusion barrier for the Au_8 cluster on the graphene moiré was estimated. The double-layer Au islands observed in the experiment [26] can be explained by the double-layer wall structure that Au_8 forms in the fcc region and the observation that nucleation of Au starts in the fcc region at low

coverage [20] which induces the double-layer structure formed over the moiré surface. This consistency provides us insight on the formation mechanism of Au double-layer film on g/Ru(0001). It supports our hypothesis that the sintering mode of Au clusters is Ostwald ripening and the vertical Au_2 species is the building block to form larger Au islands on g/Ru(0001) [24]. However, the kinetics of surface mass transport has not been taken into account and we lack a quantitative understanding of the cluster nucleation and growth mechanism. While the validation of our hypothesis of Au clustering mechanism remains an on-going subject of research, what we have known about cluster formation on g/Ru(0001) and other supported graphene surfaces shows that graphene moiré has the potential of being a suitable template for the rational design of metal cluster superlattices.

5.5 References

[1] B. Hvolbaek, T.V.W. Janssens, B.S. Clausen, H. Falsig, C.H. Christensen, J.K. Norskov, Nano Today, 2 (2007) 14-18.

[2] A. Sanchez, S. Abbet, U. Heiz, W.D. Schneider, H. Hakkinen, R.N. Barnett, U. Landman, J. Phys. Chem. A, 103 (1999) 9573-9578.

[3] G.C. Bond, D.T. Thompson, Catal. Rev.-Sci. Eng., 41 (1999) 319-388.

[4] M. Haruta, N. Yamada, T. Kobayashi, S. Iijima, J. Catal., 115 (1989) 301-309.

[5] M. Valden, X. Lai, D.W. Goodman, Science, 281 (1998) 1647-1650.

[6] M.S. Chen, D.W. Goodman, Science, 306 (2004) 252-255.

[7] M.M. Schubert, V. Plzak, J. Garche, R.J. Behm, Catal. Lett., 76 (2001) 143-150.

[8] S. Schimpf, M. Lucas, C. Mohr, U. Rodemerck, A. Bruckner, J. Radnik, H. Hofmeister, P. Claus, Catal. Today, 72 (2002) 63-78.

[9] M.A.P. Dekkers, M.J. Lippits, B.E. Nieuwenhuys, Catal. Today, 54 (1999) 381-390.

[10] A.C. Gluhoi, M.A.P. Dekkers, B.E. Nieuwenhuys, J. Catal., 219 (2003) 197-205.

[11] M. Okumura, Y. Kitagawa, K. Yamagcuhi, T. Akita, S. Tsubota, M. Haruta, Chem. Lett., 32 (2003) 822-823.

[12] B.S. Uphade, M. Okumura, S. Tsubota, M. Haruta, Appl. Catal. A-Gen., 190 (2000) 43-50.

[13] P. Landon, P.J. Collier, A.J. Papworth, C.J. Kiely, G.J. Hutchings, Chem. Commun., (2002) 2058-2059.

[14] R. Burch, Phys. Chem. Chem. Phys., 8 (2006) 5483-5500.

[15] H. Sakurai, T. Akita, S. Tsubota, M. Kiuchi, M. Haruta, Appl. Catal. A-Gen., 291 (2005) 179-187.

[16] M.M. Schubert, S. Hackenberg, A.C. van Veen, M. Muhler, V. Plzak, R.J. Behm, J. Catal., 197 (2001) 113-122.

[17] I.X. Green, W.J. Tang, M. Neurock, J.T. Yates, Science, 333 (2011) 736-739.

[18] P.J. Feibelman, Phys. Rev. B, 77 (2008) 165419.

[19] A.T. N'Diaye, S. Bleikamp, P.J. Feibelman, T. Michely, Phys. Rev. Lett., 97 (2006) 215501.

[20] Z.H. Zhou, F. Gao, D.W. Goodman, Surf. Sci., 604 (2010) L31-L38.

[21] A.T. N'Diaye, J. Coraux, T.N. Plasa, C. Busse, T. Michely, New J. Phys., 10 (2008) 043033.

[22] K. Donner, P. Jakob, J. Chem. Phys., 131 (2009) 164701.

[23] L. Semidey-Flecha, D. Teng, B.F. Habenicht, D.S. Sholl, Y. Xu, J. Chem. Phys., 138 (2013) 184710.

[24] D. Teng, D.S. Sholl, Surf. Sci. (in press), (2014).

[25] B.F. Habenicht, D. Teng, L. Semidey-Flecha, D.S. Sholl, Y. Xu, Top. Catal., 57 (2014) 69-79.

[26] L. Liu, Z.H. Zhou, Q.L. Guo, Z. Yan, Y.X. Yao, D.W. Goodman, Surf. Sci., 605 (2011) L47-L50.

[27] L.B. Vilhelmsen, B. Hammer, Phys. Rev. Lett., 108 (2012) 126101.

[28] L.B. Vilhelmsen, K.S. Walton, D.S. Sholl, J. Am. Chem. Soc., 134 (2012) 12807-12816.

[29] L.B. Vilhelmsen, D.S. Sholl, J. Phys. Chem. Lett., 3 (2012) 3702-3706.

[30] D.M. Deaven, K.M. Ho, Phys. Rev. Lett., 75 (1995) 288-291.

[31] J. Enkovaara, C. Rostgaard, J.J. Mortensen, J. Chen, M. Dulak, L. Ferrighi, J. Gavnholt, C. Glinsvad, V. Haikola, H.A. Hansen, H.H. Kristoffersen, M. Kuisma, A.H. Larsen, L. Lehtovaara, M. Ljungberg, O. Lopez-Acevedo, P.G. Moses, J. Ojanen, T. Olsen, V. Petzold, N.A. Romero, J. Stausholm-Moller, M. Strange, G.A. Tritsaris, M. Vanin, M. Walter, B. Hammer, H. Hakkinen, G.K.H. Madsen, R.M. Nieminen, J. Norskov, M. Puska, T.T. Rantala, J. Schiotz, K.S. Thygesen, K.W. Jacobsen, J. Phys.-Condens. Matter, 22 (2010) 253202.

[32] J.J. Mortensen, L.B. Hansen, K.W. Jacobsen, Phys. Rev. B, 71 (2005) 035109.

[33] G. Kresse, J. Furthmuller, Comp. Mater. Sci., 6 (1996) 15-50.

[34] G. Kresse, J. Furthmuller, Phys. Rev. B, 54 (1996) 11169-11186.

[35] G. Kresse, J. Hafner, Phys. Rev. B, 47 (1993) 558-561.

[36] G. Kresse, J. Hafner, Phys. Rev. B, 49 (1994) 14251-14269.

[37] G. Kresse, D. Joubert, Phys. Rev. B, 59 (1999) 1758-1775.

[38] P.E. Blochl, Phys. Rev. B, 50 (1994) 17953-17979.

[39] D.S. Sholl, J.A. Steckel, Density functional theory: a practical introduction, Wiley, Hoboken, N.J., 2009.

[40] J.P. Perdew, K. Burke, M. Ernzerhof, Phys. Rev. Lett., 77 (1996) 3865-3868.

[41] J.P. Perdew, K. Burke, M. Ernzerhof, Phys. Rev. Lett., 78 (1997) 1396-1396.

[42] M. Methfessel, A.T. Paxton, Phys. Rev. B, 40 (1989) 3616-3621.

[43] D.E. Jiang, M.H. Du, S. Dai, J. Chem. Phys., 130 (2009) 074705.

[44] B. Wang, M.L. Bocquet, S. Marchini, S. Gunther, J. Wintterlin, Phys. Chem. Chem. Phys., 10 (2008) 3530-3534.

[45] K.T. Chan, J.B. Neaton, M.L. Cohen, Phys. Rev. B, 77 (2008) 235430.

[46] L.B. Hu, X.R. Hu, X.B. Wu, C.L. Du, Y.C. Dai, J.B. Deng, Phys. B-Condens. Matter, 405 (2010) 3337-3341.

[47] B. Assadollahzadeh, P. Schwerdtfeger, J. Chem. Phys., 131 (2009) 064306.

[48] R.F.W. Bader, P.J. Macdougall, C.D.H. Lau, J. Am. Chem. Soc., 106 (1984) 1594-1605.

[49] T.A. Manz, D.S. Sholl, J. Chem. Theory Comput., 6 (2010) 2455-2468.

[50] T.A. Manz, D.S. Sholl, J. Chem. Theory Comput., 8 (2012) 2844-2867.

[51] G. Henkelman, A. Arnaldsson, H. Jonsson, Comp. Mater. Sci., 36 (2006) 354-360.

[52] W. Tang, E. Sanville, G. Henkelman, J. Phys.-Condens. Matter, 21 (2009) 084204.

[53] D. Spisak, http://homepage.univie.ac.at/daniel.spisak/.

[54] L. Ratke, P.W. Voorhees, Growth and Coarsening: Ostwald Ripening in Material Processing, Springer, Berlin, 2002.

CHAPTER 6

CU CLUSTERS ON GRAPHENE/CU(111)

6.1 Introduction

In previous Chapters, we have used DFT calculations to investigate small Rh and Au clusters on g/Ru(0001). Rh and Au show distinct behaviors on g/Ru(0001) in experiments [1]. In an effort to understand the behavior of larger clusters on g/Ru(0001), we combined genetic algorithm with DFT calculations for a Au_8 cluster. We predicted the most stable cluster configuration of Au_8 on g/Ru(0001) and estimated its diffusion barrier over the surface. These results give us insight into the mechanisms of cluster formation on g/Ru(0001), but they are not sufficient to help us understand all aspects of cluster nucleation and growth. It is thus necessary to focus on even larger clusters (>10 atoms) on supported graphene and seek suitable methods to describe and simulate this type of systems.

Our previous studies of metal clusters on g/Ru(0001) were all performed using DFT calculations, which generally provide high accuracy for material properties. However, because of the large computational cost, DFT methods are limited to relatively small system sizes, typically a few hundred atoms. Because of the limitation in time and length scale that DFT method can describe, it is thus not able to address many important issues associated with large and complex microstructures. Classical molecular simulations, such as molecular dynamics (MD) and Monte Carlo, has been employed to examine systems with time and length scales that are beyond the reach of DFT methods

[2]. The advantage of these methods is their high computational speed and their ability to probe large systems at finite temperatures and under external driving forces.

The key component in classical molecular simulations is the inter-atomic potential, which describes the bonding and non-bonding effects of valence electrons without explicitly describing the electrons themselves. It has not generally possible for empirical inter-atomic potentials to describe structures with more than one bonding type, because empirical potentials for different bonding types have different functional forms. The charge optimized many-body (COMB) potential [3-5] is one of several reactive force fields that can describe complex bonding environments in real materials. Another widely used potential of this kind is the reactive force field (ReaxFF) [6]. Both COMB and ReaxFF describe reactive processes by allowing bond formation and bond breaking during classical simulations. The force field parameters used in these inter-atomic potentials are optimized relative to DFT and/or other quantum chemical calculations and/or reported experimental values in literature. Molecular simulations using COMB or ReaxFF are slower than using non-reactive force fields, but are still significantly faster than DFT calculations [7-11].

The development of COMB potentials has gone through three major stages, denoted COMB1, COMB2, and COMB3, respectively. Each generation has made a significant improvement over the previous one. In particular, several functions in COMB3 have been refined in the aim of providing a general, flexible, and robust empirical potential formalism that is capable of treating all different types of bonds within a multi-component system in an integrated manner [3]. COMB1 has been successfully applied to reproduce the phase order of SiO_2 [5] and Cu [12]. COMB2 has

been applied to Si-SiO_2 system and amorphous SiO_2 [4], the Cu-SiO_2 [13], Hf-HfO_2 [14], and Cu-Cu_2O [15] systems, and Cu adatoms on ZnO surfaces [16]. COMB3 was recently proposed and demonstrated to be able to describe organic-metal interaction in a dynamically changing environment [3]. All three generations of COMB have been implemented into the Large-scale Atomic/Molecular Massively Parallel Simulator (LAMMPS) program [17, 18].

A strong limitation of the COMB potential to date is that it has only been developed for a limited set of elements including C, H, O, Cu, Al, Zr, Zn, and Ti. As a result, it is not currently possible to study Rh or Au on supported graphene with COMB potential. To work within this limitation, we aim to investigate large Cu clusters on graphene supported by Cu(111) (denoted as g/Cu(111)). Epitaxial graphene has been grown on Cu(111) and it has been observed experimentally by scanning tunneling microscopy and spectroscopy [19-22]. Multiple moiré patterns were observed, which is a result of different rotational alignments of the graphene lattice with the underlying Cu(111) lattice. This indicates that the graphene is weakly coupled to the substrate. There are two predominant moiré patterns observed, which suggests that graphene has preferred orientation with the underlying Cu(111). We will only simulate the large moiré pattern (~6.6 nm [21], ~6.0 nm [20] periodicity) when the graphene lattice is aligned with Cu(111) lattice with 0° rotation. Computational studies of graphene on transition metal surfaces [23, 24] using DFT calculations with van der Waals density functional (vdW-DF) predict that the lattice mismatch between graphene and Cu(111) is small (4.44%) and the binding is weak. It was also reported that the potential energy surface (PES) of graphene on Cu(111) is similar to that on Ru(0001), only with less corrugation [23]. This

suggests that the fcc region of g/Cu(111) is the strongest adsorption region, which is the same as the case of g/Ru(0001). Cu adatoms have been theoretically studied on graphene using vdW-DF and PBE+D2 methods [25], but unfortunately, there is no prior literature reporting Cu clusters on g/Cu(111) experimentally or computationally.

Our goal in this Chapter is to predict the morphology of Cu clusters on g/Cu(111) and investigate their mobility at elevated temperatures using MD simulations with the COMB3 potential. We focus our study on Cu_{19}, a magic size cluster. A few other clusters with different sizes were considered for the study of cluster mobility at different temperatures with respect to cluster size.

6.2 Methods

We performed MD simulations using LAMMPS program with the COMB3 potential describing the atomic interactions. The general form of COMB is $U^{tot}[\{q\},\{r\}] = U^{es}[\{q\},\{r\}] + U^{short}[\{q\},\{r\}] + U^{vdW}[\{r\}] + U^{corr}[\{r\}]$. As shown, the total potential energy $U^{tot}[\{q\},\{r\}]$ of a system in COMB3 is composed of the electrostatic energies $U^{es}[\{q\},\{r\}]$, short-range interactions $U^{short}[\{q\},\{r\}]$, van der Waals interactions $U^{vdW}[\{r\}]$, and correction terms $U^{corr}[\{r\}]$, where $\{q\}$ and $\{r\}$ represent the charge array and coordinate array of the system, respectively. The detailed functional form of each term and the parameterization procedure of COMB3 can be found in Reference [3].

All MD simulations were performed using the LAMMPS software in NVT ensemble and the temperature was kept constant using the Nose-Hoover thermostat [26, 27]. The equations of motion used are those of Shinoda *et al.* [28] and the time integration schemes follow the time-reversible measure-preserving Verlet and rRESPA integrators derived by Tuckerman *et al.* [29].

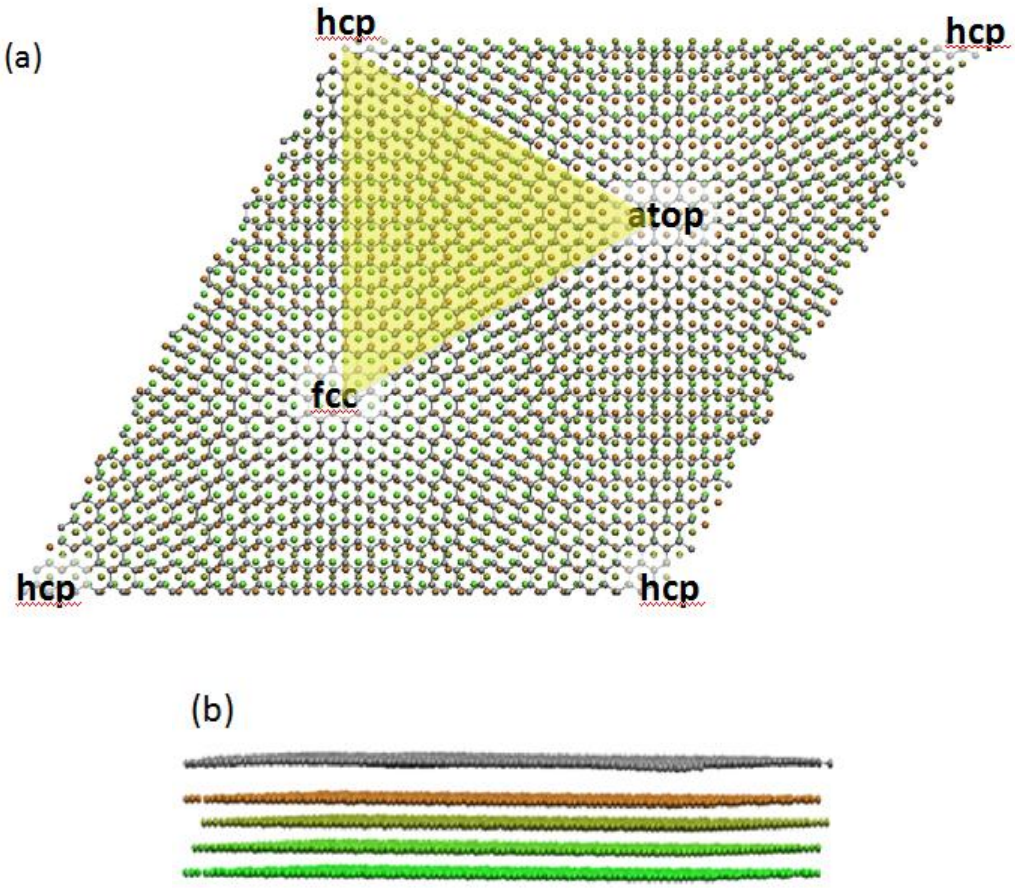

Figure 6.1: The simulated relaxed structure of (26×26) graphene (grey)/(25×25) Cu(111) (green, yellow, orange) unit cell obtained from NVT-MD simulation at 0 K. Cu atoms of different layers are colored differently. (a) Top view of the unit cell with the fcc, hcp, and atop regions labeled; The highlighted yellow triangular area is the symmetry-irreducible zone. (b) Side view of the unit cell.

The g/Cu(111) surface was modeled as a (26×26)-graphene layer over a (25×25)-Cu(111) slab of 4 Cu layers with a total of 2500 Cu atoms and 1352 C atoms. Experimental values of lattice constant for graphene (2.46 Å) [30, 31] and copper (3.61 Å) [21, 32] were used to construct the g/Cu(111) surface. The simulation box of g/Cu(111) surface is hexagonal and has a dimension of 63.82×63.82×90.00 Å. The bottom two layers of Cu(111) were kept rigid during all simulations and periodic

boundary conditions were applied in all three directions. The graphene layer was initially placed at 3 Å above the Cu(111) surface and was allowed to relax in the NVT ensemble at ~0 K. The resulting structure of g/Cu(111) is shown in Figure 6.1 with different regions labeled. The definition of each region (atop, fcc, hcp) is similar to that of g/Ru(0001) in Chapter 2 and there is no clear boundary between regions.

Candidate Cu_{19} 3D cluster structures were generated by performing an NVT-MD simulation of Cu_{19} in gas phase at 900 K for 500 ps with a time step of 20 fs. The complex potential energy surface can be explored in this manner and the use of large time steps in conjunction with a high-temperature simulation allows a rapid generation of an approximate trajectory that is able to overcome energy barriers between local energy minima. The dimension of the simulation box was 50×50×50 Å and periodic boundary conditions were applied in all three directions. The initial Cu_{19} cluster is roughly spherical and has O_h symmetry, generated as a 19-atom fragment from the Cu bulk fcc crystal structure. From the MD trajectory, 6 low energy configurations of Cu_{19} 3D clusters were picked and further optimized by running energy minimization using a Hessian-free truncated Newton algorithm (hftn) [33] with the force tolerance of 0.01 eV/Å. The 2D Cu_{19} cluster we studied is a hexagon, with all inner angles equal to approximately 120 °.

Each of the relaxed Cu_{19} clusters was initially placed 3 Å above the fcc region of g/Cu(111). The cluster was displaced so that its center of mass was roughly in the center of the fcc region. Except for the bottom 2 layers of Cu(111), all other atoms were allowed to relax. An NVT-MD simulation was performed for the system at ~0 K. The velocity of the system was initialized at zero to approximate the target temperature of 0

K. A time step of 1 fs was used and the simulation was run for 100 ps until the potential energy converged. This time step was chosen so that our MD simulations can yield meaningful results in a reasonable computational speed. The adsorption energy of a Cu_{19} cluster on g/Cu(111) is given by $E_{ads} = E_{Cu19\_gCu(111)} - E_{gCu(111)} - E_{Cu19\_gas}$. $E_{Cu19\_gCu(111)}$ and $E_{gCu(111)}$ are the potential energies of g/Cu(111) with and without Cu_{19} adsorbed on it, respectively. E_{Cu19_gas} is the potential energy of Cu_{19} in gas phase. The adsorption energy of a Cu monolayer on g/Cu(111) was also calculated for reference.

To study the Cu cluster mobility on g/Cu(111), we need to calculate the diffusion coefficient. The diffusion coefficient D of a Cu cluster on g/Cu(111) can be obtained from measuring the two-dimensional mean squared displacement (MSD) of the cluster during the MD simulations. The MSD is expressed as MSD = $<|\mathbf{r}(t) - \mathbf{r}(0)|^2>$. Using Einstein's equation in two dimensions, $4Dt$ = MSD, diffusivity D can be calculated from the slope of the MSD versus time [2, 34]. Only 2D clusters were considered and eight different cluster sizes (size = 4, 6, 7, 8, 16, 18, 19, and 20 atoms) were studied. Among them, Cu_7 and Cu_{19} are magic-size clusters. An NVT-MD simulation was performed for each cluster size and a time step of 1 fs was used. The MSD of Cu cluster was recorded every 1000 MD steps. The system was first relaxed at ~0 K for 100 ps and then heated to a higher temperature for 300 ps. Four temperatures (200, 300, 400, and 500 K) were investigated. At each temperature, 10 independent MD runs were performed to get an averaged MSD. The representative MD trajectories of Cu clusters on g/Cu(111) at different temperatures were generated and the Cu cluster structures along the trajectory were shown inside the plots.

6.3 Results and Discussion

6.3.1 Candidate Cu_{19} structures

The structures of the 6 lowest energy 3D Cu_{19} clusters in the gas phase are shown in Figure 6.2a and a 2D hexagonal Cu_{19} cluster is shown for comparison in Figure 6.2b. Their potential energies after relaxation are tabulated in Table 6.1.

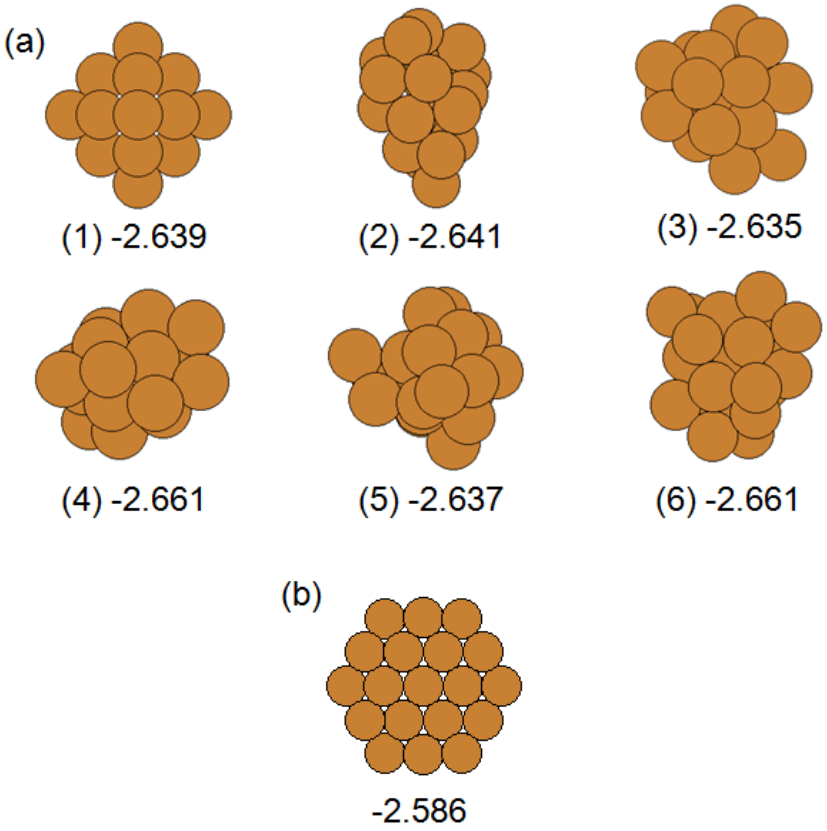

Figure 6.2: (a) The structures of the 6 lowest energy Cu_{19} 3D clusters with their potential energies reported in eV/atom. (b) The structure of the Cu_{19} 2D cluster and its potential energy in eV/atom.

Intuitively, it may seem that the cluster with O_h symmetry would have the lowest potential energy and thus be the preferred structure for 19 Cu atoms, but our simulation results indicate that this is not so. As shown in Table 6.1, this cluster is 0.0223 eV/atom (0.42 eV total) higher in energy than the lowest energy configuration we found. These seven clusters were used as candidate Cu_{19} structures and were placed in the fcc region of g/Cu(111) for the study of their adsorption on the surface.

Table 6.1: The potential energies (PE) (in eV/atom and eV) of 6 low energy 3D Cu_{19} clusters and the 2D Cu_{19} magic cluster. The 3D clusters are numbered as they are shown in Figure 6.2.

Cu_{19} Structure	PE (eV/atom)	PE (eV)
3D_(1)	-2.6389	-50.14
3D_(2)	-2.6408	-50.18
3D_(3)	-2.6347	-50.06
3D_(4)	-2.6612	-50.56
3D_(5)	-2.6369	-50.10
3D_(6)	-2.6605	-50.55
2D	-2.5855	-49.12

6.3.2 Adsorption of Cu_{19} on g/Cu(111)

We first performed an NVT-MD simulation for bare g/Cu(111) surface at ~0 K. The resulting potential energy is −4.7843 eV/atom and the graphene corrugation predicted is 0.614 Å, which is in good agreement with experimental value of 0.35 ± 0.1 Å [20] and a previous MD simulation result of 0.45 Å using a fitted Tersoff potential [35].

The seven candidate Cu_{19} clusters we generated in Section 6.3.1 were placed in the fcc region of g/Cu(111) and the adsorption energy of each cluster was calculated and reported in Table 6.2. The reference state is the sum of potential energy for bare g/Cu(111) surface and the lowest-energy 3D Cu_{19} cluster in vacuum.

Table 6.2: The adsorption energies (in eV/atom) of 6 low energy 3D Cu_{19} clusters and the 2D Cu_{19} magic cluster in the fcc region of g/Cu(111). The 3D clusters are numbered as they are shown in Figure 6.2.

Cu_{19} Structure	E_{ads} (eV/atom)
3D_(1)	-0.1042
3D_(2)	-0.0938
3D_(3)	-0.0691
3D_(4)	-0.1182
3D_(5)	-0.0789
3D_(6)	-0.1036
2D	-0.0938

As shown in Table 6.2, one of the 3D Cu_{19} clusters (3D_(4)) has the lowest adsorption energy compared to other Cu_{19} clusters. This Cu_{19} cluster is 0.024 eV/atom (0.46 eV total) lower in energy than the 2D Cu19 cluster on g/Cu(111). This indicates that at very low temperature, a Cu_{19} cluster prefers a 3D compact structure in the fcc region of g/Cu(111). It thus implies that different from 2D Au islands formed on g/Ru(0001) [1, 36, 37], 3D Cu aggregates would form on g/Cu(111) at low temperature. As the temperature increases, the system tends to progress towards maximizing its

entropy, in which a more disordered state is preferred. Thus the diffusion and subsequent agglomeration of these 3D Cu_{19} clusters may occur at higher temperatures.

6.3.3 Mobility of Cu clusters on g/Cu(111)

We studied the mobility of a Cu cluster on g/Cu(111) by measuring its mean square displacement (MSD) during the NVT-MD simulation. We simulated eight different cluster sizes (n = 4, 6, 7, 8, 16, 18, 19, and 20 atoms) at four different temperatures (T = 200, 300, 400, and 500 K). The initial structures of these Cu clusters are 2D clusters. Before heating up the system, the Cu clusters were relaxed on g/Cu(111) at 0 K and their adsorption energies were calculated and tabulated in Table 6.3. The results show that large Cu clusters ($n \geq 16$) are more strongly adsorbed on g/Cu(111) than small Cu clusters ($n \leq 8$) at 0 K. However, on average each atom in small Cu clusters is 0.06 eV more strongly adsorbed than that in large Cu clusters.

Table 6.3: The adsorption energies (in eV/atom and eV) of 2D Cu clusters on g/Cu(111) at 0 K.

Cluster Size	E_{ads} (eV/atom)	E_{ads} (eV)
4	-0.2594	-1.038
6	-0.2235	-1.341
7	-0.2153	-1.507
8	-0.2070	-1.656
16	-0.1682	-2.691
18	-0.1723	-3.101
19	-0.1695	-3.221
20	-0.1636	-3.272

Some representative trajectories of a Cu cluster on g/Cu(111) at 200 K and 500 K are shown in Figures 6.3, 6.4, 6.5, 6.6 for Cu_7, Cu_8, Cu_{19}, Cu_{20}, respectively. The structures of the Cu cluster along the trajectory are shown inside the plots. For reference in these figures, the fcc to fcc distance on the g/Cu(111) moiré is 63.82 Å.

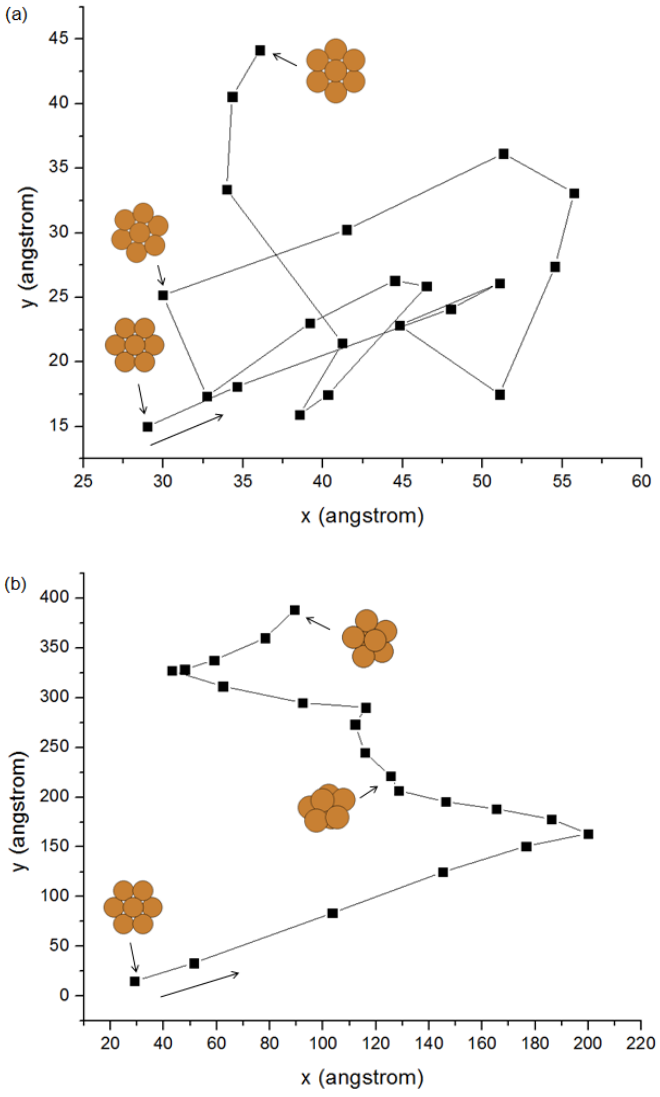

Figure 6.3: Sample trajectory of a Cu_7 cluster on g/Cu(111) simulated at (a) 200 K and (b) 500 K. The simulation time span is 200 ps and the time between two neighboring points is 10 ps. The structures of Cu_7 along the trajectory are shown in the plot.

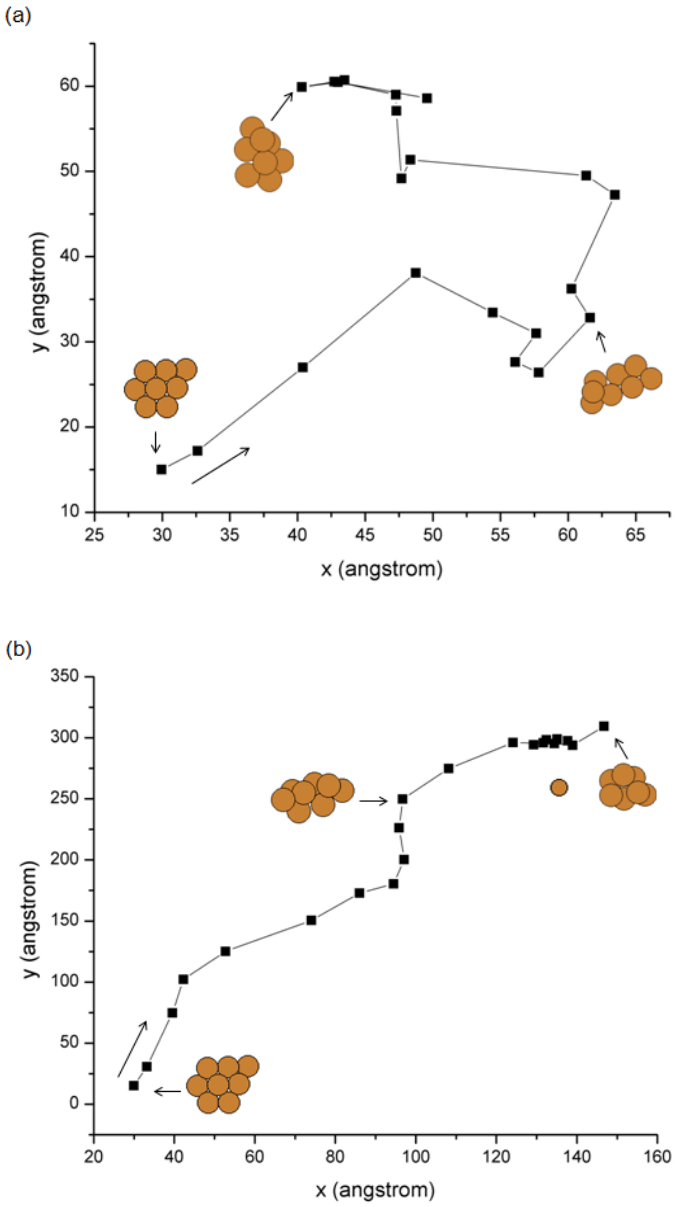

Figure 6.4: Sample trajectory of a Cu_8 cluster on g/Cu(111) simulated at (a) 200 K and (b) 500 K. The simulation time span is 200 ps and the time between two neighboring points is 10 ps. The structures of Cu_8 along the trajectory are shown in the plot.

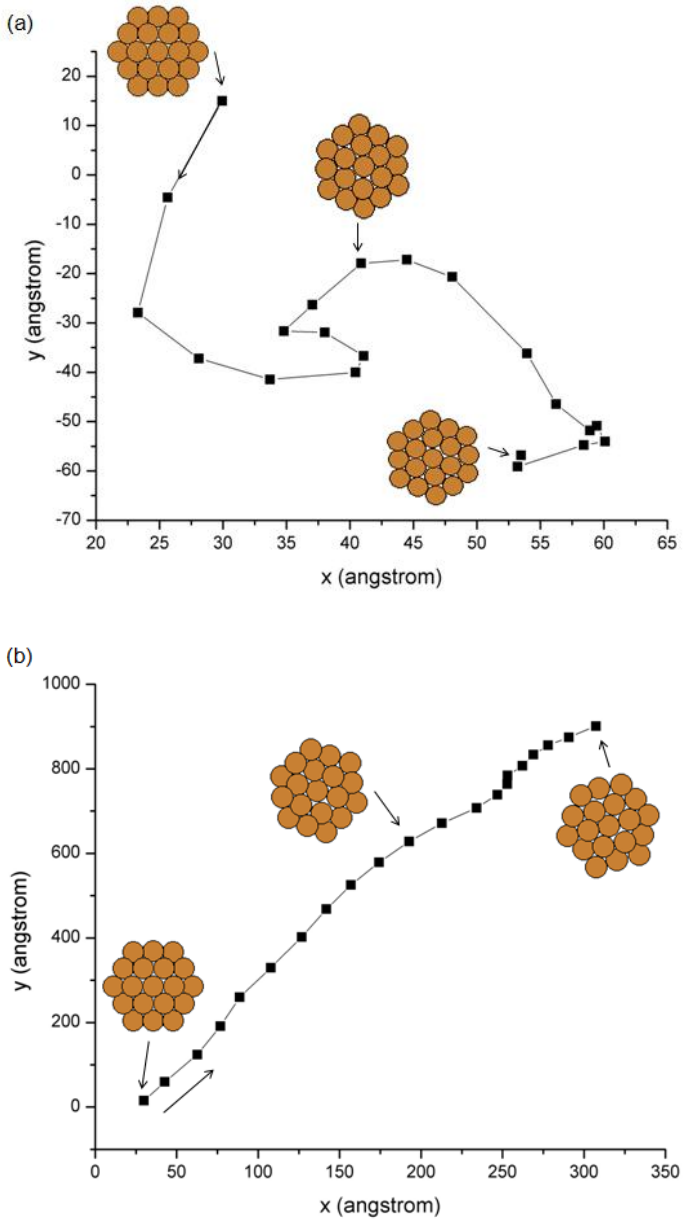

Figure 6.5: Sample trajectory of a Cu_{19} cluster on g/Cu(111) simulated at (a) 200 K and (b) 500 K. The simulation time span is 200 ps and the time between two neighboring points is 10 ps. The structures of Cu_{19} along the trajectory are shown in the plot.

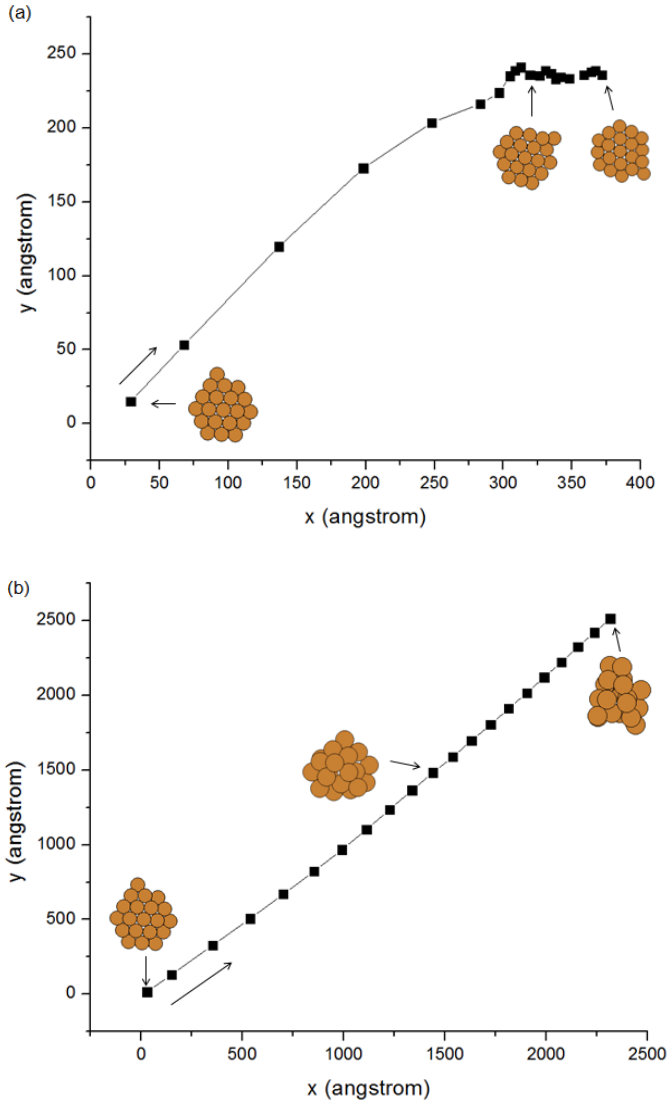

Figure 6.6: Sample trajectory of a Cu_{20} cluster on g/Cu(111) simulated at (a) 200 K and (b) 500 K. The simulation time span is 200 ps and the time between two neighboring points is 10 ps. The structures of Cu_{20} along the trajectory are shown in the plot.

A representative plot of 10 different MD trajectories of a Cu_{19} cluster on g/Cu(111) at 400 K is shown in Figure 6.7a. The cluster's MSD can be calculated by averaging these 10 trajectories. An example plot of MSD versus time for Cu_{16} on g/Cu(111) at different temperatures is shown in Figure 6.7b. It is clear that the MSD is

nearly linear relative to time and higher temperature leads to higher diffusivity of Cu clusters.

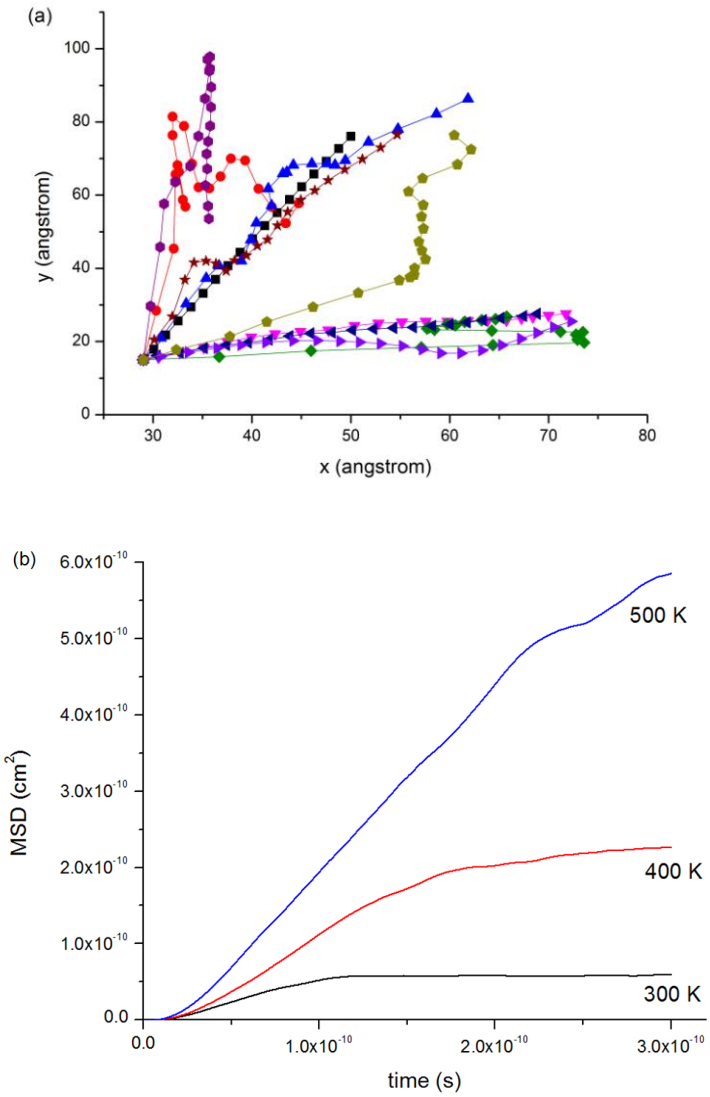

Figure 6.7: (a) 10 different MD trajectories of a Cu_{19} cluster on g/Cu(111) simulated at 400 K. The simulation time span is 20 ps and each color represents a different trajectory. (b) MSD (in cm^2) of Cu_{16} supported on g/Cu(111) at 300, 400, and 500 K as a function of time (in s). The total simulation time is 300 ps.

It was noted from the trajectories and the MSD plot that within the time span of simulation, all Cu clusters diffuse very fast and are almost "sliding" on g/Cu(111) at elevated temperatures. Especially at higher temperatures (i.e. 500 K), our data implies there are negligible energy barriers imposed on supported Cu clusters by the corrugation of g/Cu(111). As mentioned in Chapters 1 and 2, the greatly enhanced adsorption of supported clusters in the fcc and hcp regions of g/Ru(0001) is caused by a large lattice mismatch (10.8%) between graphene and Ru(0001) and a strong carbon sp^3 rehybridization. However, the lattice mismatch between graphene and Cu(111) is 3.6%, resulting in a large (26×26)-g/Cu(111) unit cell. Graphene was also demonstrated of undergoing a weak rehybridization on Cu(111) [24]. These factors explain the weak interactions and little barriers that g/Cu(111) imposes to Cu clusters. Thus, at temperatures around room temperature and above, the corrugation experienced by Cu clusters is almost negligible.

Our results indicate that Cu clusters will rapidly agglomerate on this surface and form large Cu islands. We have not found a Cu cluster size above which the Cu clusters diffuse via Brownian motion on g/Cu(111) at elevated temperatures. This cluster size is likely to exist, but if it does it is much larger than clusters we have examined. Our simulation results suggest that g/Cu(111) may not be an ideal substrate for the formation and growth of isolated Cu clusters.

6.4 Conclusions

We have examined the morphology of Cu clusters on g/Cu(111) by investigating the adsorption of a Cu_{19} cluster in the fcc region of g/Cu(111) using MD simulations with the COMB3 potential. COMB3 is an empirical potential that can capture charge transfer

and describe complex bonding environment in real materials. All MD simulations were performed using the LAMMPS program. We determined the low energy Cu_{19} structures and their adsorption energies at 0 K on g/Cu(111). At low temperature, a Cu_{19} cluster prefers to form a 3D compact structure on g/Cu(111). We also studied the mobility of Cu clusters on g/Cu(111) by performing NVT-MD simulations at elevated temperatures. The analysis shows that the small corrugation of g/Cu(111) imposes weak interaction on the supported Cu clusters, which suggests that g/Cu(111) may not be a suitable substrate for the formation and growth of isolated Cu clusters.

6.5 References

[1] Z.H. Zhou, F. Gao, D.W. Goodman, Surf. Sci., 604 (2010) L31-L38.

[2] D. Frenkel, B. Smit, Understanding molecular simulation: from algorithms to applications, Academic, 2nd ed., San Diego, C.A., 2002.

[3] T. Liang, B. Devine, S.R. Phillpot, S.B. Sinnott, J. Phys. Chem. A, 116 (2012) 7976-7991.

[4] T.R. Shan, B.D. Devine, J.M. Hawkins, A. Asthagiri, S.R. Phillpot, S.B. Sinnott, Phys. Rev. B, 82 (2010) 235302.

[5] J.G. Yu, S.B. Sinnott, S.R. Phillpot, Phys. Rev. B, 75 (2007) 085311.

[6] A.C.T. van Duin, S. Dasgupta, F. Lorant, W.A. Goddard, J. Phys. Chem. A, 105 (2001) 9396-9409.

[7] H.P. Chen, R.K. Kalia, E. Kaxiras, G. Lu, A. Nakano, K. Nomura, A.C.T. van Duin, P. Vashishta, Z.S. Yuan, Phys. Rev. Lett., 104 (2010) 155502.

[8] A. Nakano, R.K. Kalia, K. Nomura, A. Sharma, P. Vashishta, F. Shimojo, A.C.T. van Duin, W.A. Goddard, R. Biswas, D. Srivastava, Comp. Mater. Sci., 38 (2007) 642-652.

[9] K.I. Nomura, R.K. Kalia, A. Nakano, P. Vashishta, A.C.T. van Duin, W.A. Goddard, Phys. Rev. Lett., 99 (2007) 148303.

[10] Y.K. Shin, T.R. Shan, T. Liang, M.J. Noordhoek, S.B. Sinnott, A.C.T. van Duin, S.R. Phillpot, MRS Bull., 37 (2012) 504-512.

[11] S.V. Zybin, W.A. Goddard, P. Xu, A.C.T. van Duin, A.P. Thompson, Appl. Phys. Lett., 96 (2010) 081918.

[12] J. Yu, S.B. Sinnott, S.R. Phillpot, Philos. Mag. Lett., 89 (2009) 136-144.

[13] T.R. Shan, B.D. Devine, S.R. Phillpot, S.B. Sinnott, Phys. Rev. B, 83 (2011) 115327.

[14] T.R. Shan, B.D. Devine, T.W. Kemper, S.B. Sinnott, S.R. Phillpot, Phys. Rev. B, 81 (2010) 125328.

[15] B. Devine, T.R. Shan, Y.T. Cheng, A.J.H. McGaughey, M. Lee, S.R. Phillpot, S.B. Sinnott, Phys. Rev. B, 84 (2011) 125308.

[16] Y.T. Cheng, T.R. Shan, B. Devine, D. Lee, T. Liang, B.B. Hinojosa, S.R. Phillpot, A. Asthagiri, S.B. Sinnott, Surf. Sci., 606 (2012) 1280-1288.

[17] S. Plimpton, J. Comput. Phys., 117 (1995) 1-19.

[18] LAMMPS, LAMMPS molecular dynamics package; http://lammps.sandia.gov.

[19] Y. Ogawa, B.S. Hu, C.M. Orofeo, M. Tsuji, K. Ikeda, S. Mizuno, H. Hibino, H. Ago, J. Phys. Chem. Lett., 3 (2012) 219-226.

[20] L. Zhao, K.T. Rim, H. Zhou, R. He, T.F. Heinz, A. Pinczuk, G.W. Flynn, A.N. Pasupathy, Solid State Commun., 151 (2011) 509-513.

[21] L. Gao, J.R. Guest, N.P. Guisinger, Nano Lett., 10 (2010) 3512-3516.

[22] W. Kim, K. Yoo, E.K. Seo, S.J. Kim, C. Hwang, J. Korean Phys. Soc., 59 (2011) 71-74.

[23] K. Toyoda, K. Nozawa, N. Matsukawa, S. Yoshii, J. Phys. Chem. C, 117 (2013) 8156-8160.

[24] M. Vanin, J.J. Mortensen, A.K. Kelkkanen, J.M. Garcia-Lastra, K.S. Thygesen, K.W. Jacobsen, Phys. Rev. B, 81 (2010) 081408.

[25] M. Amft, S. Lebegue, O. Eriksson, N.V. Skorodumova, J. Phys.-Condens. Matter, 23 (2011) 395001.

[26] W.G. Hoover, Phys. Rev. A, 31 (1985) 1695-1697.

[27] S. Nose, J. Chem. Phys., 81 (1984) 511-519.

[28] W. Shinoda, M. Shiga, M. Mikami, Phys. Rev. B, 69 (2004) 134103.

[29] M.E. Tuckerman, J. Alejandre, R. Lopez-Rendon, A.L. Jochim, G.J. Martyna, J. Phys. A-Math. Gen., 39 (2006) 5629-5651.

[30] B. Wang, M.L. Bocquet, S. Marchini, S. Gunther, J. Wintterlin, Phys. Chem. Chem. Phys., 10 (2008) 3530-3534.

[31] D.E. Jiang, M.H. Du, S. Dai, J. Chem. Phys., 130 (2009) 074705.

[32] P.A. Khomyakov, G. Giovannetti, P.C. Rusu, G. Brocks, J. van den Brink, P.J. Kelly, Phys. Rev. B, 79 (2009) 195425.

[33] S.G. Nash, J. Comput. Appl. Math., 124 (2000) 45-59.

[34] A. Einstein, Ann. Phys.-Berlin, 17 (1905) 549-560.

[35] P. Sule, M. Szendro, C. Hwang, L. Tapaszto, arXiv: 1401.1716 [cond-mat.mtrl-sci] 8 Jan 2014.

[36] L. Liu, Z.H. Zhou, Q.L. Guo, Z. Yan, Y.X. Yao, D.W. Goodman, Surf. Sci., 605 (2011) L47-L50.

[37] Y. Xu, L. Semidey-Flecha, L. Liu, Z.H. Zhou, D.W. Goodman, Faraday Discuss., 152 (2011) 267-276.

CHAPTER 7

CONCLUSIONS AND OUTLOOK

7.1 Conclusions

Long-range moiré superstructures exist in graphene formed on a number of single crystal surfaces such as Ir(111) and Ru(0001). These superstructures can function as templates to drive the self-assembly of superlattices of metal clusters for model catalyst studies. In Chapter 2, an extensive set of periodic DFT calculations were performed to investigate the adsorption and diffusion of Rh and Au adatoms on the (12×12)-graphene moiré on (11×11)-Ru(0001). We analyzed the detailed potential energy surfaces (PESs) for Rh_1 and Au_1 on small (3×3) model surfaces representing high-symmetry regions on g/Ru(0001). The adsorption energy of each adatom in all 91 non-equivalent C-top and C_6 ring center sites in the symmetry-irreducible zone of the graphene moiré unit cell on g/Ru(0001) was calculated directly, yielding a coarse-grained PES. These PESs demonstrate that the global minimum-energy adsorption sites for both Rh_1 and Au_1 are located in the fcc region and the global maximum is located in the mound region. For both adatoms, the hcp region represents a shallower energy basin than the fcc region. All these predictions are consistent with the experimentally observed preferential nucleation in the fcc region by Rh and Au on g/Ru(0001). The lowest adsorption energy is –2.40 eV for Rh_1 and –1.57 eV for Au_1, both found in the fcc region.

The minimum-energy global diffusion path between fcc regions of adjacent moiré cells on g/Ru(0001) was determined for Au_1 and Rh_1. The global diffusion barriers are 0.53 eV for Rh_1 and 0.71 eV for Au_1, corresponding to a hopping rate between fcc

regions of adjacent moiré cells of 1.10×10^{3} and 9.97×10^{-1} s^{-1} at room temperature, respectively. The consequences of different mobility of adatoms to cluster nucleation and growth were explored by performing Monte Carlo-based statistical analysis. We demonstrated that even deposition coupled with a lack of transport across moiré cells is key to maximizing cluster number density and size uniformity, whereas significant transport across moiré cells leads to agglomeration and formation of large particles. However, experimentally Rh has been observed to form clusters at greater number density than Au on g/Ru(0001) [1]. The discrepancy between the experiment and the greater mobility of Rh_1 than Au_1 as predicted by theory suggests the need to take additional diffusing species, such as larger clusters, into account in understanding the nucleation and growth behavior of Au. Our work regarding this issue is presented in Chapter 4.

In Chapter 3, we performed periodic DFT calculations to investigate the adsorption and diffusion characteristics for all 18 4d (Y-Ag) and 5d (La-Au) metal adatoms on g/Ru(0001) using a series of (3×3) surface models representing the fcc, hcp, mound, and ridge regions of the graphene moiré. For all the adatoms, the global minimum-energy adsorption site is found in the fcc region and the global maximum in the mound region. This is consistent with previous experimental observations that nucleation occurred almost exclusively in the fcc region and never in the mound region [1-5]. For each series of the transition metals, those that have a half-filled or completely filled d shell have the weaker adsorption energies. By comparing the g/Ru(0001) surfaces with the freestanding graphene, it was seen that the Ru substrate enhances the adsorption of all 18 adatoms on graphene.

Diffusion within the fcc region is facile at room temperature for most adatoms (with the notable exception of Ta), but an additional barrier is imposed by the corrugation of the graphene moiré for traversing between moiré cells. Overall, the adatoms of the earlier transition metals have lower global mobility than those of the later ones, and the adatom of a 5d transition metal has lower global mobility than that of the corresponding 4d transition metal in the same group in the periodic table. We postulate that the maximum filling factor of the graphene moiré cells is achieved as a balance between nucleation density and diffusion length, both of which connect to the adsorption energy and the global mobility of the metal adatom on g/Ru(0001). Substrate temperature and coverage of metal atoms deposited will also influence nucleation density and diffusion length.

Motivated by the discussion following the statistical analysis in Chapter 2, we performed DFT calculations in Chapter 4 to examine the adsorption and diffusion of Rh and Au dimers and trimers on g/Ru(0001) and compared to our previous study of monomers. We have determined the lowest-energy structure, the diffusion barrier, and the room temperature hopping rate for Rh and Au dimers and trimers. All these small clusters were predicted to prefer adsorption in the fcc region of g/Ru(0001). The adsorption energy of a Rh_2 (Rh_3) in the fcc region is −2.85 (−3.53) eV, while for a Au_2 (Au_3) it is −0.99 (−1.64) eV. The diffusion barriers were determined by performing NEB calculations. The global diffusion barriers are 0.82 (1.50) eV for Rh_2 (Rh_3) and 0.51 (0.81) eV for Au_2 (Au_3), corresponding to a hopping rate between fcc regions of adjacent moiré cells of 1.05×10^{-3} (2.08×10^{-13}) s^{-1} for Rh_2 (Rh_3) and 6.77×10^{2} (6.17×10^{-3}) s^{-1} for Au_2 (Au_3) at room temperature, respectively. Our study show that Rh monomers diffuse

faster than dimers and trimers. For Au, however, dimers diffuse faster than monomers and trimers on the moiré surface. This difference in diffusion behaviors is directly associated with the cluster orientation with respect to the surface. We thus studied the orientation of dimers for all 4d and 5d transition metals on the surface. This analysis suggests that Re and Ag also form dimers that diffuse faster than monomers on the g/Ru(0001) surface, but that all other metals have diffusivities that decrease monotonically with cluster size.

In Chapter 5, we examined the energetics of Au_8 clusters in the fcc and ridge region of g/Ru(0001) by using a method combining Genetic Algorithm with DFT calculations. The most stable Au_8 structure and its energy in each of these two regions were reported and the diffusion barrier for the Au_8 cluster on the graphene moiré was estimated. We predict that a Au_8 cluster prefers to form a double-layer wall structure in the fcc region, which is consistent with the double-layer Au islands observed in the experiment [6] and the fact that nucleation of Au starts in the fcc region at low coverage [1]. This consistency provides us insight on the formation mechanism of Au double-layer film on g/Ru(0001). It supports our hypothesis that the sintering mode of Au clusters is Ostwald ripening and the vertical Au_2 is the major diffusing species and the building block to form larger Au islands on g/Ru(0001).

In Chapter 6, we studied the morphology of Cu clusters on g/Cu(111) via investigating the adsorption of a Cu_{19} cluster in the fcc region of g/Cu(111) using MD simulations with the COMB3 potential. From these simulations, we determined the low energy Cu_{19} structures and their adsorption energies at 0 K on g/Cu(111). Our results show that at low temperature, a Cu_{19} cluster prefers to form a 3D compact structure on

g/Cu(111). It implies that 3D Cu aggregates, different from 2D Au islands on g/Ru(0001), may form on g/Cu(111). We also studied the mobility of Cu clusters on g/Cu(111) by performing NVT-MD simulations at elevated temperatures. The analysis shows that the small corrugation of g/Cu(111) imposes weak interation on the supported Cu clusters, which suggests that g/Cu(111) may not be an ideal substrate for the formation and growth of isolated Cu clusters.

Our results show that graphene moiré has the potential of being a suitable template for the rational design of metal cluster superlattices. The consistency of our predictions with available experimental observations suggests that these understandings and insights may help experimental researchers achieve dense super-lattices of clusters of additional transition metals on g/Ru(0001), for applications including model catalysis studies.

7.2 Outlook

We have performed computational studies to investigate the graphene moiré formed on Ru(0001) and its function as the support and template of growing catalytic metal clusters. The graphene moiré has periodically alternating regions of strong and weak interactions with Ru(0001). This periodic and heterogeneous nature of the graphene moiré and its good stability makes g/Ru(0001) a viable template that supports cluster formation and is free of other reactive elements. As graphene is a chemically inert carbon surface, only the clusters formed on it are expected to participate in catalytic reactions, thereby reducing the complexity of reaction mechanisms. This stands in contrast to oxide-supported catalysts. There is thus a great opportunity to study catalytic

reactions at low temperature on metal clusters supported on g/Ru(0001), and conceivably other metal-supported graphene moiré surfaces.

Various metal species have been studied experimentally and computationally on g/Ru(0001) and other supported graphene, such as g/Ir(111), g/Rh(111), etc. In particular, Rh, Pt, Ru, Pd, Co, and Au were all seen to nucleate in the fcc region of g/Ru(0001) [1, 5]. While Rh, Pt, and Ru form finely dispersed small clusters at low coverages, Pd and Co rapidly form large 3D aggregates, and Au forms large 2D islands. Pt, W, Re, Fe, and Au on g/Ir(111) have been studied by N'Diaye *et al.* [7] who reported that Pt, W, and Re form epitaxial cluster superlattices, while Fe and Au do not. Several key factors that govern the growth and distribution of metal on graphene moiré have been suggested. It was concluded that the metals that grow epitaxial cluster superlattices on supported graphene have three characteristics: (1) a large cohesive strength to form strong bonds; (2) a large extension of localized valence orbital to efficiently interact with graphene and initiate rehybridization of carbon atoms; and (3) a certain lattice match with the graphene unit cell [7].

The preference of metal clusters forming 2D planar islands on graphene moiré suggests their strong interaction with the graphene. It is thus proposed that a competition between metal-C and metal-metal interaction should determine the morphology of clusters in the cluster formation process. As long as the metal-C interaction is stronger than the metal-metal interaction, a 2D growth mode will persist (i.e., metal wetting the graphene). Otherwise, growth will shift to a 3D mode. The strength of the metal-C bond increases in the order of Co < Pd < Rh < Pt < Ir < Ru [8, 9]. However, the metal-metal bond energy, or the cohesive energy of the metal, is difficult to determine since it

depends on the size, shape, and structure of the nanoclusters [10, 11], so one cannot assume the cohesive energy of small clusters during the initial stage of growth to be the same as that of bulk metals.

The substrate metal on which graphene is supported also has a significant effect on the cluster growth on the graphene moiré. For instance, Pt cluster has been grown on both g/Ru(0001) [3] and g/Ir(111) [7], but the resulting clusters are qualitatively different. The smallest 2D Pt clusters prefer the fcc regions on g/Ru(0001) instead of the hcp regions on g/Ir(111). Pt clusters on g/Ru(0001) are less uniform and epitaxial cluster superlattices cannot be fabricated at room temperature, and conversion from 2D to 3D clusters occurs at much lower coverages on g/Ru(0001) than g/Ir(111) (0.02 ML vs. 0.1 ML). While there is evidence that graphene interacts more strongly with Ru(0001) than Ir(111), it is unclear how this stronger interaction affects the clustering mechanisms of metals deposited on graphene moiré.

Overall, research in the area of metal cluster growth on graphene moiré supported by metal substrates so far remains in an early exploration phase. For example, additional information about the size-dependent surface bond energies needs to be collected in order to provide a quantitative explanation of the cluster nucleation and growth of a given metal on a graphene moiré and to validate the argument based on metal-C and metal-metal interactions mentioned above. These data would be difficult to obtain experimentally, thus requiring more computational studies on this matter. Furthermore, the kinetics of surface mass transport has not been taken into account and we have not fully understood the effect of the deposition temperature. These fields remain to be further investigated in the future research through experiments and computational

simulation. Although the exact nucleation and growth mechanisms are unclear, it has been demonstrated that the metal-supported graphene moiré has the potential of being a viable template for growing cluster superlattices with tunable properties. With continued research, the rational design of metal cluster superlattices on graphene moiré with desired size, composition, and catalytic properties will eventually be realized.

7.3 References

[1] Z.H. Zhou, F. Gao, D.W. Goodman, Surf. Sci., 604 (2010) L31-L38.

[2] A.K. Engstfeld, S. Beckord, C.D. Lorenz, R.J. Behm, Chemphyschem, 13 (2012) 3313-3319.

[3] Y. Pan, M. Gao, L. Huang, F. Liu, H.J. Gao, Appl. Phys. Lett., 95 (2009) 093106.

[4] K. Donner, P. Jakob, J. Chem. Phys., 131 (2009) 164701.

[5] E. Sutter, P. Albrecht, B. Wang, M.L. Bocquet, L.J. Wu, Y.M. Zhu, P. Sutter, Surf. Sci., 605 (2011) 1676-1684.

[6] L. Liu, Z.H. Zhou, Q.L. Guo, Z. Yan, Y.X. Yao, D.W. Goodman, Surf. Sci., 605 (2011) L47-L50.

[7] A.T. N'Diaye, T. Gerber, C. Busse, J. Myslivecek, J. Coraux, T. Michely, New J. Phys., 11 (2009) 103045.

[8] D. Tzeli, A. Mavridis, J. Phys. Chem. A, 110 (2006) 8952-8962.

[9] J.A.M. Simoes, J.L. Beauchamp, Chem. Rev., 90 (1990) 629-688.

[10] H.K. Kim, S.H. Huh, J.W. Park, J.W. Jeong, G.H. Lee, Chem. Phys. Lett., 354 (2002) 165-172.

[11] K.K. Nanda, S.N. Sahu, S.N. Behera, Phys. Rev. A, 66 (2002) 013208.

APPENDIX A

SUPPLEMENTARY INFORMATION FOR CHAPTER 2

A.1 Convergence tests

We have performed a series of tests on the effect of the size of the vacuum region, the number of Ru layers in the Ru(0001) substrate, and the number of Ru layers relaxed, on the adsorption energies of the adatoms on g/Ru(0001). The results are listed in Table A.1.

Table A.1: Results of convergence tests with respect to size of vacuum region; number of Ru layers in the Ru(0001) substrate; and the number of Ru layers relaxed. Values are the adsorption energies of Rh_1 and Au_1 (in eV) in the off-t1 and t2 sites, respectively, on the (3×3) fcc g/Ru(0001) model surface.

setup	Rh_1	Au_1
3 Ru layers, relaxing graphene and top Ru layer		
13 Å vacuum	-2.65	-1.42
15 Å vacuum	-2.67	-1.42
17 Å vacuum	-2.67	-1.42
13 Å vacuum, relaxing graphene and top Ru layer		
3 Ru layers	-2.65	-1.42
4 Ru layers	-2.46	-1.33
5 Ru layers	-2.50	-1.32
13 Å vacuum, 5 Ru layers; relaxing graphene and:		
keeping Ru frozen at optimized positions	-2.42	-1.29
relaxing top 1 Ru layer	-2.50	-1.32
relaxing top 2 Ru layers	-2.42	-1.24
relaxing top 3 Ru layers	-2.45	-1.27

The results in Table A.1 show the adsorption energies of Rh_1 and Au_1 are essentially invariant with the size of the vacuum region from 13 to 17 Å. The effect of the number of Ru layers relaxed is also small, at 0.05 eV between relaxing top 1 and 3 Ru layers. Keeping the Ru slab frozen at the optimized position of the clean g/Ru surface results in a small, fortuitous reduction of this difference. The number of Ru layers included in the Ru(0001) substrate has a larger effect on the adsorption energy of the adatoms. The difference between the 3-layer and 5-layer Ru slabs is 0.15 eV for Rh_1 and 0.11 eV for Au_1.

Because a significant number of large-scale calculations using the full (12×12)-graphene moiré on (11×11)-Ru(0001) model are needed to construct the coarse-grained PESs, we decided to use a 13 Å vacuum region and a 3-layer Ru(0001) slab to support the graphene, with the top Ru layer frozen at the optimized position of the clean g/Ru surface, as it offers a reasonable tradeoff between accuracy and computational cost. According to the tests above, the adsorption energy of Rh_1 and Au_1 on the coarse-grained PESs may be overestimated by up to 0.15 and 0.11 eV, respectively, if the 5-Ru layer results are taken to have converged. Several recent studies on graphene moiré on Ru(0001) have used a 3-layer Ru(0001) slab [1-3], although Stradi *et al.* have recently concluded that it takes at least 5 Ru layers to correctly capture the surface electronic structure of g/Ru(0001) [4].

For the calculations performed on the full (12×12)-graphene moiré on (11×11)-Ru(0001) model, we verified that the adsorption energies of the adatoms at selected sites change by less than 0.10 eV, and the estimated global diffusion barriers change by less than 0.05 eV, by further converging geometry optimization to 0.03 eV/Å on a Γ-centered

3×3×1 Monkhorst-Pack *k*-point grid. The more stringent convergence criteria are not used in constructing the coarse-grained PESs for the same reason as above.

A.2 Adsorption energies on the coarse-grained PESs

The coarse-grained potential energy surfaces for Rh_1 and Au_1 on the graphene moiré/Ru(0001) surface are shown in the symmetry-irreducible zone, with the adsorption energies (ΔE) of each adatom in all the C-top and C_6 ring center sites labeled.

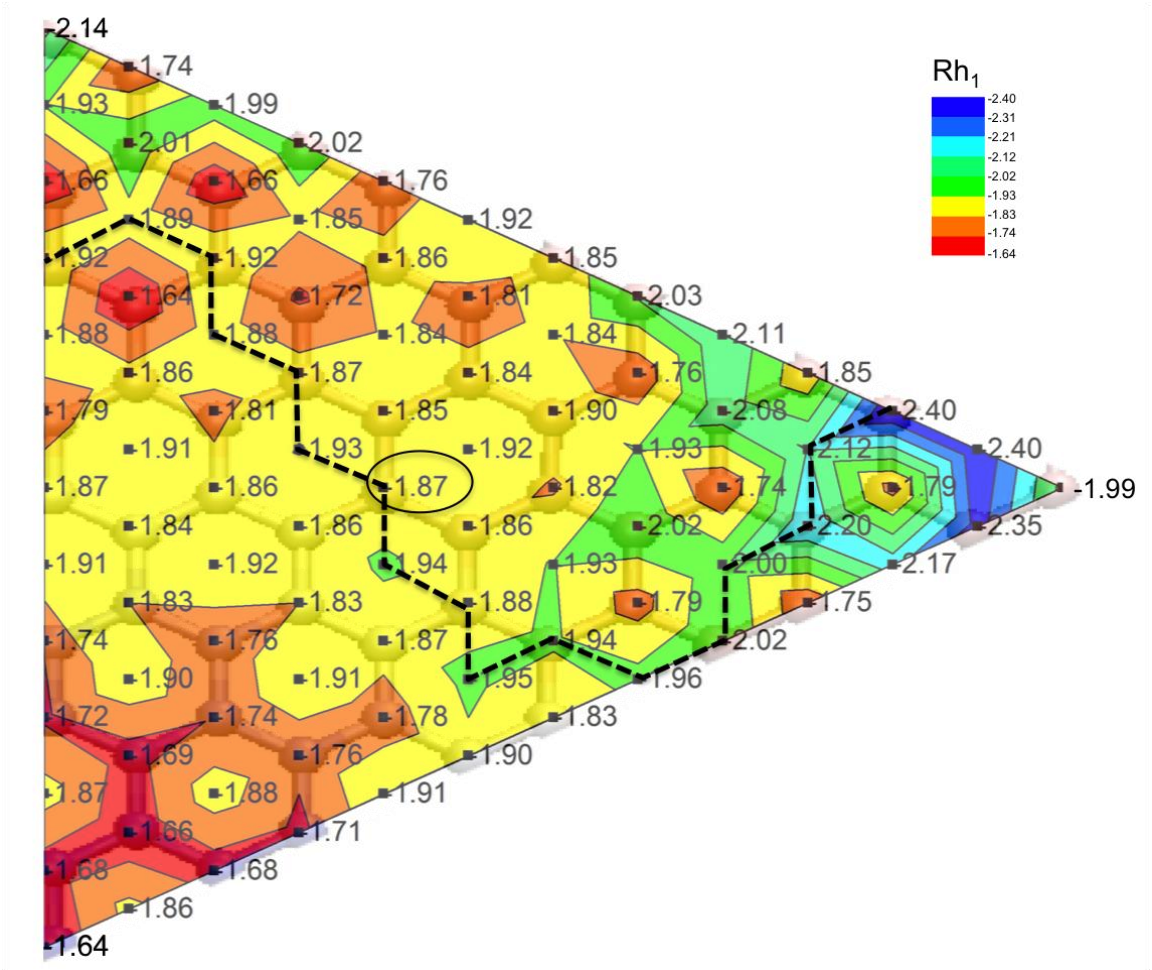

Figure A.1: Potential energy surface for Rh_1 sampled at all the top and ring center sites in the symmetry-irreducible zone of the g/Ru(0001) surface, with the adsorption energy of the adatom labeled at each site. Contours are generated based on interpolation and overlaid onto the graphene network as an aid to the eye only. The minimum-energy diffusion path is marked by a dashed line, and the highest-energy site on the path is circled.

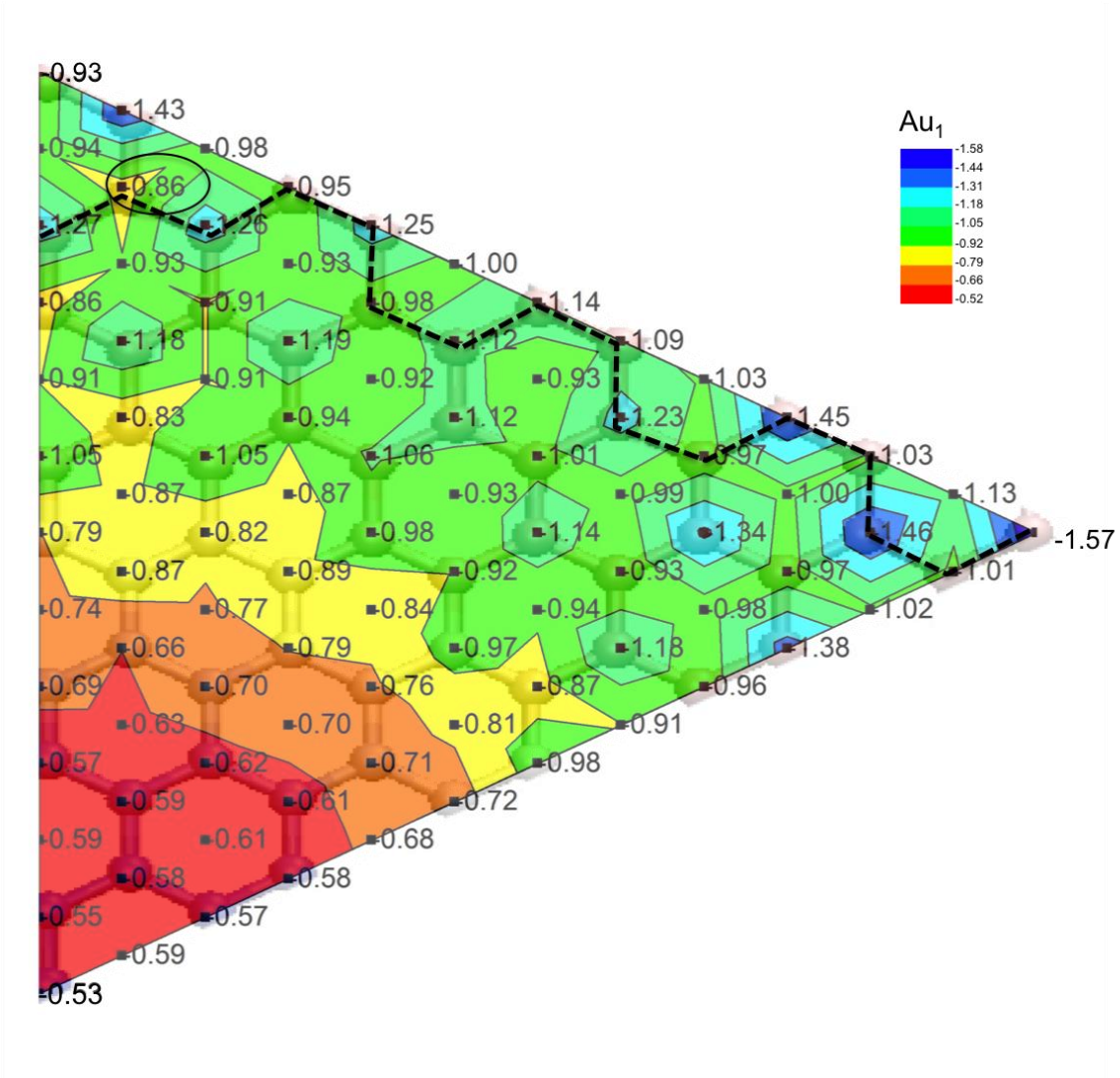

Figure A.2: Potential energy surface for Au_1 sampled at all the top and ring center sites in the symmetry-irreducible zone of the g/Ru(0001) surface, with the adsorption energy of the adatom labeled at each site. Contours are generated based on interpolation and overlaid onto the graphene network as an aid to the eye only. The minimum-energy diffusion path is marked by a dashed line, and the highest-energy site on the path is circled.

A.3 References

[1] D.E. Jiang, M.H. Du, S. Dai, J. Chem. Phys., 130 (2009) 074705.

[2] E. Sutter, B. Wang, P. Albrecht, J. Lahiri, M.L. Bocquet, P. Sutter, J. Phys.-Condens. Matter, 24 (2012) 314201.

[3] B. Wang, B. Yoon, M. Konig, Y. Fukamori, F. Esch, U. Heiz, U. Landman, Nano Lett., 12 (2012) 5907-5912.

[4] D. Stradi, S. Barja, C. Diaz, M. Garnica, B. Borca, J.J. Hinarejos, D. Sanchez-Portal, M. Alcami, A. Arnau, A.L.V. de Parga, R. Miranda, F. Martin, Phys. Rev. B, 85 (2012) 121404.

APPENDIX B

SUPPLEMENTARY INFORMATION FOR CHAPTER 3

Below we report the potential energy surfaces (PESs) calculated for the 18 4d (Y-Ag) and 5d (La-Au) transition metal adatoms on the (3×3) freestanding graphene and the fcc, hcp, and ridge versions of the (3×3) g/Ru(0001) surface models. The PESs for each metal have their own energy scales (in eV). Contours are generated based on interpolation as an aid to the eye.

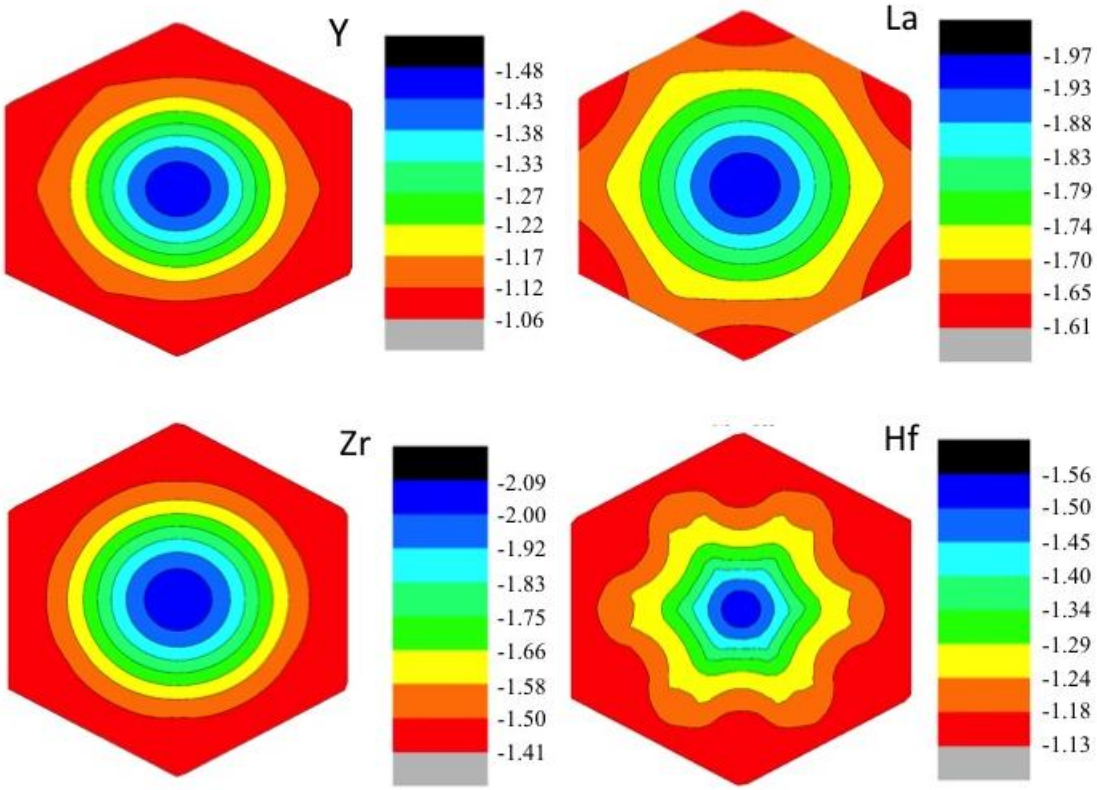

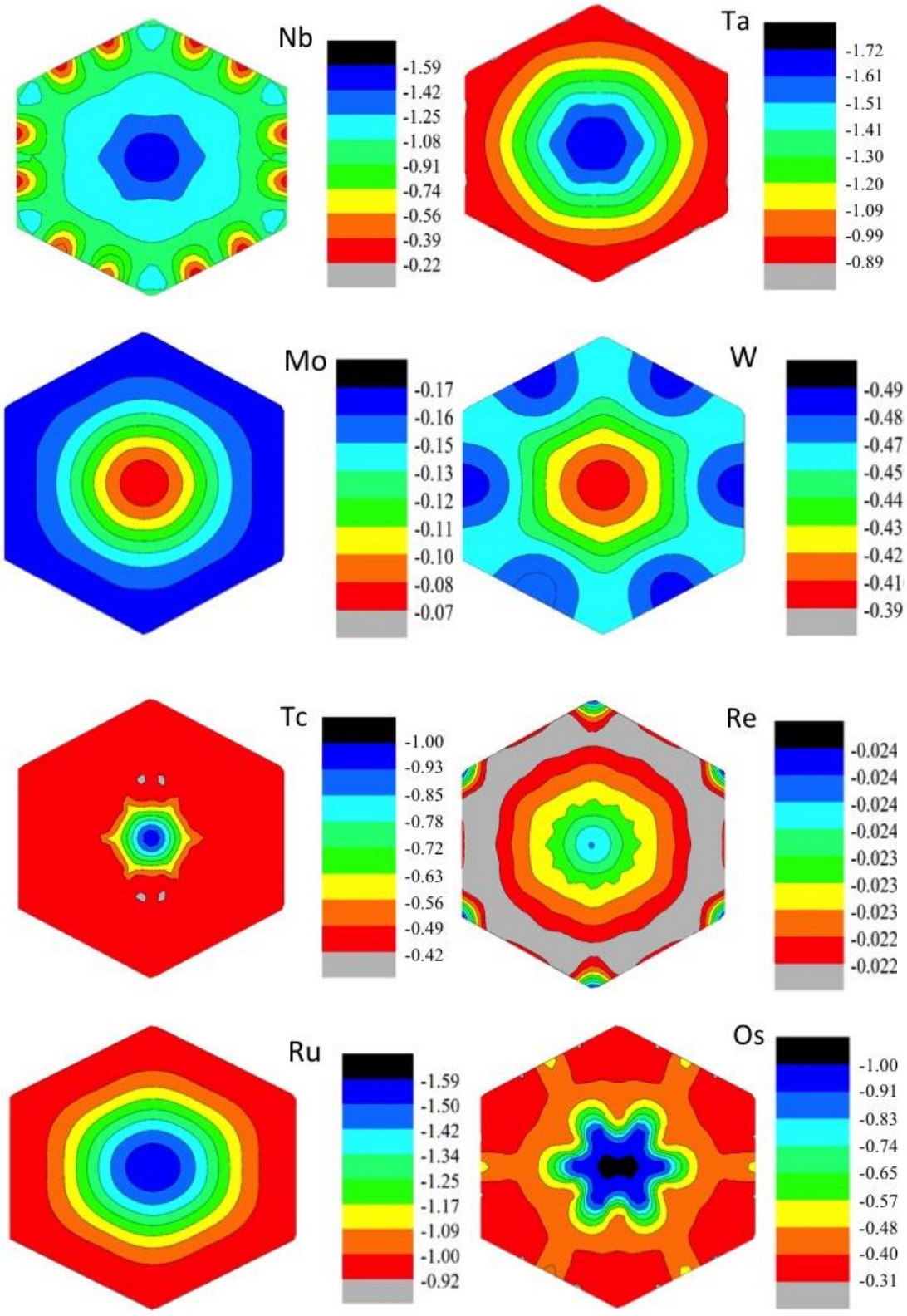
Nb
-1.59
-1.42
-1.25
-1.08
-0.91
-0.74
-0.56
-0.39
-0.22
Ta
-1.72
-1.61
-1.51
-1.41
-1.30
-1.20
-1.09
-0.99
-0.89
Mo
-0.17
-0.16
-0.15
-0.13
-0.12
-0.11
-0.10
-0.08
-0.07
W
-0.49
-0.48
-0.47
-0.45
-0.44
-0.43
-0.42
-0.41
-0.39
Tc
-1.00
-0.93
-0.85
-0.78
-0.72
-0.63
-0.56
-0.49
-0.42
Re
-0.024
-0.024
-0.024
-0.024
-0.023
-0.023
-0.023
-0.022
-0.022
Ru
-1.59
-1.50
-1.42
-1.34
-1.25
-1.17
-1.09
-1.00
-0.92
Os
-1.00
-0.91
-0.83
-0.74
-0.65
-0.57
-0.48
-0.40
-0.31

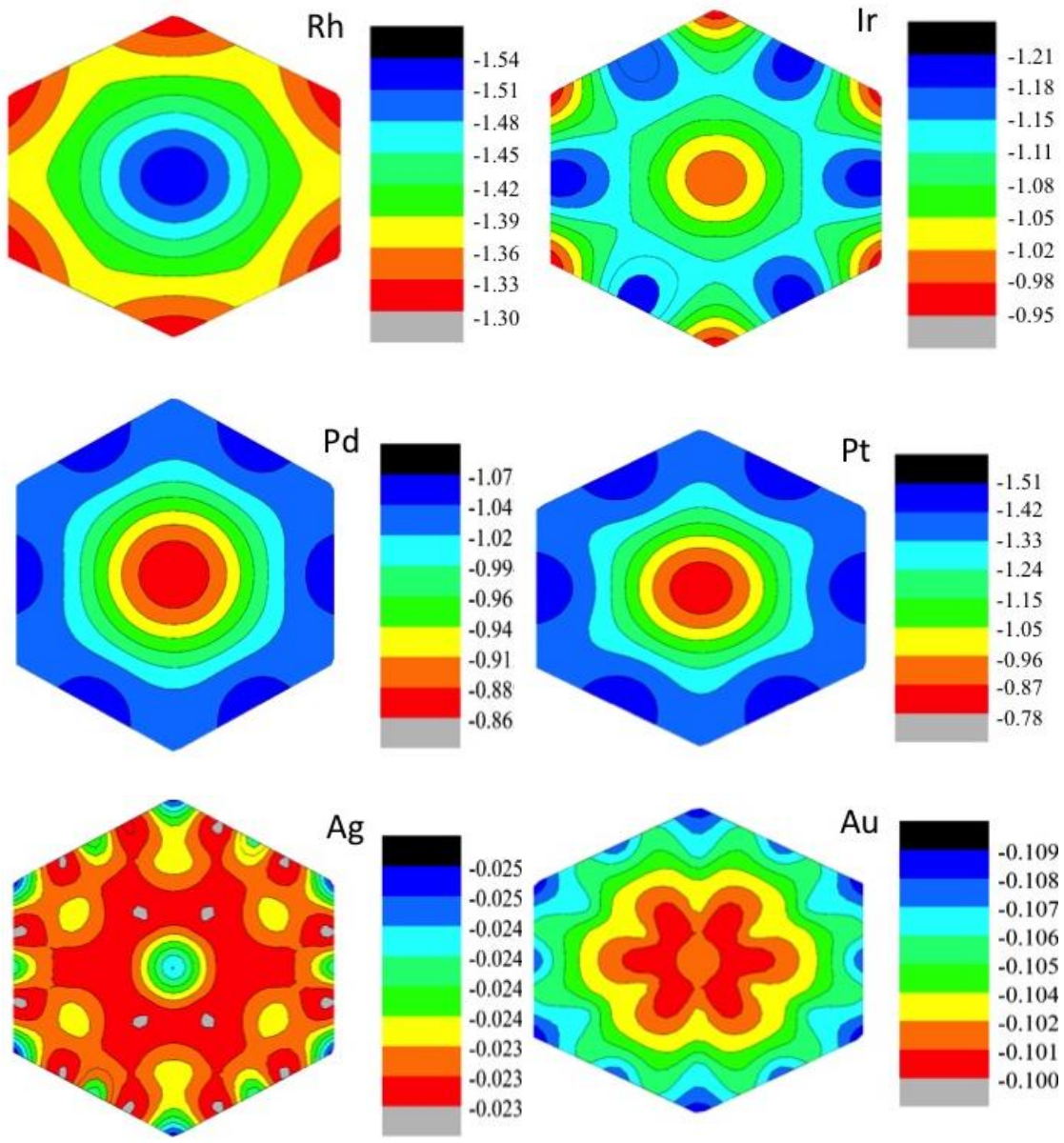

Figure B.1: PESs of the 18 4d and 5d transition metal adatoms on freestanding graphene. The color scale shows the adsorption energy in eV.

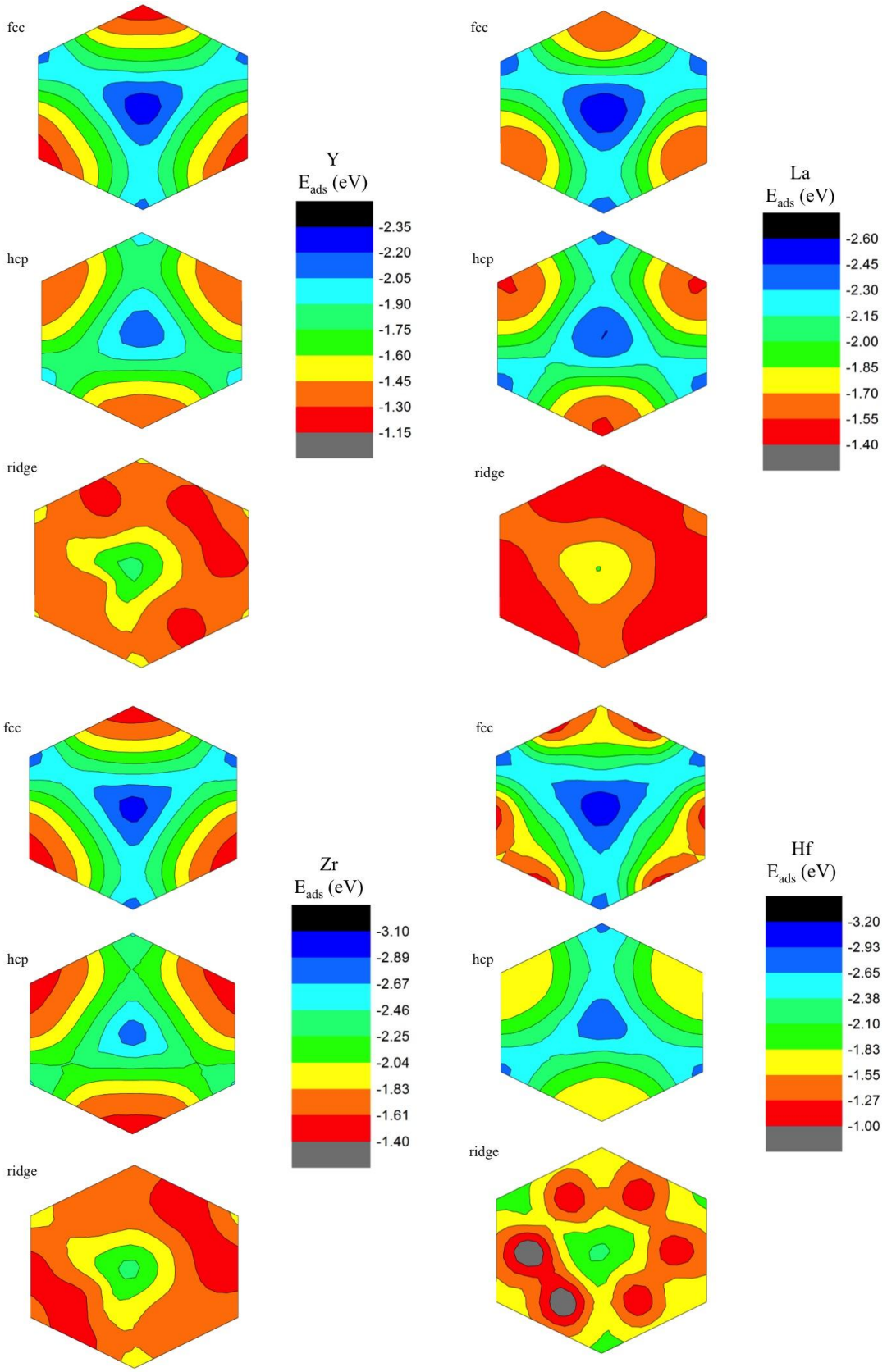
fcc
hcp
ridge
Y
E_{ads} (eV)
-2.35
-2.20
-2.05
-1.90
-1.75
-1.60
-1.45
-1.30
-1.15
La
E_{ads} (eV)
-2.60
-2.45
-2.30
-2.15
-2.00
-1.85
-1.70
-1.55
-1.40
Zr
E_{ads} (eV)
-3.10
-2.89
-2.67
-2.46
-2.25
-2.04
-1.83
-1.61
-1.40
Hf
E_{ads} (eV)
-3.20
-2.93
-2.65
-2.38
-2.10
-1.83
-1.55
-1.27
-1.00

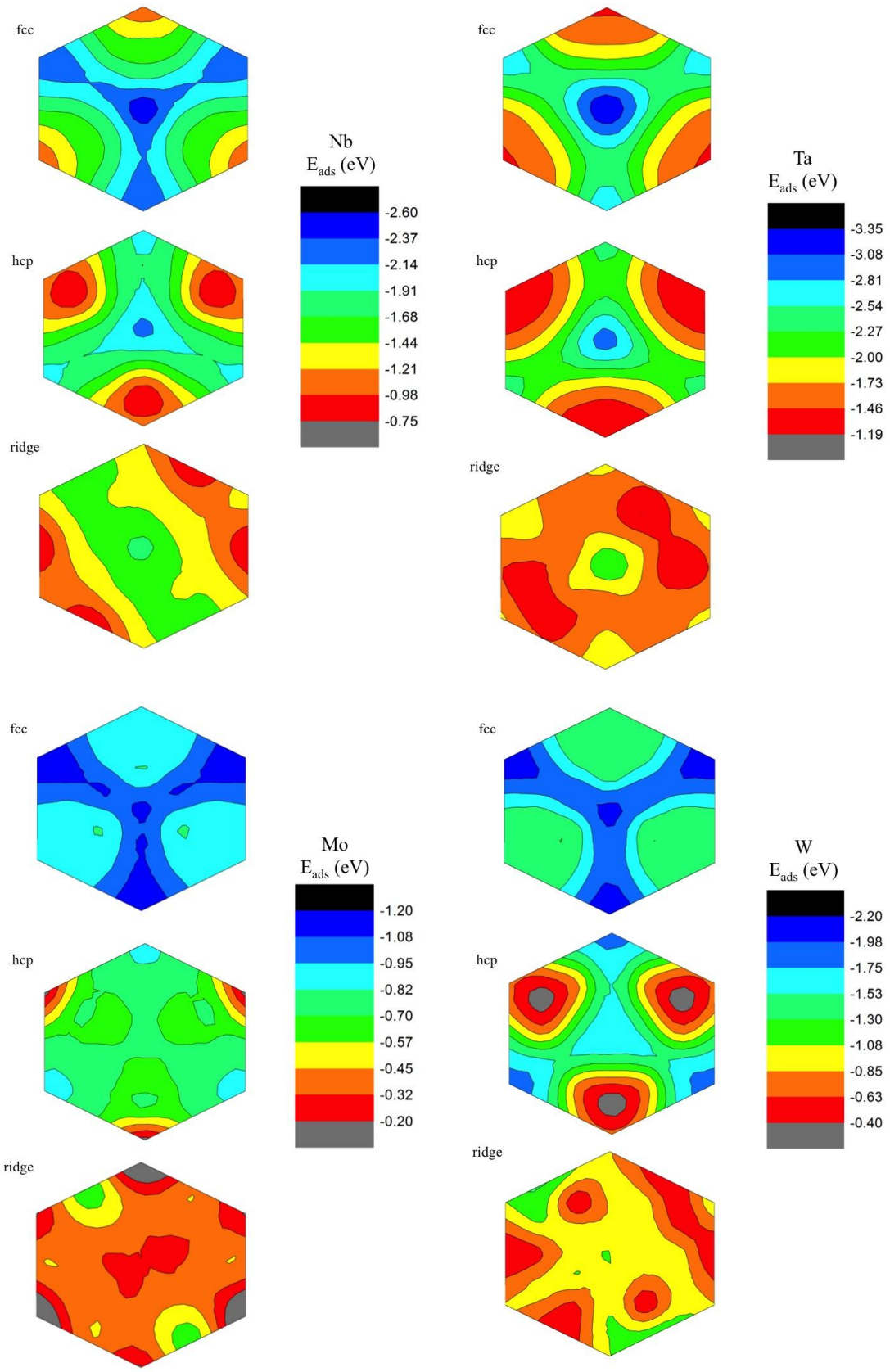
fcc
hcp
ridge
Nb
E_{ads} (eV)
-2.60
-2.37
-2.14
-1.91
-1.68
-1.44
-1.21
-0.98
-0.75
fcc
hcp
ridge
Ta
E_{ads} (eV)
-3.35
-3.08
-2.81
-2.54
-2.27
-2.00
-1.73
-1.46
-1.19
fcc
hcp
ridge
Mo
E_{ads} (eV)
-1.20
-1.08
-0.95
-0.82
-0.70
-0.57
-0.45
-0.32
-0.20
fcc
hcp
ridge
W
E_{ads} (eV)
-2.20
-1.98
-1.75
-1.53
-1.30
-1.08
-0.85
-0.63
-0.40

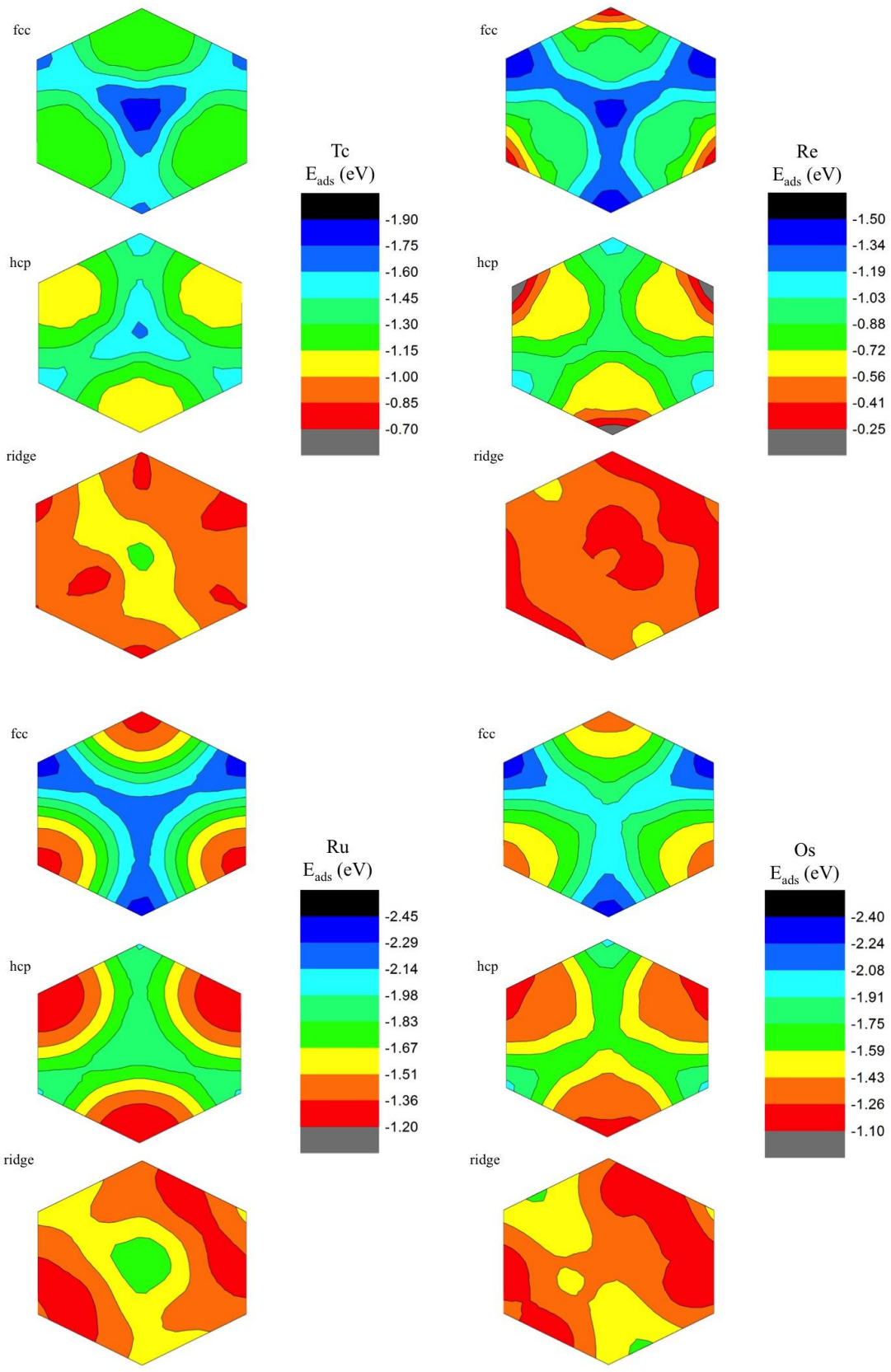
fcc
hcp
ridge
Tc
E_{ads} (eV)
-1.90
-1.75
-1.60
-1.45
-1.30
-1.15
-1.00
-0.85
-0.70
fcc
hcp
ridge
Re
E_{ads} (eV)
-1.50
-1.34
-1.19
-1.03
-0.88
-0.72
-0.56
-0.41
-0.25
fcc
hcp
ridge
Ru
E_{ads} (eV)
-2.45
-2.29
-2.14
-1.98
-1.83
-1.67
-1.51
-1.36
-1.20
fcc
hcp
ridge
Os
E_{ads} (eV)
-2.40
-2.24
-2.08
-1.91
-1.75
-1.59
-1.43
-1.26
-1.10

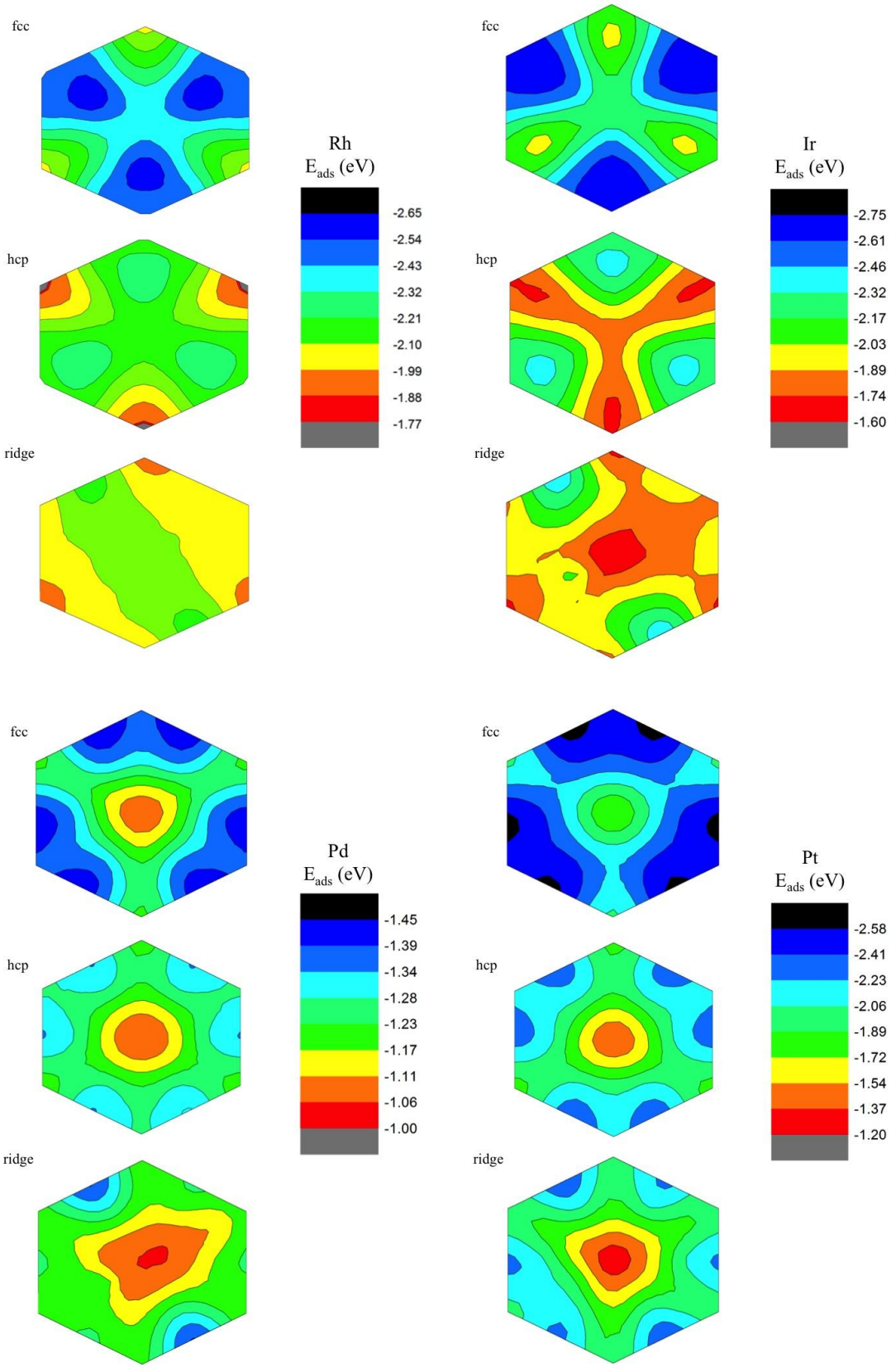
fcc
hcp
ridge
Rh
E_{ads} (eV)
-2.65
-2.54
-2.43
-2.32
-2.21
-2.10
-1.99
-1.88
-1.77
fcc
hcp
ridge
Ir
E_{ads} (eV)
-2.75
-2.61
-2.46
-2.32
-2.17
-2.03
-1.89
-1.74
-1.60
fcc
hcp
ridge
Pd
E_{ads} (eV)
-1.45
-1.39
-1.34
-1.28
-1.23
-1.17
-1.11
-1.06
-1.00
fcc
hcp
ridge
Pt
E_{ads} (eV)
-2.58
-2.41
-2.23
-2.06
-1.89
-1.72
-1.54
-1.37
-1.20

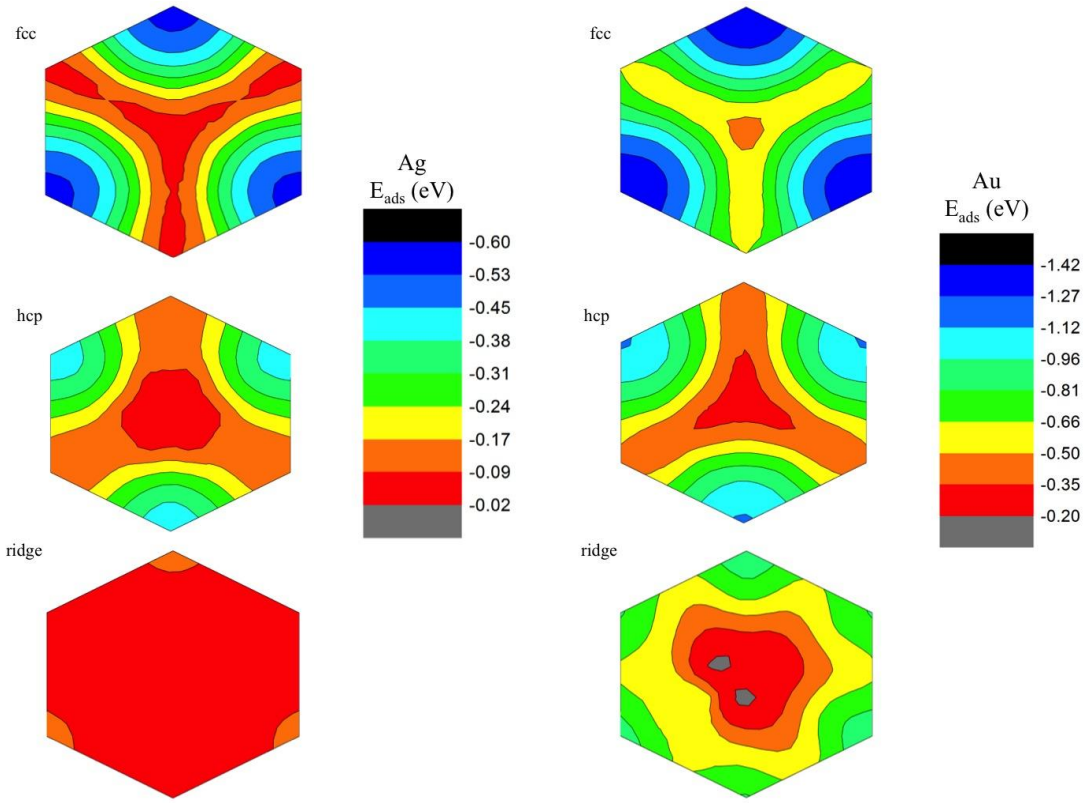

Figure B.2: PESs of the 18 4d and 5d transition metal adatoms on the (3×3) fcc, hcp, and ridge g/Ru(0001) model surfaces. The color scale shows the adsorption energy in eV.

APPENDIX C

SUPPLEMENTARY INFORMATION FOR CHAPTER 4

We provide the figures for the most stable dimer configurations in the hcp (Figure C.1) and the ridge region (Figure C.2) for Rh and Au. We also show an example of different proposed diffusion modes we considered for Rh_2 in the fcc region in Figure C.3. The diffusion paths for Rh_3 (Figure C.4) and Au_3 (Figure C.5) in the ridge region are provided as well.

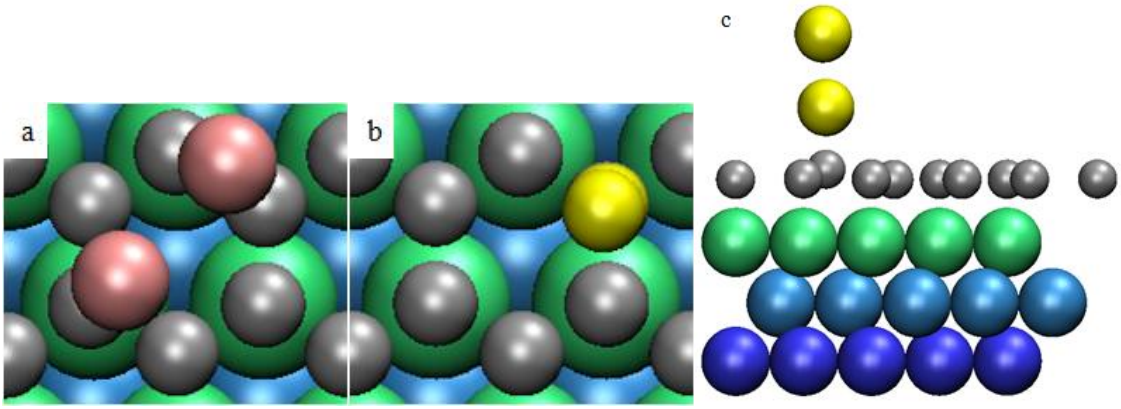

Figure C.1: The most stable dimer configuration in the hcp region for (a) Rh (pink), top view; (b) Au (yellow), top view; (c) Au, side view. Three Ru (green, light blue, dark blue) layers are shown, with the bottom layer (dark blue) hidden behind the top layer (green) in the top views. The grey atoms are C.

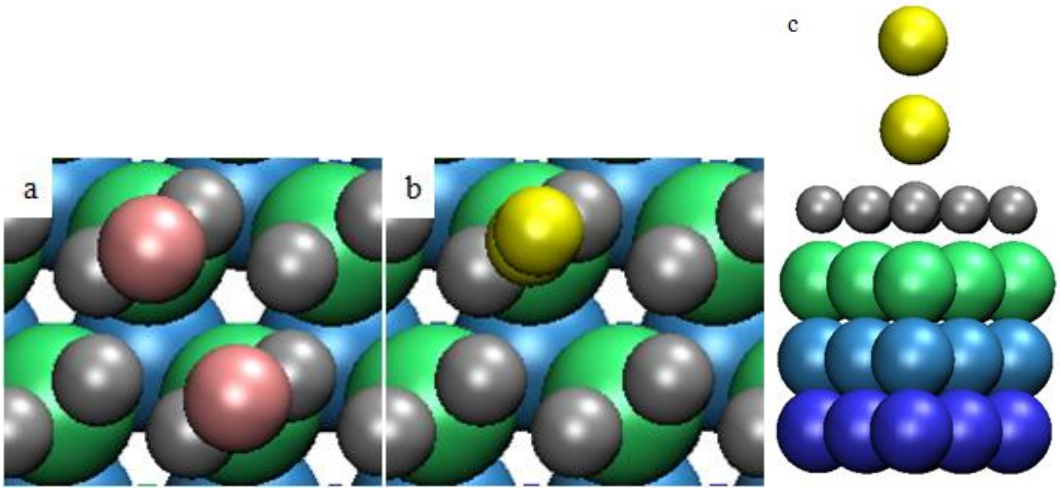

Figure C.2: The most stable dimer configuration in the ridge region for (a) Rh, top view; (b) Au, top view; (c) Au, side view. The element colors are the same as before.

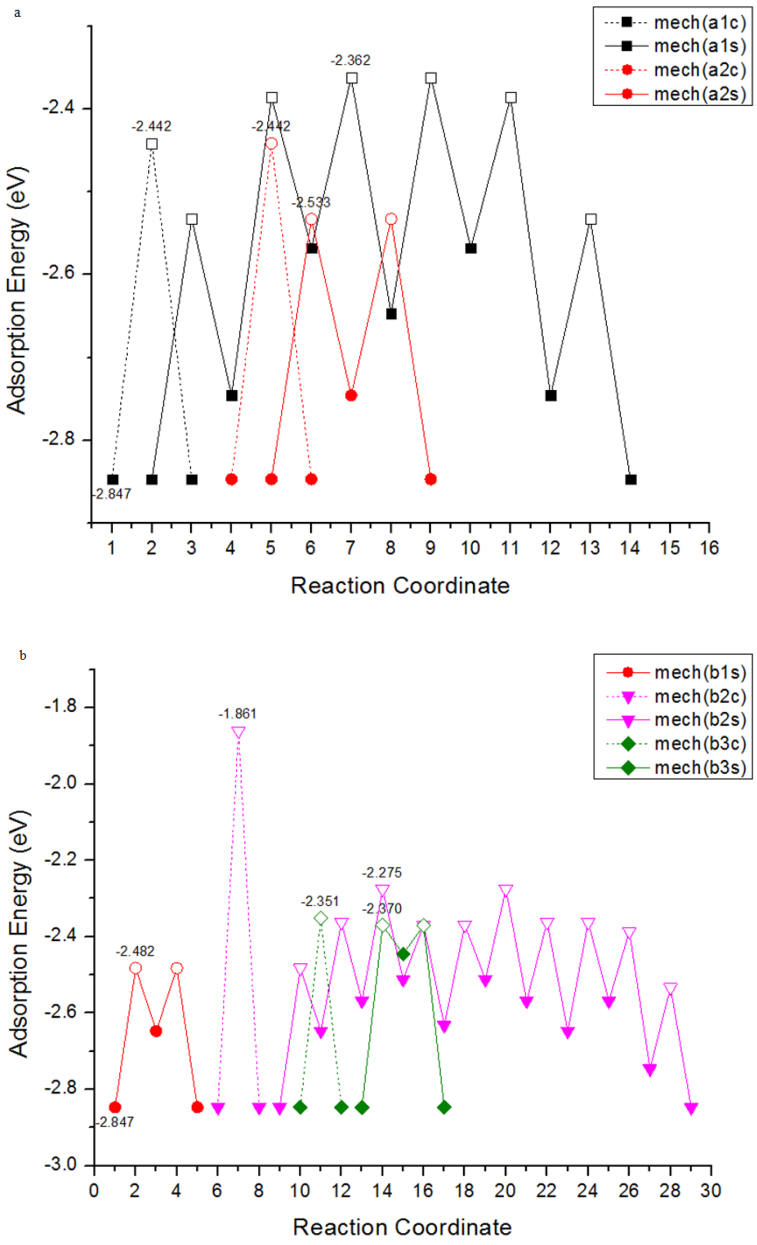

Figure C.3: Different diffusion modes considered for Rh_2 diffusing within the fcc region. In (a), all modes are within the same 6-C ring, which do not contribute to the net diffusion. In (b), all modes are across two neighboring 6-C rings, which contribute to the net diffusion. Concerted modes are represented by "c" and dashed line, while stepwise modes are represented by "s" and solid line. Each mode is numbered, e.g. mech(b2c), which indicates mechanism #2 in (b) with concerted mode. Filled symbols are local minima (LM) and unfilled symbols are transition states (TS). The adsorption energy of LM and TS for each diffusion mode is labeled. Diffusion paths are shifted from each other in x-coordinate for a better view. A combination of mech(b1s) and mech(b3s) is the path with the lowest energy barrier for Rh_2 to diffuse within the fcc region.

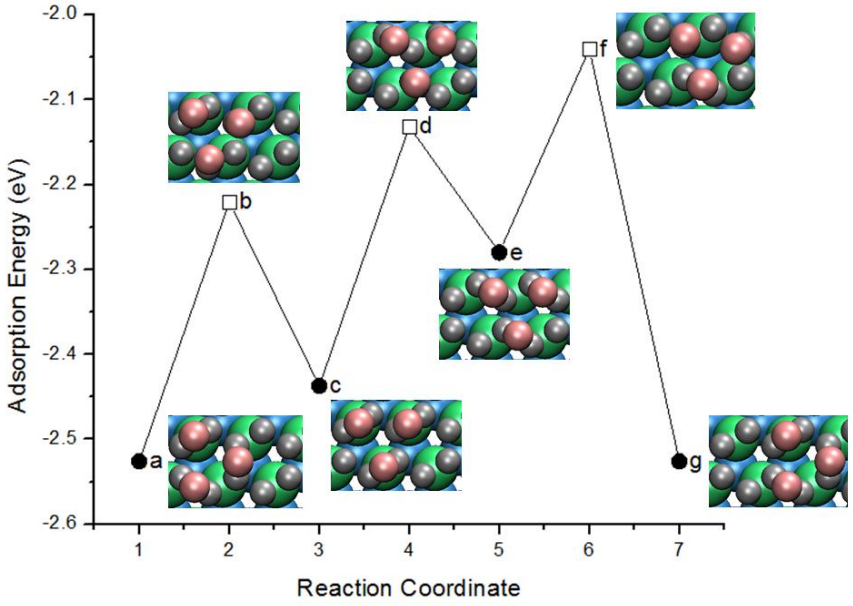

Figure C.4: The diffusion path of Rh_3 in the ridge region. Circles (squares) indicate stable local minima (transition states). The element colors are the same as before.

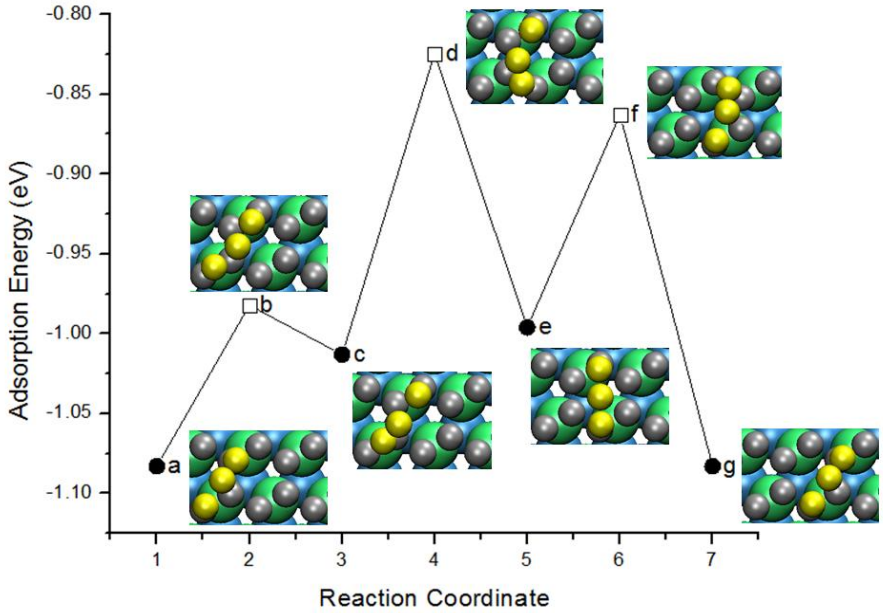

Figure C.5: The diffusion path of Au_3 in the ridge region. Circles (squares) indicate stable local minima (transition states). The element colors are the same as before.

APPENDIX D

SUPPLEMENTARY INFORMATION FOR CHAPTER 5

Table D.1: The adsorption energy of the 6 most stable Au_8 clusters in the fcc region of g/Ru(0001) using a (5×5) and a (6×6) supercell with 3 layers of Ru.

Au_8 structure	$E_{ads\_(5\times5)}$ (eV)	$E_{ads\_(6\times6)}$ (eV)
F1	-2.10	-1.58
F2	-1.99	-1.44
F3	-1.87	-1.31
F4	-1.67	-1.17
F5	-1.82	-1.22
F6	-1.58	-0.84

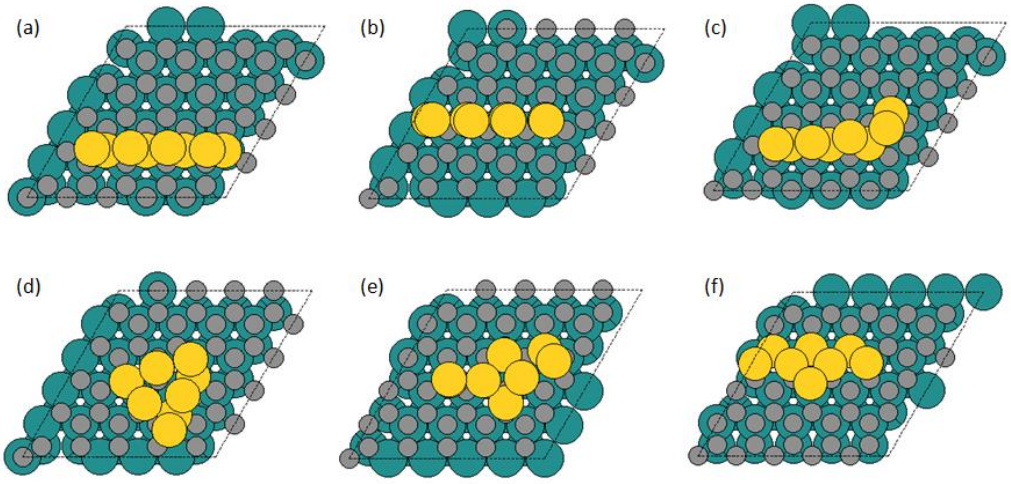

Figure D.1: Top view of the structures of the 6 most stable Au_8 clusters ((a)-(f): in energy-ascending order) in the fcc region of g/Ru(0001) with 2 layers of Ru.

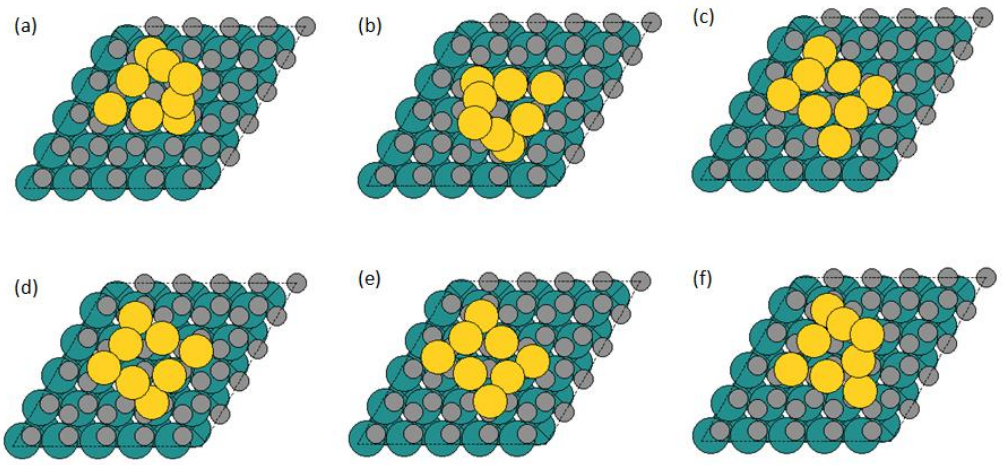

Figure D.2: Top view of the structures of the 6 most stable Au_8 clusters ((a)-(f): in energy-ascending order) in the ridge region of g/Ru(0001) with 2 layers of Ru.

VITA

DIE TENG

DIE TENG was born in Chengdu, Sichuan, China on July 14th, 1986. She attended public schools in Chengdu, China, and went to college in the U.S. in 2005. She received a B.S. in Chemistry and Physics from Illinois College, Jacksonville, Illinois in 2009 before coming to Georgia Institute of Technology to pursue a doctorate in Chemical Engineering. When she is not working on her research, Ms. Teng enjoys reading, singing, and hiking in nature.